

FACULTAD DE CIENCIAS FÍSICAS
MÁSTER EN ASTROFÍSICA



**ANÁLISIS DE CURVAS DE LUZ DE TESS: PERIODOS DE ROTACIÓN Y
FULGURACIONES DE LAS ESTRELLAS M DE CARMENES**

**ANALYSIS OF TESS LIGHT CURVES: ROTATIONAL PERIODS AND FLARES ON CARMENES' M
STARS**

Por:

Sebastián LÓPEZ SKRZYPINSKI

Tutores:

José Antonio CABALLERO (CAB)

David MONTES (UCM)

TRABAJO DE FIN DE MÁSTER

Madrid, Junio de 2021

*Those things that ye have sung,
I will show them forth,
that ye may see what ye have done*

J.R.R. Tolkien, The Silmarillion

Abstract

Context. CARMENES is a high resolution spectrograph built for the 3.5m telescope at the Calar Alto Observatory. The main aim of this instrument is to detect low mass planets around M dwarfs. In order to achieve this goal, it is critical to characterize the monitored stars, especially their activity and rotation.

Methods. Using *TESS* data, we studied the rotation and activity in the 2 minute cadence time series of 1285 M dwarfs in the CARMENES input catalog. The Generalised Lomb-Scargle (GLS) periodogram was used to search periodic signals resulting from stellar rotation. Using splines and Fourier polynomials, the light curves of rotating stars were detrended to look for flaring activity

Results. Using the GLS periodogram, we measured 244 rotation periods between 0.105 and 10.5 d. Of them, 107 are consistent with their literature counterparts. A total of 110 new rotational periods of M dwarfs were obtained. Removing binary stars, we found 2567 flares with energies ranging from $10^{29.9}$ erg to $10^{35.2}$ erg for 168 rotating M dwarfs. Fitting the rate of flares with energies greater than 10^{33} erg to a power law of the form $NdE \propto E^{-\alpha}$, we determined α to be $2.095^{+0.043}_{-0.059}$. We find α to be dependant with the spectral type: later types have a steeper distribution.

Resumen

Contexto. CARMENES es un espectrógrafo de alta resolución construido en el telescopio 3.5m del Observatorio de Calar Alto. El objetivo principal del instrumento es detectar planetas de baja masa alrededor de enanas M. Para conseguirlo, es vital caracterizar las estrellas monitorizadas, especialmente su actividad y rotación.

Método. Haciendo uso de los datos de *TESS*, se ha estudiado la rotación y la actividad en las series temporales con cadencia de 2 minutos de 1285 enanas M del catálogo de CARMENES. Se ha utilizado el periodograma Lomb-Scargle Generalizado (GLS) para buscar señales periódicas debidas a la rotación de las estrellas. Usando splines y polinomios de Fourier, se han eliminado tendencias periódicas de las curvas de luz de estrellas rotadoras con el fin de estudiar sus fulguraciones

Resultados. Usando el periodograma GLS, se han medido 244 periodos de rotación entre 0.105 y 10.5 días. De éstos, 107 son consistentes con la literatura. Se han obtenido total de 110 nuevos periodos para enanas M. Eliminando estrellas binarias, se han encontrado 2567 fulguraciones con energías entre $10^{29.9}$ erg y $10^{35.2}$ erg en 168 enanas M rotadoras. Ajustando la frecuencia de fulguraciones con energías superiores a 10^{33} erg a una ley de potencias de la forma $NdE \propto E^{-\alpha}$, se determina un valor para α de $2.095^{+0.043}_{-0.059}$. Encontramos que α depende del tipo espectral: tipos más tardíos tienen distribuciones más pronunciadas.

Contents

1. Introduction	1
1.1. M dwarfs	1
1.2. CARMENES	2
1.3. Aims	2
2. Data	2
2.1. Carmencita	2
2.2. <i>TESS</i>	2
3. Analysis	5
3.1. Rotation periods	5
3.2. TESS masks and contamination	7
3.3. Summary sheets	8
3.4. Detrending the light curves	10
3.4.1. Fourier fit	11
3.5. Stellar flares	13
3.5.1. Identification	13
3.5.2. Flare energy estimation and power law	13
4. Results	16
4.1. Periods	16
4.2. Activity	17
4.2.1. Flares in rotating stars	17
4.2.2. Dependence with spectral type	18
4.3. Relation rotation-activity	19
4.3.1. Activity indicators	19
4.3.2. Flare activity and rotation	20
4.4. Multiple systems	21
5. Conclusions and future work	23
References	23
Appendices	26
A. Periods	26
B. Summary sheets	31
C. Solar System objects	55

1. Introduction

The science of exoplanets is nowadays a consolidated branch of astrophysics, but until recent years, this worlds existed only in philosophy and science fiction. One of the earliest accounts in modern European history proposing the existence of exoplanets come from the Italian mathematician and philosopher Giordano Bruno (1458-1600), who thought that stars are objects similar to the Sun, with planets orbiting them.

In 1952, Doppler spectroscopy and transit methods were proposed as possible ways of detecting Jupiter-like planets in close orbits to their host stars (Struve 1952). Both methods proved their potential in 1995 and 1999 respectively, with the discoveries of 51 Pegasi b (Mayor and Queloz 1995) and HD209458b (Charbonneau et al. 2000). Thus, the science of exoplanets was born.

Since then, almost 4400 exoplanets have been confirmed to exist¹. Most of them were discovered using transit method thanks to space telescopes such as *Kepler*, which was operational between 2009 and 2018 and has been used to discover around 2800 planets until date.

On the other hand, Earth-based spectrographs have also largely contributed to the discover of exoplanets. This is the case of HARPS at La Silla observatory. HARPS is an echelle spectrograph built to measure radial velocities with an accuracy of 1 m s^{-1} and has discovered over 130 exoplanets since 2004.

The study of exoplanets has been turning towards red dwarfs for multiple reasons. First of all, M dwarfs are the most numerous stars in the Universe, so focusing on them is highly efficient. Secondly, their low masses and sizes makes them perfect candidates for detecting planets around them using the most common methods: radial velocity and transits.

1.1. M dwarfs

M dwarfs are the smallest ($0.1 - 0.6 R_{\odot}$) and coolest ($2300 - 4100 \text{ K}$) kind of stars in the main sequence and are the transition between stars and substellar objects ($M < 0.07 M_{\odot}$). They are also the most abundant type of star in the Milky Way, making up for almost three quarters of all the stars (Fabricius et al. 2021). This alone makes M dwarfs the perfect candidate for exoplanet detection, but they present other advantages that have to do with the detection methods.

The fact that red dwarfs are very faint ($L_{\text{bol}} < 0.30 L_{\odot}$) turns into an advantage when detecting planets by the transit method, as a dip in brightness caused by a planet is easier to detect. Regarding the radial velocity method, the signal created by the presence of a planet is stronger for less massive stars. Thus, the two most used methods for exoplanetary search are more sensitive by design when the host star is a red dwarf.

Furthermore, one of the final aims of exoplanetary research is to find Earth-sized planets orbiting their stars within the habitable zone. This presents another advantage for M dwarfs as their habitable zone lies closer to the star than for other spectral types due to their low effective temperatures and luminosities. Hence, a planet orbiting within the habitable zone of an M dwarf would do it with a short period and would induce a strong signal in both transit and radial velocity data, thus enabling to find smaller planets in this habitable zone.

Despite of all their advantages for exoplanetary research, M dwarfs present their own challenges. First of all, most of the light of an M dwarf is emitted in the red optical and near-infrared. This is a disadvantage because most classical spectrographs operate in the visible region of the electromagnetic spectrum.

Moreover, the high activity of M dwarfs can be a problem for radial velocity methods and planet habitability. The profile of lines in the spectrum can be affected by the presence of plages, stellar spots or granulation, changing the position of their centroids in a way that can resemble the signal of a planet. The periodicity of this type of signal is similar to what is expected from a planet, specially an Earth-mass planet in the habitable zone.

For this last reason, it is critical to characterize the rotation of M dwarfs as to not confound that rotation with a planet. This can be made with spectroscopic analysis of activity lines such as

¹<https://exoplanets.nasa.gov/discovery/exoplanet-catalog/>

H α or Ca II H&K (Jeffers et al. 2018). It is also possible to characterize the rotation of stars using photometric techniques exploiting the variability due to the presence of stellar spots.

1.2. CARMENES

CARMENES (Quirrenbach et al. 2018) is a two-channel, high-resolution spectrograph built at the 3.5 m Calar Alto telescope. It covers from 0.52 to 0.96 μm in the optical channel and from 0.96 to 1.71 μm in the near-infrared channel with spectral resolution $R = 80,000 - 100,000$. Each channel performs radial velocity measurements with a stable accuracy of $\sim 1\text{ m/s}$. The spectral range covered by the CARMENES spectrograph makes it unique in the sense that it completely covers the typical spectra of M stars.

Since 2016, the instrument has been surveying ~ 350 late-type main-sequence stars with the main goal of detecting low-mass planets around them. One of the most famous achievement regarding this goal was the discovery of two Earth-mass planets orbiting Teegarden’s star, a low activity M7.0 dwarf 3.83 pc from the Sun (Zechmeister et al. 2019).

One of the most recent discoveries by CARMENES has been Gliese 486b (Trifonov et al. 2021), a 2.81 M_{\oplus} planet orbiting a M3.5 dwarf. This discovered with radial velocity measurements and confirmed observing transits with *TESS*. Gliese 486b is a perfect candidate for studying its atmosphere using transmission and emission spectroscopy due to its temperature.

As of today, 35 planets have been discovered and another 17 confirmed by CARMENES.

The CARMENES team has also done an extensive work regarding M dwarfs’ activity, atmospheres, rotation, etc., becoming a referent regarding the study of late-type stars. CARMENES has produced over 60 refereed publications, 25 PhD teses and 40 MSc theses that have greatly contributed to the science of cool stars and their worlds.

1.3. Aims

The main goal of this Master’s Thesis is to characterize the rotation of the M dwarfs of the CARMENES sample, as well as their flaring activity. For this purpose, we study the light curves obtained by the *TESS* telescope of the stars of the sample during the full first two cycles of observation plus part of the third cycle (until sector 33).

In addition, we also aim to study the flare frequency distribution of rotating stars by identifying flare events in *TESS* light curves and determine if this distribution changes with the spectral type.

2. Data

2.1. Carmencita

Carmencita (CARMEN(ES) Cool dwarf Information and daTa Archive), is the input catalogs for the CARMENES survey. Version 099 contains 2206 M stars brighter than $J = 12.5$ mag. About 300 of these objects are observed during the guaranteed observation time (GTO).

This database contains stellar parameters such as accurate coordinates, spectral types, photometry from ultraviolet to mid-infrared, parallaxes and spectro-photometric distances, rotational and radial velocities, H_{α} pseudo-equivalent widths, X-ray count rates, multiplicity data, proper motions, metallicities, and much more. These parameters have been either measured by the CARMENES team or compiled from the literature, and everything is fully referenced in the database.

In this work, we looked for periodicity and activity in all the stars that are part of the Carmencita database. We also used the compiled data regarding activity indicators, rotation velocities, effective temperatures, etc.

2.2. TESS

The Transiting Exoplanet Survey Satellite (*TESS*, Ricker et al. 2014) is a space telescope performing a nearly all-sky photometric survey searching for transiting planets in nearby stars. During its

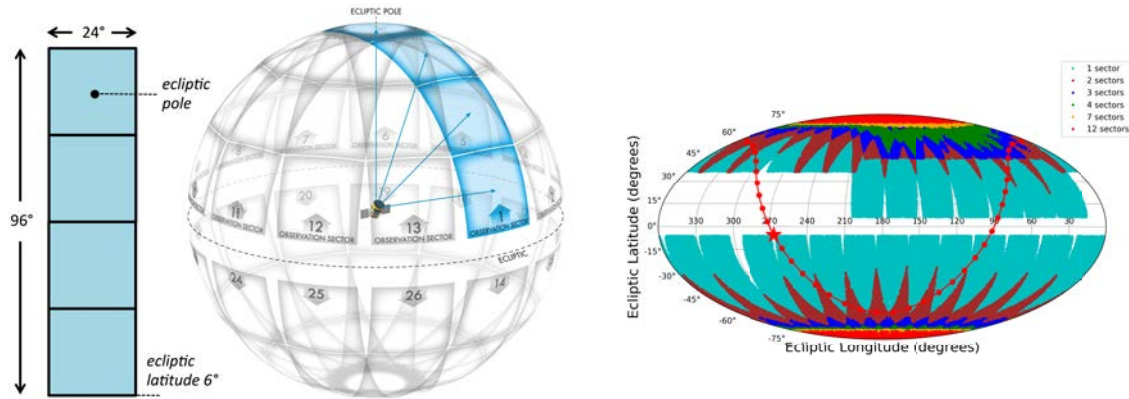


Figure 1: **Left:** *TESS* camera array and theoretical sectors for the main mission. **Right:** actual observing sectors for years 1 and 2 in ecliptical coordinates. The shift in pointing during sectors 14-16 and 24-26 is due to excessive Earth and Moon contamination in cameras 1 and 2 in the nominal pointing.

nominal mission, it took photometry measurements with 2 minute and 30 minute cadences of about 200,000 F5 to M5 spectral types stars, covering a spectral range from 600 to 1000 nm (Fig. 7). It began its observations in July 2018 and ended its planned mission in July 2020, when the extended mission expected to end in September 2022 began.

The *TESS* mission selects its targets making use of the *TESS* Input Catalog (TIC, Stassun et al. 2019): a collection of sources (stars and extended sources) of the sky assembled from different catalogs. The base point-source adopted in the first year of the mission (TICv7) was the 2MASS catalog, as the second *Gaia* data release was not still available. Later (TICv8), the *Gaia* DR2 was adopted as a base point-source catalog. The improvement on angular resolution of the DR2 catalog compared to 2MASS created some cases where the same 2MASS identifier was associated with multiple *Gaia* sources. There were also cases in which a 2MASS source had no *Gaia* counterpart, so they were left unaltered in TICv8.

TESS is equipped with four cameras with custom $f/1.4$ lenses and a field of view (FOV) of 24×24 deg. The cameras are positioned forming a 4×1 array which covers a FOV of 96×24 deg. This constitutes an “observing sector”. Each CCD has two 2048×2048 $15 \times 15 \mu m$ pixel arrays: one for imaging and another for storage, making for a total 4096×4096 effective pixel detector. The pixel arrangement in addition to the FOV means that the image scale is $21 \text{ arcsec pixel}^{-1}$, which is huge. This means that *TESS* is highly susceptible to crowding, and light curves from close sources might be confused or even be the same. Therefore, it is important to look for stars in the neighborhood of a source of interest, and check if their light can be contaminating its light curve.

The main mission was divided into 26 sectors. The first 13 sectors (year 1) covered the southern hemisphere of the ecliptic while sectors 14-26 (year 2) cover the northern hemisphere (see Fig. 1). Each sector is observed during 27.4 days during which *TESS* takes aperture photometry from stars of particular interest each two minutes. For these targets, the *TESS* pipeline defines an aperture mask designed to optimize the signal-to-noise (S/N) of the target, although the large image scale problem cannot be completely avoided. The flux from the pixels in this predefined aperture mask and its surroundings can be accessed through the Target Pixel Files (TPF), which allow for pixel-level photometry if needed.

The *TESS* pipeline allows to study the short cadence light curves (QLP: quick look pipeline) from two different approaches:

- The simple aperture photometry (SAP): the untreated light curve. The values of all pixels in the pre-defined aperture are added together. The background is corrected, but spurious errors such as cosmic ray contamination or long-term variations are present, and systematic errors are not accounted for.

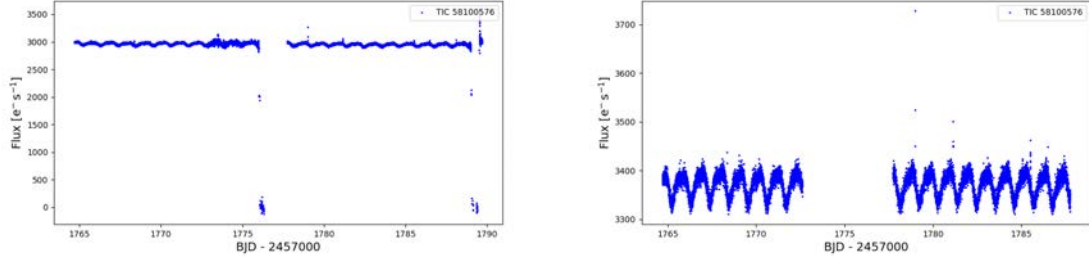


Figure 2: Example of the PDC pipeline removing instrumental systematic errors. The left panel shows the uncorrected SAP time series for J00245+300 with instrumental errors that are not present in the right panel, which shows the PDCSAP flux.

- The presearch data conditioning SAP (PDCSAP): the PDC pipeline identifies time-correlated instrumental signatures in the light curves and corrects the flux of each target to account for crowding. In Fig. 2 an example of PDC in action is shown.

In both cases, *TESS* selects pixels without sources around the aperture mask as background. The resulting light curve will then be obtained by subtracting the flux from the background pixels to the aperture mask.

In addition, *TESS* returns images of the whole FOV every 30 min, making it possible to recover photometry of objects for which there is no aperture photometry through the full-frame images (FFIs).

The focus of this work lies in stars from the Carmencita sample that have been observed by *TESS* within the first two years of observations. We will focus on the 2 minute cadence observations (PDCSAP fluxes), leaving the inspection of FFIs for future work.

The correlation between CARMENES and *TESS* catalogs used here was constructed using *Gaia* DR2 identifiers when available in TICv8 and Carmencita. If this identifier was not present in either of the catalogs, the 2MASS identifier was used instead. Thus, each CARMENES star was assigned a TIC identifier univocally (see Revilla (2020) for further details about the correlation).

Once we obtained the TIC identifiers, we downloaded the light curve data using the bulk download files available in MAST¹ (Mikulski Archive for Space Telescopes). These files allow to download all the light curves for each sector, but can be modified so only the TIC that we need are downloaded.

Our sample consists in 1285 stars from the Carmencita data archive for which *TESS* provided aperture photometry (they have SAP flux). The distribution in sectors of these stars is shown in Table 1, while Table 2 shows the number of stars that we found in multiple sectors. We expect to find photometry for 318 more Carmencita stars by inspecting the FFIs of the 26 sectors, as they can be found in positions covered by *TESS* (see Fig. 3).

Table 1: Number of CARMENES stars with 2 minute cadence found in each *TESS* observing sector in the nominal mission.

South	Year 1												
Sector	1	2	3	4	5	6	7	8	9	10	11	12	13
N_{stars}	4	11	19	43	56	53	35	39	24	10	3	0	0
North	Year 2												
Sector	14	15	16	17	18	19	20	21	22	23	24	25	26
N_{stars}	149	130	150	156	157	159	161	168	142	163	155	147	159
South	Year 3												
Sector	27	28	29	30	31	32	33						
N_{stars}	1	4	15	26	37	62	34						

¹https://archive.stsci.edu/tess/bulk_downloads/bulk_downloads_ffi-tp-lc-dv.html

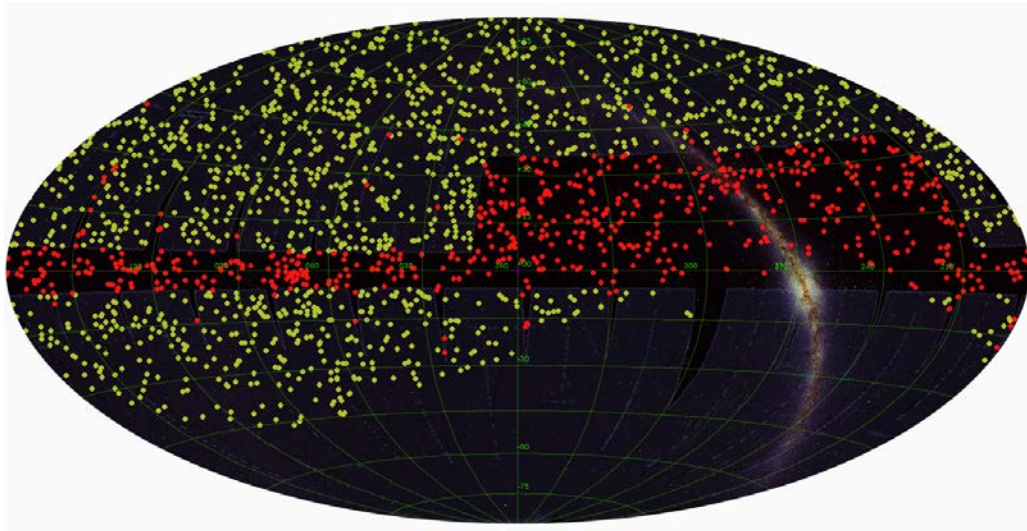


Figure 3: *TESS* 1-26 observing sectors are plotted. The CARMENES sample is overlaid on the sky to show the stars that are out of FOV: in green are plotted the 1567 stars within *TESS* FOV and in red are plotted the 634 stars out of FOV.

Table 2: Number of stars for which we found 2 minute cadences in multiple sectors.

N_{sectors}	1	2	3	4	5	6	7	8	9	10	11	12	13
N_{stars}	871	160	99	52	15	7	7	2	4	3	4	20	5

In addition to the data from the first two cycles from *TESS* (sectors 1-26), we used the data from sectors 27 up to 33. These sectors correspond to the third cycle of observations, in which *TESS* is currently observing the southern hemisphere again.

During its third cycle, *TESS* keeps performing 2-min cadence photometry, but also performs a 20 second data collection for up to 1000 targets per sector. Of the 179 light curves we used from cycle 3, 65 were obtained with this 20 second cadence photometry.

3. Analysis

3.1. Rotation periods

Similarly to the Sun, stars can show cold, dark spots on their surface, an effect that is more prominent in cool stars. Therefore, drops in a star’s brightness can be interpreted as one of these spots aligning with the line of sight. If the lifespan of the dark spot is longer than the time it takes the star to complete a rotation, one might be able to observe a periodic variability of the brightness as the star rotates.

Since *TESS* provides photometric measurements of stars over time for almost a month, it is a great tool to observe these starspot modulations in the light curves and measure the rotational periods that might be present.

To compute the rotational periods of the sample, we used the Generalised Lomb-Scargle periodogram (GLS¹) presented and discussed in Zechmeister and Kürster (2009). This algorithm takes a time series as an input and computes a spectrum of possible frequencies, assigning them a power which marks its significance. Each peak of the periodogram has an associated false alarm probability (FAP) associated which gives information about the plausibility of the frequency: the closer to zero, the more reliable the frequency. Period uncertainties are calculated by fitting the periodogram peak to a Gaussian curve and taking the full width at half maximum (FWHM) as an estimation of the error.

¹<https://github.com/mzechmeister/GLS>

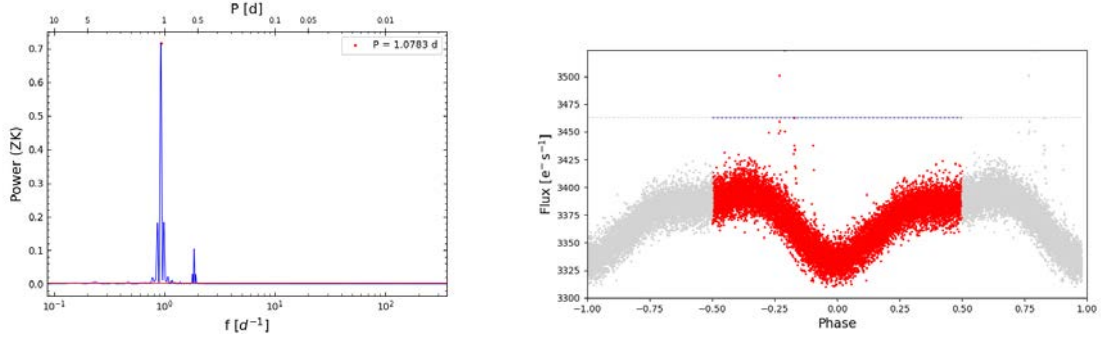


Figure 4: **Left:** GLS periodogram from the light curve of J00245+300 (Fig. 2). The bottom x axis marks the frequencies (in d^{-1}) and the top x axis marks the periods (in d). The y axis represents the power of the frequencies (with ZK normalization). The horizontal red lines mark the powers with FAP 1 %, 0.1 % and 0.01 %. **Right:** phase folded light curve for J00245+300 using the period of the highest peak (1.0783 d). The horizontal dotted line indicates the outlier cut to perform the GLS (5σ).

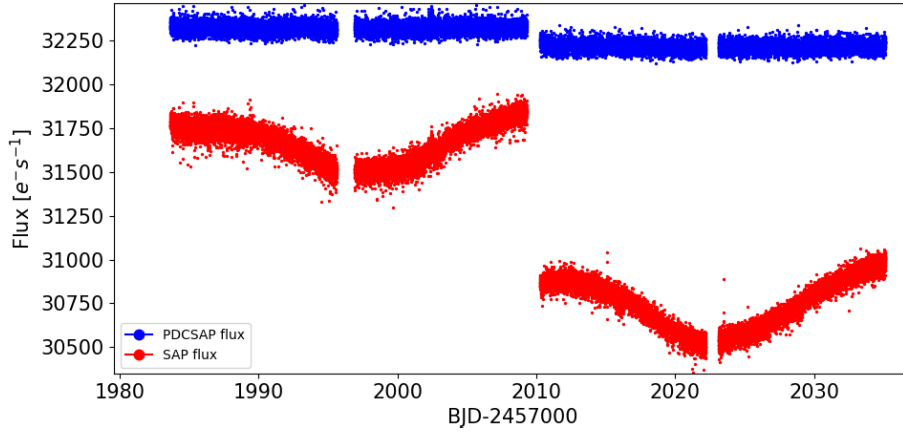


Figure 5: SAP and PDCSAP light curves for J00136+806=G242-048. The long periodic signal (~ 27 d) is removed by the pipeline, as it is optimized to search for transits. Thus, the period is impossible to recover from the PDCSAP flux.

The GLS algorithm was run on the PDCSAP and SAP light curves provided by the *TESS* pipeline. We constrained the algorithm to look for periods between 4 minutes and 13 days, which correspond to double the sampling rate (Nyquist frequency) and half the total observing time. This was done to ensure that two full signal repetitions were observed before acknowledging the period. Points further than 5σ above and below the light curve median were removed before running the GLS to prevent signals such as flares or eclipses to induce spurious signals in the periodogram. In a first iteration, the highest peak from each periodogram was selected as the candidate main rotational period.

For stars that could be found in multiple sectors, this was done individually in each sector, as *TESS* PDC pipeline can destroy long period signals as shown in Fig. 5. The rotational period was calculated averaging the output period of each individual valid sector.

To recover long period signals, the uncorrected SAP flux should be used as longer periods might be over-corrected by PDC. Some pipelines provide a method to calculate periods longer than the sector baseline for stars present in multiple sectors, such as SIP (Systematics-intensive Periodogram)¹, a tool designed specifically for *TESS* and presented by Hedges et al. (2020).

In this work we will not try to measure periods longer than 13 d and we join the observations in multiple sectors only to confirm single sector measurements, not with the intention of finding long periodicities.

¹<https://github.com/christinahedges/TESS-SIP>

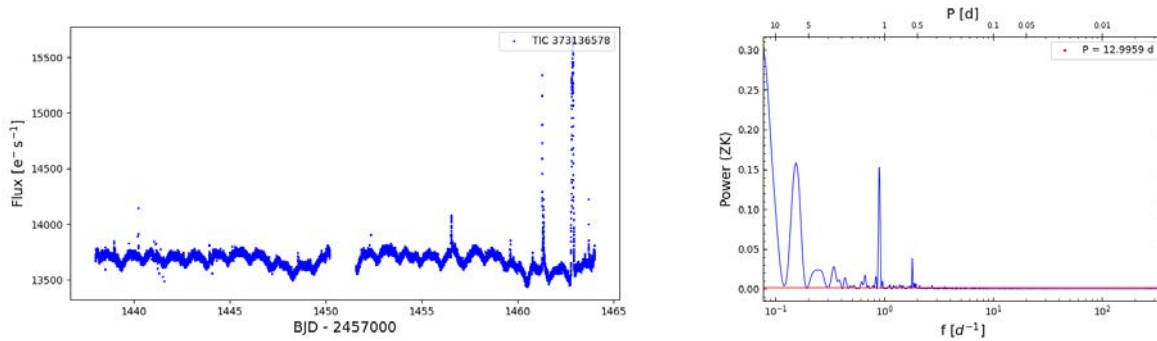


Figure 6: Light curve (left) and periodogram for J04350+086=StKM 1-495. In this case, the secondary peak at 1.1 d is correct while the highest peak at 13 d probably appears due to the gap in the sampling

Every light curve was phase folded using the highest peak of the periodogram as a means of testing the accuracy of the measured period. Fig. 4 shows an example of the GLS performing in the PDCSAP light curve for J00245+300 shown in Fig. 2 (sector 17) and the phase folded data using the highest peak as the period. The structure of the modulation seen in the phase folded light curve can give us a clue about the accuracy of the measured period.

In some particular cases, the period was selected from a secondary peak from the periodogram as the highest peak was not correct. An example is J04350+086 (StKM 1-495), which shows its higher peak at 13d and a secondary peak at 1.1 d, which is the correct one (see Fig. 6).

When the PDC routine made it ambiguous to determine if the measured period was real or an effect of correction, the SAP light curves were used as a double check.

If a star was observed in multiple sectors, we joined the data available for all sectors in a single light curve. This process was a bit tricky as the data could not be well aligned as shown in Fig. 2. We tried to join the data by putting the median flux of each light curve at the same level. Then, the GLS algorithm was run on the merged data, which was then phase folded using the resulting highest peak as the main period. This steps were followed not as a means of obtaining a long period, but to double check the results of individual sectors. As stated above, it is necessary to treat the data differently for that purpose and it escapes the objective of this work.

3.2. TESS masks and contamination

Each star that *TESS* observes with a short cadence has an associated aperture mask that is designed to optimize the S/N. Nevertheless, the *TESS* image scale and point-spread function (PSF) make it difficult to discriminate the light coming from individual sources with nearby physical or optical companions, specially in cases of crowding.

To make sure that the measured signal comes from the star of interest, we revised the TPFs of each star (individually in each sector). We identified *Gaia* DR2 sources near the star and compared their fluxes in *Gaia*'s *G* band using *tpfplotter*¹(Aller, A. et al. 2020): a tool developed in Python with this purpose. We then calculated the relative contribution of the star of interest compared to the total contribution of *Gaia* sources within the *TESS* aperture mask, as:

$$FG_{\text{ratio}} = \frac{F_G^*}{\sum A_i F_{Gi}} \quad (1)$$

where F_G^* and F_{Gi} are the *G*-band flux of the star of interest and of the i th star in the TPF and A_i takes the value 1 when the star is within the aperture mask and 0 when it is out of it. The summation is extended to all sources present in the TPF.

As shown in Fig. 7, *TESS* and *Gaia* *G*-band response functions cover a range in the electromagnetic spectrum that intersects in the spectrum of an M dwarf (with *Gaia* reaching into shorter wavelengths), so this procedure can be used as an indicator of how much of the light comes from the star of interest.

¹<https://github.com/jlillo/tpfplotter>

As *TESS* reaches further in the infrared, the brightness of M dwarfs could be even under-estimated using this procedure, which could restrict their FG_{ratio} more than needed.

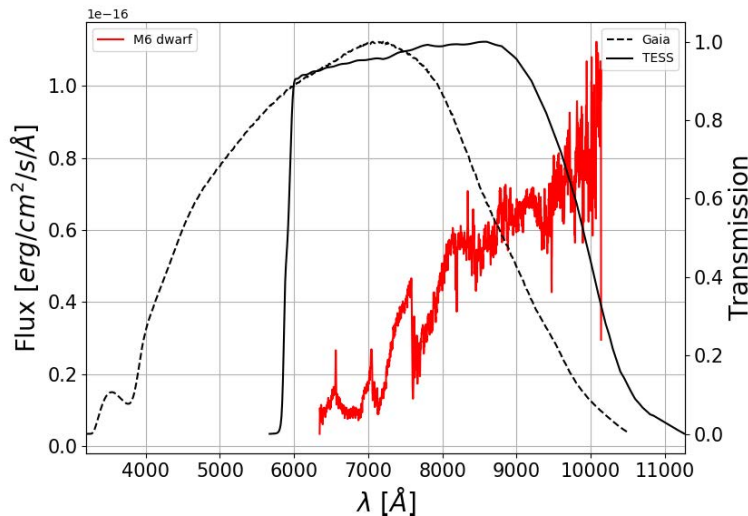


Figure 7: Typical M6 dwarf spectrum compared to *TESS* and *Gaia* DR2 G-band response functions. M dwarfs are brighter in *TESS* passband than in *Gaia*, as the brightest part of their spectra is out of the G-band.

In addition to this indicator, we used the TPFs to look for nearby bright sources. As *TESS* typical PSF encloses about 90 % of a star’s light within a square of 2×2 pix (about 42×42 arcsec²), light from a close star that is out of the aperture mask can sometimes have an effect on the light curve. To overcome this problem, we looked at individual TPFs when a source was present and was brighter than the main star by $\Delta G_{mag} = 3$, comparing the flux coming from pixels around both sources by defining different aperture masks. With this manual process, we could determine if the modulation (when present) was a product of our star or from a neighbor.

In some other cases, the observed star was found completely out of the aperture mask, and the light curve was obtained defining a new mask, as in the case of the double system J01390-179 (see Fig. 8). Fortunately, the few cases presenting this problem were found in a fairly empty field (their TPFs contained just the main star), so it was not difficult to define an aperture mask.

In Fig. 8, we show four examples of TPFs: J11376+587, J00515-229, J02462-049 and J03018-165S. The images show the aperture mask that the *TESS* pipeline assigned to each star (red squares). Marked with red circles are the *Gaia* DR2 sources found in the neighborhood of the interest star on the TPF, numbered in order of proximity to the main star (marked with 1). The size of each circle indicates the magnitude of the corresponding star compared to the main source. The first star has no nearby sources that can contaminate the light curve, so we can trust the obtained data. The mask defined for J00515-229 contains two sources within and a bright star next to it that can induce a signal in the light curve. The case of J02462-049 is that of a badly defined mask as the star is completely out of the aperture mask. The last panel shows a difficult case: J03018-165 is a binary system and both components lie approximately within the same pixel and are almost equal in brightness. What we see in their light curves is very similar. In cases like this one we assigned the rotation period (if found) to the brightest star if its FG_{ratio} was greater than 0.8 or if the obtained period was compatible with what was be found in the literature, as in the case of J03018-165S.

This manual approach was also used in cases where the `tpfplotter` tool could not produce a result, as some of the stars from our sample did not have a *Gaia* DR2 identifier associated.

3.3. Summary sheets

The basic information regarding all the light curves obtained from *TESS* was gathered in sheets that include four plots:

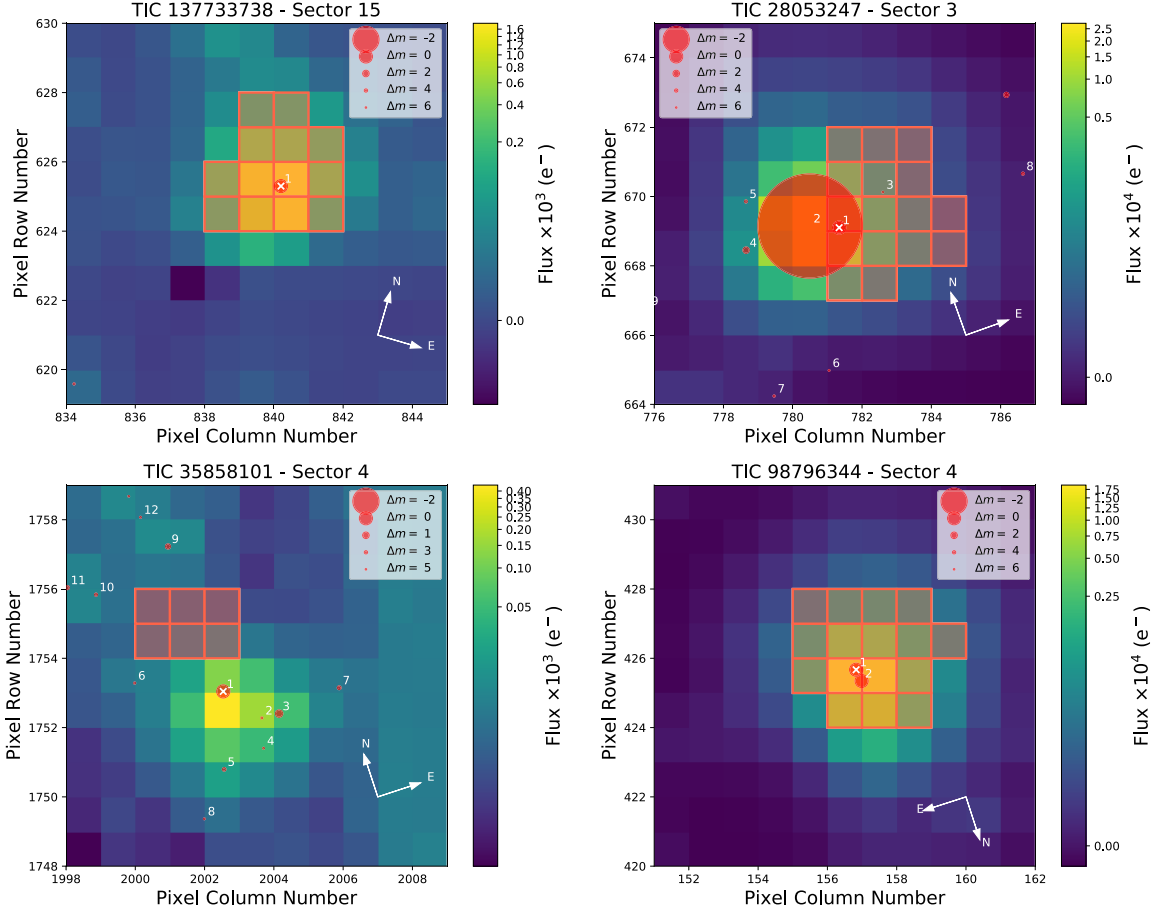


Figure 8: TPFs of J11376+587 (top left), J00515-229 (top right), J02462-049 (bottom left) and J03018-165S (bottom right). The aperture mask is drawn with red semi-transparent squares overlaying the corresponding pixels. Red circles indicate the *Gaia* DR2 sources found, their size indicating their magnitude relative to the main star and are numbered in order of proximity to it.

- **Top left:** one cadence of TPF with the mask used by the *TESS* pipeline and the stars in the *Gaia* DR2 sources, marked with red circles as in Fig. 8.
- **Top right:** The PDCSAP flux light curve. The time units are *TESS* Barycentric Julian Date (BJD) in days as in the right panel of Fig. 2.
- **Bottom left:** GLS periodogram with the highest peak marked as in the left panel of Fig. 4. The x axis units are frequency (bottom) in units of d^{-1} and period (top) in units of d . The y axis represents the power in a ZK normalization. The red horizontal lines indicate the power levels corresponding to false alarm probabilities (FAP) of 0.1, 0.01 and 0.001.
- **Bottom right:** the phase folded light curve using the highest peak as the main period as shown in the right panel of Fig. 4. In this representation, a red dashed line marks the 5σ clip that was used to remove the outliers. Only points within 10σ from the median were plotted. In red are plotted points from the original light curve, while in gray are plotted points duplicating the phase, so we show two whole modulations.

When a star had usable data for more than one observed sector, a diagnosis was generated for each sector individually. At the end, another sheet was added containing the combined light curve and periodogram obtained using all the data. This was not done when the observed sectors were observed in different *TESS* cycles because the time between the two observations is almost two years, enough for the star spots to change and potentially contaminate the periodogram.

These diagnosis sheets were used to quickly check the plausibility of measured rotation periods. A repository with a simple code that runs the GLS periodogram and generates a diagnosis sheet given TIC identifier and sector was uploaded to GitHub (https://github.com/SLSkrzypinski/TESS_diagnosis) and can be freely used.

The diagnosis sheets for some of the stars that are mentioned in this work can be found in Appendix B.

3.4. Detrending the light curves

In order to study flare activity present in the light curves, starspot modulations and other tendencies (cyclical or not) were removed using two methods depending on the characteristics of each light curve:

- Cubic splines in the general case.
- Fit to a Fourier polynomial in cases where the modulations were comparable in duration to a typical flare.

The splines fit was performed using a robust Huber estimator (Huber 1981) in order to reduce the impact of prominent outliers such as flares or eclipses in the case of binary systems. This method was carried out using the `exostriker`¹ Python library (Trifonov 2019), which also relies on the `wotan`² package (Hippke et al. 2019). As we did before running the GLS periodogram, outliers were removed using sigma-clipping before the detrending the light curve. The left panel of Fig. 9 shows the model for J06212+442 (G 101-035).

In some cases, the window length that must be used to fit a spline model that completely remove the starspot modulation is too short and becomes comparable with the duration of a flare. If flares present are not too prominent, this is not problematic. Nevertheless, sometimes splines try to fit the flare, lowering the energy that is measured or even masking it completely (see right panel of Fig. 9).

In the cases that were problematic, a Fourier fit was instead used to detrend the light curves.

¹<https://github.com/3fon3fonov/exostriker>

²<https://github.com/hippke/wotan>

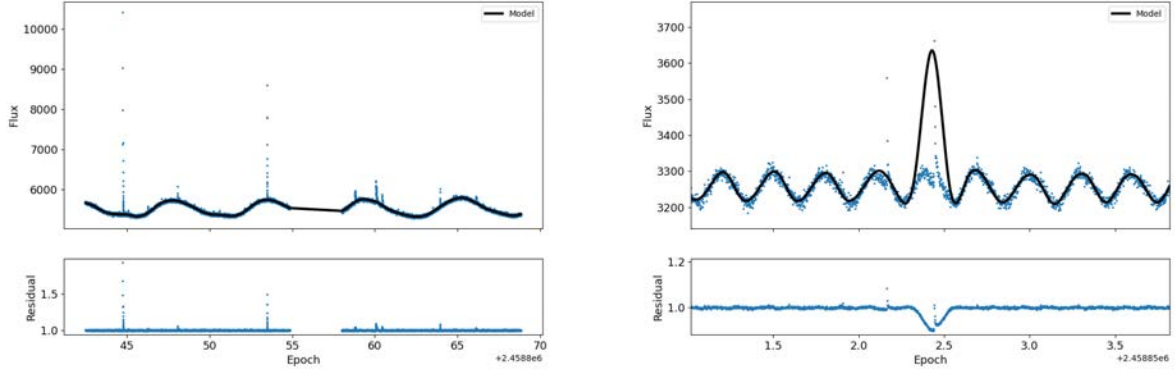


Figure 9: **Left:** Model and residuals obtained by fitting splines for J06212+442 using a window length of 0.5 d. **Right:** Same as left panel, but for J06318+414 (LP 205-044) and a window length of 0.1 d. The splines try to fit the strongest flare, but mask it instead.

3.4.1. Fourier fit

In those cases for which the spline detrending method was not sufficient, we used a Fourier fit to remove starspot modulations from the light curves. For this purpose, the light curve was phase-folded using the measured period P and duplicated so we had two complete modulations. We used the same sigma-clipping as before running the GLS periodogram and spline-fitting to remove outliers. Then, we fitted the resulting light curve to a polynomial of the form:

$$F_{\text{fit}}(\phi) = A_0 + \sum_{n=1}^m \left(A_n \sin \frac{n \cdot \phi}{P} + B_n \cos \frac{n \cdot \phi}{P} \right) \quad (2)$$

with A_n and B_n being the $2m$ free parameters and A_0 being the mean flux. Here, $F_{\text{fit}}(\phi)$ indicates the fitted flux at phase ϕ .

To assure that we use the right number of parameters, we used the lag-autocorrelation of Deb and Singh (2009). This function is defined as:

$$\rho = \frac{\sum_{j=1}^N (\nu_j - \hat{\nu}) (\nu_{j+1} - \hat{\nu})}{\sum_{j=1}^N (\nu_j - \hat{\nu})^2} \quad (3)$$

where ν_j is the j th residual of the fit, $\hat{\nu}$ is the mean residual and N is the number of observations.

To make sure that we choose the right polynomial order, the fit was performed so that the lag-autocorrelation was smaller than a cut value set to be (Baart 1982):

$$\rho_c = \frac{1}{\sqrt{2(N-1)}} \quad (4)$$

We started by fitting a polynomial with $m = 2$ and increased the order of the fit until either $\rho \leq \rho_c$ or $m = 17$. The latter condition was imposed to save computing time as the fit starts taking too long and the information that can be retrieved from it is not very useful.

Once the optimal fit was reached, it was extended to the original light curve and subtracted from the data, obtaining the residuals.

An example of this fit can be found in Fig. 10, which shows the detrending of J06318+414. For this particular star, the spline detrending was not possible as the window length that was needed to remove the modulation was too short, masking some flares (see Fig. 9).

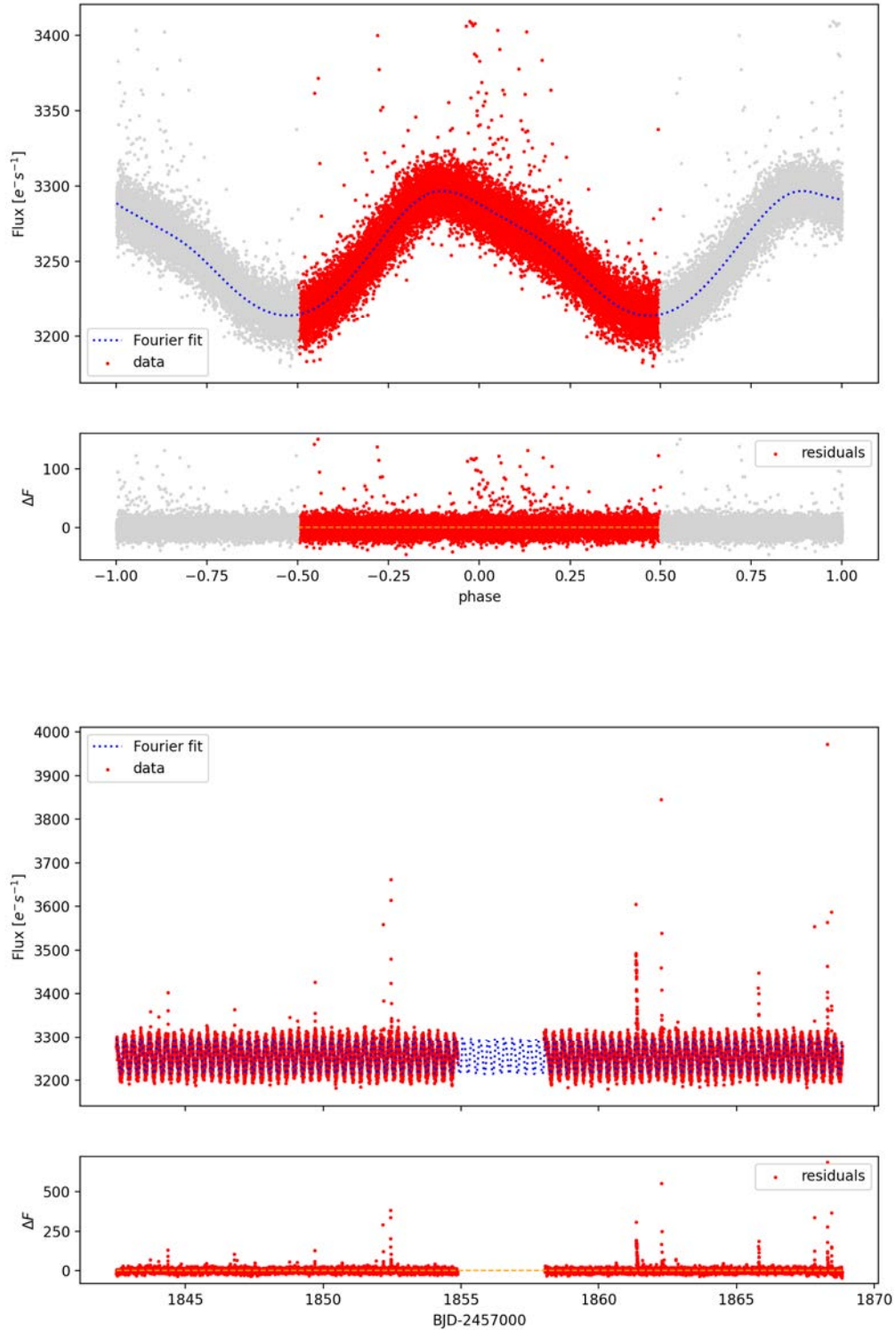


Figure 10: Example of our Fourier fit with 7 terms for J06318+414 (LP 205-044) with a measured period $P = 0.3$ d. We fit a Fourier polynomial to two phases of the light curve (top two plots) and then extend it to the original data in the time space (bottom two plots). Both panels show the data on the top and the residuals on the bottom.

3.5. Stellar flares

3.5.1. Identification

Flares were identified once the light curves were flattened using a Fourier fit. The median and dispersion of the flattened light curve were computed each 128 points (~ 2 h), which is of the order of the duration of a flare. For an outburst to be flagged as a flare, three or more data points need to lie 2σ above the local median and at least one of them must be above 3σ . This method is similar to the sigma clipping used by Günther et al. (2020). The peak point was selected as the maximum height in a 40-point-neighborhood around the flagged points. We also imposed the condition that $t_{\text{decay}} > t_{\text{rise}}$, where t_{rise} and t_{decay} are the flare rise and decay times. This last condition is imposed due to the typical shape of a flare consisting on a sudden rise in brightness followed by a longer exponential decay, excluding events as cosmic rays or solar system objects crossing the camera (see below).

Starting and ending points were defined using the flux variation distribution. For each consecutive pair of data points we obtained the flux variation as $\delta F_j = F_{j+1} - F_j$. This δF distribution has a mean $\hat{\delta F}$ and a standard deviation σ_{diff} . The starting point of a flare is defined as the first point j before the peak for which δF_j is larger than 1.5 times the top 1% from the distribution. The ending point was defined as the first point of the flattened light curve after the peak that is closer than $1\sigma_{\text{diff}}$ to the residuals' local median. This same method was discussed in depth by Shibayama et al. (2013), although it was used for *Kepler* data and the ending point was defined as the first point closer than $3\sigma_{\text{diff}}$ to the median.

This method is quite restrictive regarding small flares. The sigma clipping used in addition to the condition that δF_j must be 1.5 times larger than the top 1% of the distribution δF makes it difficult to identify small flares as such, as they are masked by noise. Additionally, when large flares are followed by smaller ones, the latter are masked as the local median is dramatically raised by the largest flare, thus the sigma clipping fails to flag the small flares. These limitations were an accepted risk in exchange of making the process of identifying flares as automatic as possible.

False positives can also be a problem. For instance, Solar System objects can sometimes cross the aperture mask of a star and can be flagged as a flare. This type of events have a particular shape as shown in Fig. 11, which presents an event of this kind for J01009-044 (GJ 1025) observed in sector 30. Panel 1 shows the star and its aperture mask in a normal state. As the object crosses background pixels, its brightness is subtracted from the flux of the mask (panels 2 and 3), creating a dip in the light curve. As light from the object enters the aperture mask (panel 4), a sudden rise followed by a quick decay (panel 5) appears in the light curve. More examples of this case can be found in Appendix C. The condition $t_{\text{decay}} > t_{\text{rise}}$ should get rid of these kind of events, but light curves were inspected to manually remove false flare flags to be sure.

3.5.2. Flare energy estimation and power law

The energy of each flare was estimated using each star's effective temperature (T_{eff}) and radius (R_*) as tabulated by Cifuentes et al. (2020). For stars for which some data was not found in this database, we used the values from TICv8.

Flares were modeled as a black body with $T_{\text{flare}} = 9000$ K, as in Yang et al. (2017) and Günther et al. (2020). The energy was calculated using the luminosities of the star and the flare in the *TESS* passband (Fig. 7):

$$L'_* = \pi R_*^2 \int R_\lambda B_\lambda(T_{\text{eff}}) d\lambda \quad (5)$$

$$L'_{\text{flare}} = A_{\text{flare}}(t) \int R_\lambda B_\lambda(T_{\text{flare}}) d\lambda \quad (6)$$

where $B_\lambda(T)$ is the Planck function for a temperature T , R_λ is the *TESS* response function (Ricker et al. 2014) and A_{flare} is the flare surface area. Here, we assume $L'_{\text{flare}}(t)/L'_* = \Delta F(t)/F_*$, with $\Delta F(t)$ the flux of the flare obtained by subtracting the model to the flux at the time of the flare t and F_*

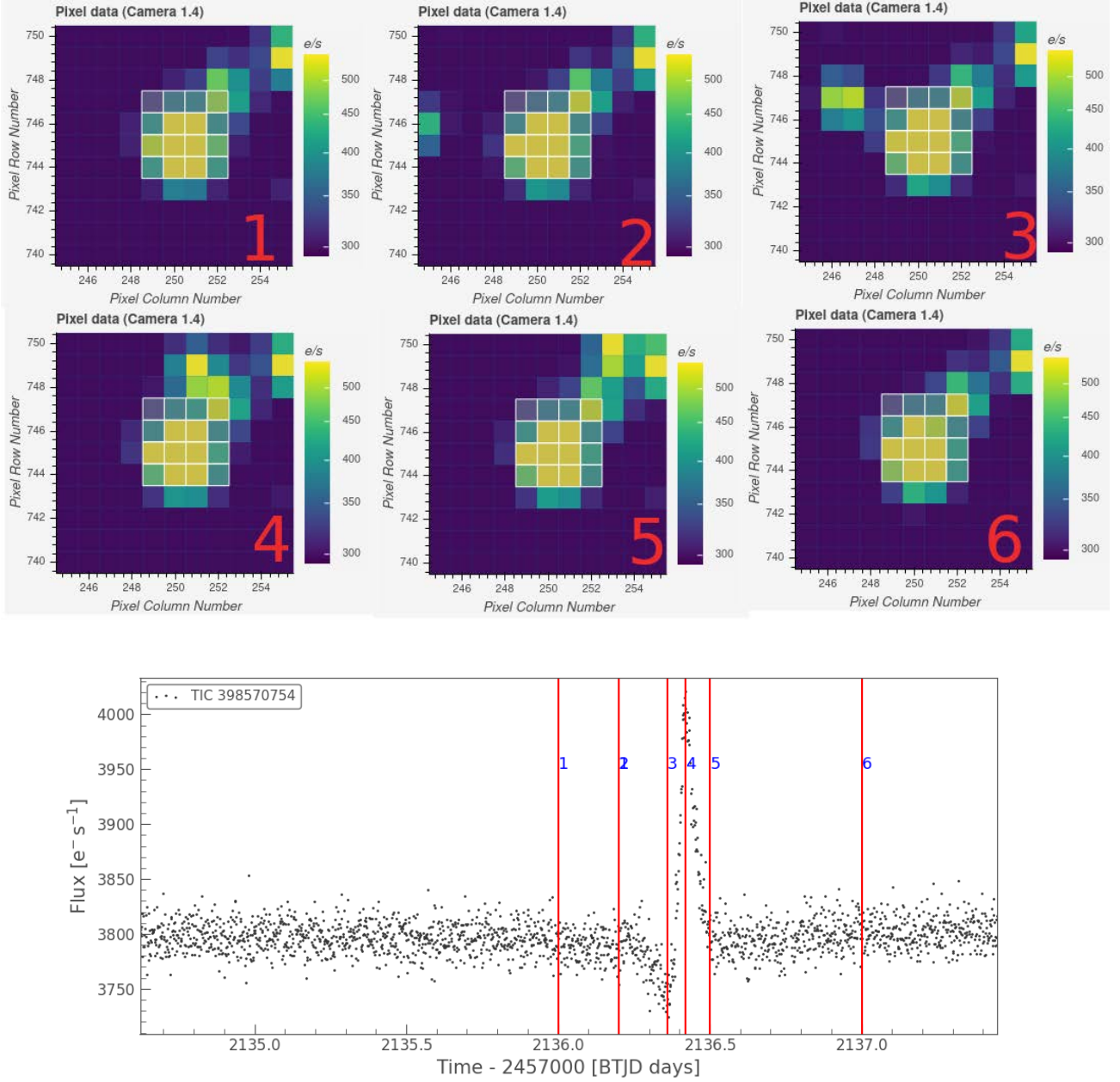


Figure 11: A Solar System object crossing the aperture mask of J01009-044 and generating a signal that could be identified as a flare. As light of the object enters the aperture mask (marked with white pixels), a rise in flux can be confused with a flare.

the model at the same time. Equations 5 and 6 can then be solved for A_{flare} as:

$$A_{\text{flare}}(t) = \frac{\Delta F}{F_*}(t) \pi R_*^2 \frac{\int R_\lambda B_\lambda(T_{\text{eff}}) d\lambda}{\int R_\lambda B_\lambda(T_{\text{flare}}) d\lambda} \quad (7)$$

The bolometric flare luminosity can then be written as:

$$L_{\text{flare}} = \sigma_{SB} T_{\text{flare}}^4 A_{\text{flare}} \quad (8)$$

And the total flare energy is:

$$E_{\text{flare}} = \int_{t_{\text{beg}}}^{t_{\text{end}}} L_{\text{flare}}(t) dt \quad (9)$$

All the integrals were solved using a Simpson's rule on the *TESS* data.

Once we estimate the energy of found flares, we saw how this energy is distributed and compared this distribution to what we would expect.

The energy distribution of stellar flares has been described by power laws since the beginning of their statistical properties (Lacy et al. 1976). Although some recent studies have proposed different distributions (for instance, Verbeeck et al. (2019) proposed a lognormal distribution), the power laws are still widely used to describe flare distributions. These distributions take the form:

$$dN \propto E^{-\alpha} dE \quad (10)$$

where dN is the number of flare events with energy between E and $E + dE$. This means that the number of events with energy greater than a certain value E_c can be written as:

$$N(E > E_c) \propto E_c^{1-\alpha} \quad (11)$$

Taking logarithms at both sides of Eq.11 it is obvious that a linear relation with slope $(1 - \alpha)$ exists between the energy and the cumulative number of events. We can then measure the value of α by means of a simple linear fit to the obtained data. This process of fitting the logarithms of both sides of a power law to a straight line has been discussed and better methods have been proposed, like maximum likelihood estimators (see for example Ryan et al. (2016)), but our method can be used as a fair approximation.

The value of α has some implications regarding coronal heating (Hudson 1991, Einaudi and Velli 1999, Georgoulis and Vlahos 1996). An exponent $\alpha \geq 2$ makes it possible for flares to be the main coronal heating mechanism. If $\alpha < 2$, the strongest flares would be too rare to be responsible for coronal temperature in its quiescent state.

If a power law as Eq.10 correctly describes a flare energy distribution, the total energy for a given time interval is:

$$E_{\text{tot}} = \int_{E_{\text{min}}}^{E_{\text{max}}} \frac{dN}{dE} E dE = \frac{k}{-\alpha + 2} (E_{\text{max}}^{-\alpha+2} - E_{\text{min}}^{-\alpha+2}) \quad (12)$$

where E_{min} and E_{max} are the minimum and maximum energy flare events in the time interval and k is an arbitrary constant. If $\alpha > 2$ and $E_{\text{max}} \gg E_{\text{min}}$, then Eq.12 leads to:

$$E_{\text{tot}} \approx \frac{k}{\alpha - 2} E_{\text{min}}^{-\alpha+2} \quad (13)$$

The total energy that can be released from flare activity then can be arbitrarily high as it diverges for $E_{\text{min}} \rightarrow 0$.

Empirical data have led to α values around 2. From *Kepler* and K2 data, Shibayama et al. (2013) found α to be in the range 2.0-2.2 for solar-type stars. On the other hand, Gizis et al. (2017) obtained $\alpha = 1.8 \pm 0.2$ for an M8 dwarf over the range 10^{31} to 10^{33} erg using data from K2, which would deny flares as a main coronal heating mechanism. Ilin, E. et al. (2019) determined α to lie between 2.0 and 2.4 for all type of stars, independently from stellar age or mass.

It is remarkable that all these results are very close to the critical value of 2 and contradict each other, keeping the question about coronal heating open.

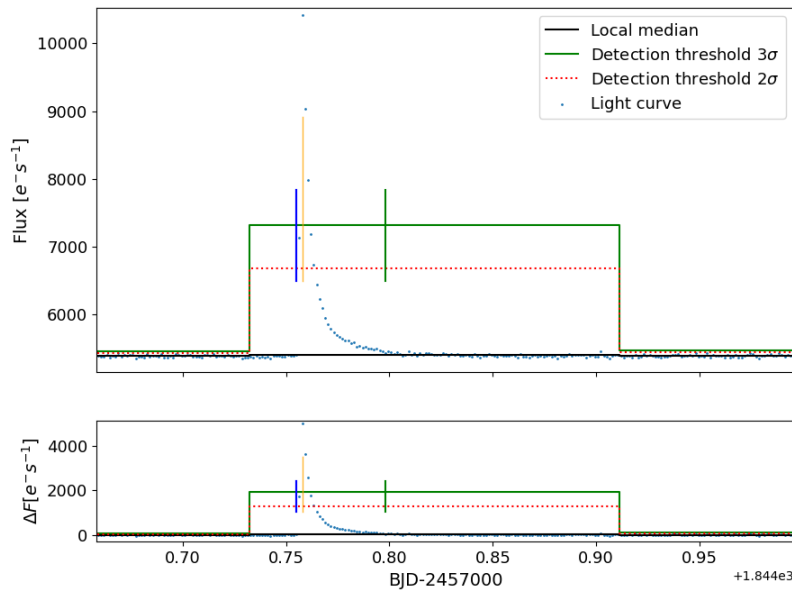


Figure 12: A flare detection example for J06212+442 (G 101-035). The top panel shows the original data, while the bottom panel shows the residuals. Vertical lines mark the beginning of the flare (blue), peak (yellow) and ending (green).

4. Results

4.1. Periods

Using the SAP and PDCSAP light curves, we found 244 reliable periods ranging between 0.11 d and 10.52 d. Every period that we found to be reliable (see below) is shown in Table A.1. More than half of the found periods (64 %) are shorter than 2 days (see Fig. 13). This is mostly due to *TESS* baseline and observation cadence added to the fact every light curve has a gap at around half of each sector baseline as *TESS* repositions itself, making it difficult to find periods longer than 6 days.

The light curves that we considered as valid for period measurement have a false alarm probability below 0.1 % in the periodogram peak and show a clear structure when phase folded. The observed star also needs to be sufficiently isolated ($FG_{\text{ratio}} > 0.8$) for the signal to be considered as valid, unless we could check with the literature.

Of the 244 stars for which we found a reliable period, we could find 123 period counterparts in the literature, with 16 showing significant differences. In addition, 37 periods were previously measured by Revilla (2020) using the same methods that are used here (but only for GTO stars), 11 of which were new. Thus, we present 110 new rotational periods for the CARMENES sample.

We show the relation between the periods we obtained and those found in the literature as a consistency test in Fig. 13, finding that the periods that we measured mostly agree with the literature with the exceptions shown in Table 3. In that table, stars that show a discrepancy with the literature value more than 10 % are listed except for those that fall near the relations $P_{\text{rot}} = 2P_{\text{lit}}$ or $P_{\text{rot}} = P_{\text{lit}}/2$, as in those cases one measurement could be an alias of the other. Stars shown in Table 3 are plotted in Fig. 13 with red labeled dots.

Another consistency test that can be run on our data is comparing the rotational periods and the rotational velocities obtained using spectroscopy ($v \sin i$). The rotational velocity quantifies the speed at which a point at the surface of the star is moving due to the rotation and is related to the rotation period via the radius of the star:

$$v \sin i = \frac{2\pi R_* \sin i}{P_{\text{rot}}} \quad (14)$$

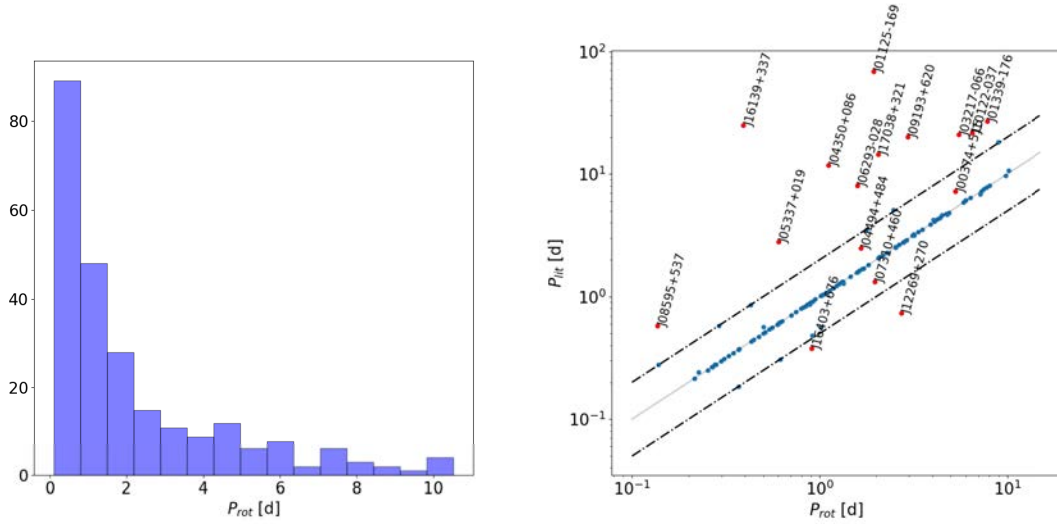


Figure 13: **Left:** distribution of found rotational periods. Most periods found are shorter than 2 days. **Right:** rotation periods obtained with *TESS* compared with what was found in the literature (blue and red dots). The lines corresponding to the 2:1 and 1:2 relations are plotted with dashed lines and the 1:1 relation with a gray line. Red labeled dots indicate stars for which we found major discrepancies with literature values.

where R_* is the radius of the star.

This quantity depends on the orientation of the star with respect to the observer (i) and can be used to determine this angle of orientation if $v \sin i$ and P_{rot} are known alongside with R_* . It can be used to check if the measured period of a star falls within what would be expected from its $v \sin i$ measurement, as we do in Fig. 14.

In Fig. 14 we plot the rotational period we obtained with *TESS* photometry and their corresponding $v \sin i$ value if we found one. The dashed lines indicate conservative limits obtained with Eq.14, with the vertical width coming from the indetermination in the inclination angle i and the different radius R_* . The horizontal line at long periods and low $v \sin i$ is there due to instrumental limitations when measuring velocities below $2 \text{ km} \cdot \text{s}^{-1}$.

There are six outliers in Fig. 14 that are out of the envelope defined by the dashed lines. The most prominent are:

- J04173+088 (LTT 11392): we measure $P_{\text{rot}} = 0.37 \text{ d}$, which seems slow for its rotational velocity $v \sin i = 190.3 \text{ km} \cdot \text{s}^{-1}$ (Jeffers et al. 2018) and radius $R_* = 0.278 R_{\odot}$. The period measured by us is twice the one measured by West et al. (2015) (0.185 d), but this period is still insufficient to explain the large $v \sin i$.
- J14549+411 (LP 222-015): we measure $P_{\text{rot}} = 6.014 \text{ d}$, which again seems too slow given its rotation velocity $v \sin i = 44.1 \text{ km} \cdot \text{s}^{-1}$ (Gilhool et al. 2017) and radius $R_* = 0.554 R_{\odot}$. Hartman et al. (2011) gives a rotation period of 6.11 d, which does not differ significantly from our measurement.

We do not list the other four outliers here as their $v \sin i$ values found in the literature are upper limits ($v \sin i < 8 - 20 \text{ km} \cdot \text{s}^{-1}$). Thus their true value could be lower than shown.

4.2. Activity

4.2.1. Flares in rotating stars

We looked for flare activity in those stars for which we found a reliable rotation period (Table A.1). Unresolved multiple systems (EB, SB) were left out of the analysis due to the fact that we cannot discern which star flares come from, which would affect the analysis. Resolved multiple systems were

Table 3: Stars for which we found a rotational period significantly different than the period found in the literature.

Karmn	Name	P_{rot} (d)	P_{lit} (d)	Reference
J00374+515	G 172-014	5.295	7.2	Hartman et al. (2011)
J01125-169	YZ Cet	1.937	69.2	Díez Alonso et al. (2019)
J01339-176	LP 768-113	7.553	27.1	Díez Alonso et al. (2019)
J03217-066	G 77-046	5.528	21.1	Díez Alonso et al. (2019)
J04350+086	StKM 1-495	1.116	11.76	Kiraga (2012)
J04494+484	G 081-034	1.660	2.49	Hartman et al. (2011)
J05337+019	V371 Ori	0.605	2.81	?
J06293-028	V577 Mon AB	1.585	8.1	Mascareño et al. (2016)
J07310+460	1RXS J073101.9+460030	1.964	1.33	Hartman et al. (2011)
J08595+537	G 194-047	0.136	0.581	Newton et al. (2016)
J09193+620	LP 091-014 AB	2.943	20.2	Shkolnik et al. (2010)
J10122-037	AN Sex	6.485	21.6	Díez Alonso et al. (2019)
J12269+270	CX Com	2.722	0.733	Newton et al. (2016)
J16139+337	σ CrB Cab	0.392	24.948	Hartman et al. (2011)
J16403+676	LP 069-457	0.907	0.38	Irwin et al. (2011)
J17038+321	LP 331-057	2.053	14.54	Hartman et al. (2011)

also ignored if two or more stars of the system were found within the same aperture mask and both stars' brightness were comparable.

We found 2567 flares in 179 rotating stars. Measured energies range between $7.35 \cdot 10^{29}$ erg and $1.51 \cdot 10^{35}$ erg. The data are complete and follows a linear relation for energies greater than 10^{33} erg (see Fig. 15). Smaller flares are difficult to identify as such due to data noise and the fact that the automated searching method described in Section 3.5.1 has difficulties identifying small flares as such when they are surrounded by larger ones.

The largest flare found belongs to J23083-154 (HK Aqr) which was observed in sectors 2 (cycle 1) and 29 (cycle 3). The flare event in question happened at $BJD = 2459105.39$ (sector 29). This is a M0.0 V star for which we obtained $P_{\text{rot}} = 0.431$ d, which is the same as measured in Kiraga (2012). The $v \sin i$ of this star is 69.4 km s^{-1} and the pseudo-equivalent width of the $H\alpha$ line is -1.8 \AA . The rotation velocity is consistent with the measured period, but the activity suggested by $pEW(H\alpha)$ is not among the largest of our sample. The diagnosis sheet for this star can be found in Appendix B.

A linear fit using least squares was performed on the cumulative frequency distribution for energies greater than 10^{33} (Fig. 15), obtaining a value $\alpha = 2.095^{+0.043}_{-0.059}$. The uncertainties come from varying the limit in the lower energy that is used to perform the fit, as this is the major source of error.

The value of α that we obtained would be marginally consistent with the idea that microflares are able to heat the corona. This result is not very strong as the exponent α that we obtained here is very close to the critical value of 2.

4.2.2. Dependence with spectral type

In the previous section we fitted the flare frequency distribution for all rotating single stars to a power law, obtaining an exponent close to 2. Now, we try to fit a power law to the flare frequency distribution of the same stars, but separating them into spectral types.

In Fig. 16 we show the fit for three spectral types groups:

- From M0V to M2V, obtaining $\alpha = 1.875$.
- From M2V to M4V, obtaining $\alpha = 2.122$.
- From M4V to M6V, obtaining $\alpha = 2.283$.

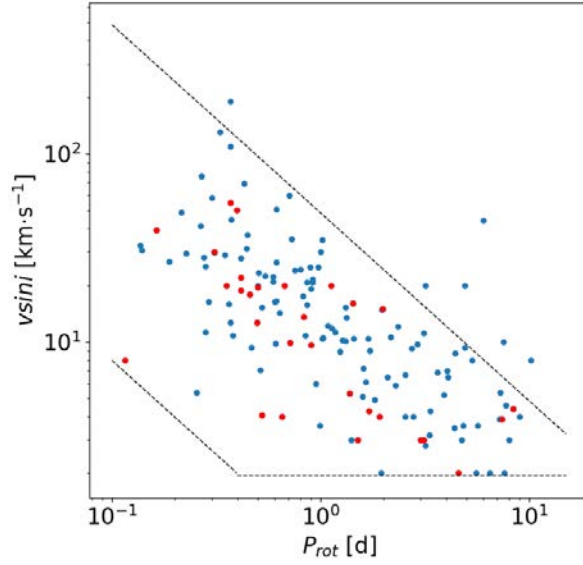


Figure 14: $v \sin i$ plotted against the new rotation periods (red) and the recomputed ones (blue). Dashed lines represent a conservative envelope to the limits using Eq.14.

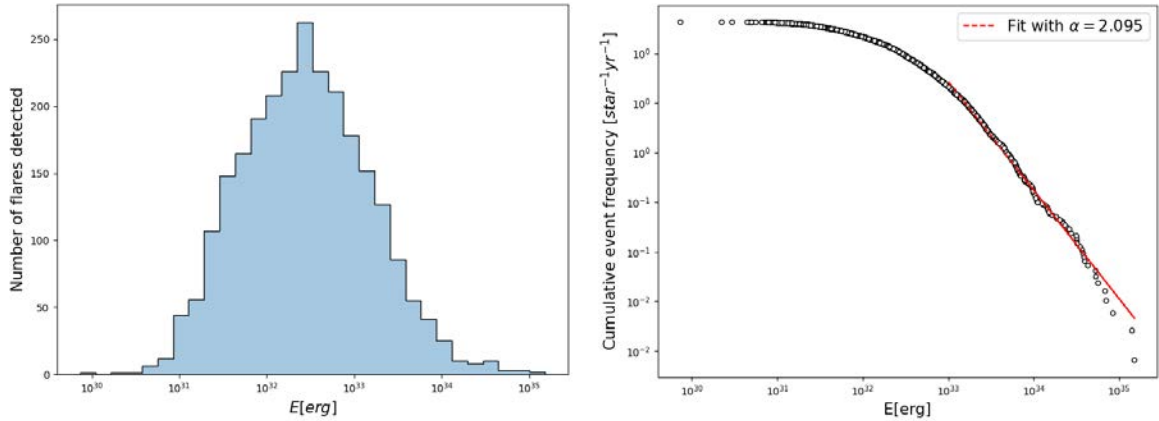


Figure 15: **Left:** number of flares detected compared to their energy. Below $E = 10^{13}$ the flares are poorly sampled. **Right:** cumulative flare frequency distribution and the linear fit using $E > 10^{13}$ erg.

Stars spectral types later than M6 V were not included in the analysis as the number of flares recovered became very small.

What we see from these results and Fig. 16 is that it seems to exist a relation between spectral type and the steepness of the flare frequency distribution. Late types seem to show a steeper distribution, with a transition from $\alpha < 2$ to $\alpha > 2$ before and after M2V spectral type. This result is not consistent with Ilin, E. et al. (2019), who found α to be independent of mass (and, consequently, spectral type).

4.3. Relation rotation-activity

4.3.1. Activity indicators

Jeffers et al. (2018) stated that in the CARMENES sample, there exists a correlation between the rotation and activity indicators, such as $H\alpha$ line or X-ray emission, finding that fast rotators tend to have higher magnetic activity.

Following this result, we compared the rotation periods obtained and those found in the literature with the $H\alpha$ pseudo-equivalent width ($pEW(H\alpha)$) values tabulated in Carmencita. The value of

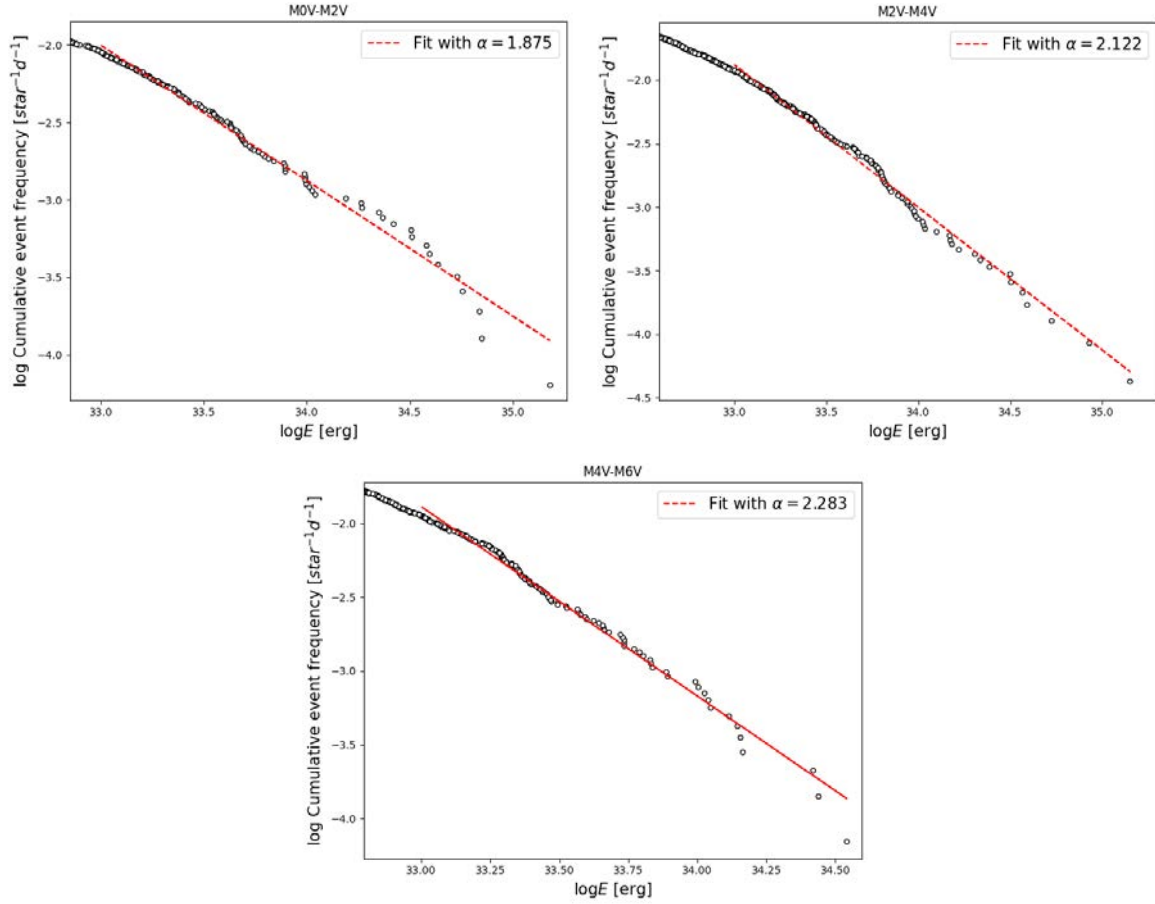


Figure 16: Flare frequency distributions for M0 V to M2 V stars (top left), M2 V to M4 V (top right) and M4 V to M6 V (bottom). We show the fit performed and the α value obtained in each case.

$pEW(H\alpha)$ measures the strength of the $H\alpha$ line: negative values are considered product of an active star (there is emission in the line) while positive values indicate that the star is inactive (the line is seen in absorption).

In the left panel of Fig. 17 we show the variation of the emission in the $H\alpha$ line with the rotational period. As found in Jeffers et al. (2018) and Díez Alonso et al. (2019), we find a negative correlation between rotation period and emission in the $H\alpha$ line: shorter periods tend to come from higher activity stars (more negative $pEW(H\alpha)$).

This result is mostly qualitative and must be taken with caution. We are biased towards short periods and lack for a bigger sample of slowly rotating stars. Nevertheless, the trend that our data follows seems to agree with what was found in the literature. The most prominent outlier is J06509-091, for which we got a period of 0.115 d while its equivalent width is low (Alonso-Floriano et al. 2015 tabulated $pEW(H\alpha) = -0.3 \text{ \AA}$). We included this star in our list of periods because we measured the same period in sectors 6 and 33 (see Appendix B).

Another activity indicator that can be used is the ratio of luminosities in X-rays and in the J band, L_X/L_J . We expect that fast rotators are more active stars and therefore have a higher emission in X-rays. We show this relation in the right panel of Fig. 17, observing that this relation holds true with two prominent outliers in short periods and low L_X/L_J : J03112+011 (1RXS J031114.2+010655) and J08595+537 (G 194-047). For both of these stars we measure a short period but their X-ray emission seems too low.

4.3.2. Flare activity and rotation

For the stars with measured rotation periods that show flaring activity, the flare frequency was calculated as the ratio between the number of flares observed and the total time that the star was

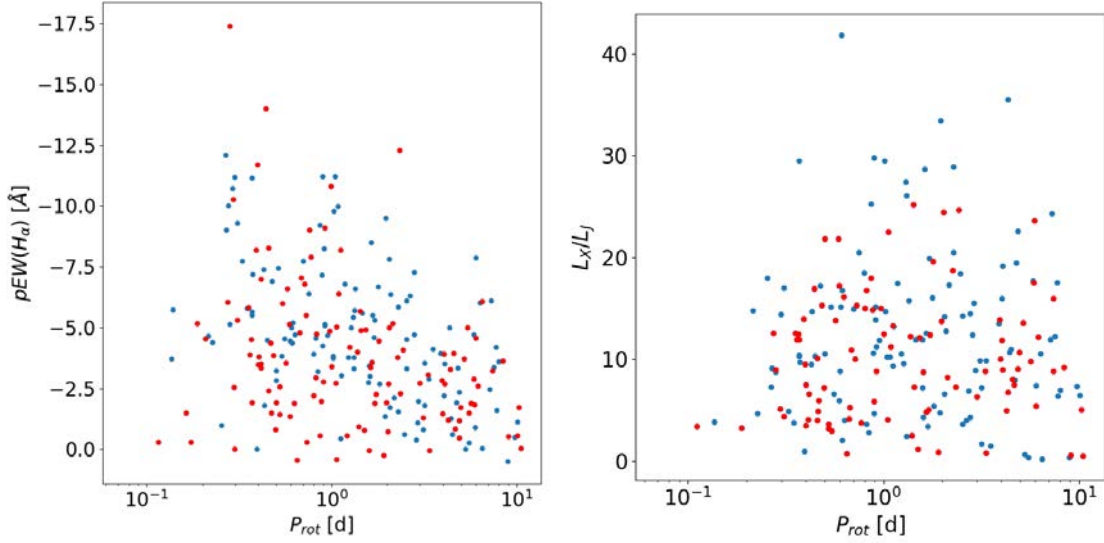


Figure 17: **Left:** variation of $pEW(H\alpha)$ with the measured period. **Right:** variation of the relative X-ray luminosity with the measured period. In both panels, red dots indicate the new P_{rot} while the blue dots mark the recomputed ones.

observed with *TESS* (in days). Fig. 18 shows a similar pattern to what was discussed in the previous section (Fig. 17): faster rotators tend to be more active stars. Fig. 18 also shows the flare frequency against the pseudo-equivalent width of the $H\alpha$ line. The relation here is more clear: stars that flare the most are also the stars that show more activity in the $H\alpha$ line.

Fig. 17 and the left panel of Fig. 18 show the same trend, but they must be looked taking into account that the slowest rotator we measured has a P_{rot} of 10.5 d, which is not too slow. In general stars rotating slower than ~ 10 d tend to be far less active, with low emission in $H\alpha$ (or even showing an absorption feature) and low X-ray luminosities. We would expect the same with the flaring rate. Unfortunately, given the *TESS* baseline we cannot reach into slow-rotating stars, which would give us a greater insight in this subject.

4.4. Multiple systems

Some of the light curves obtained from *TESS* data belong to systems containing multiple stars, including eclipsing (EB) and spectroscopic binaries (SB). Neither the EB nor the SB binaries were studied for flare activity. These cases were treated with special care and were inspected one by one. We were able to assign a rotational period to one of the stars when the system was widely separated or when the contribution of one of the stars was significantly higher (one of the stars holds more than $> 80\%$ of the light) when they were not.

In those cases for which the system is not resolved (EB and SB), we can only be sure that the signal of a period comes from one of the stars, but cannot firmly state from which one. In these cases, we propose a rotational period for the system, not specifying a particular star.

It is also worth to mention that some eclipses were found in five light curves corresponding to known multiple systems: J03372+691 (LP 054-019AB), J07418+050 (G 050-001), J09193+620 (LP 091-014 AB), J15474+451 (LP 177-102 AB) and J16343+571 (CM Dra Aab). Of these systems, only two were previously confirmed to be eclipsing binary systems: LP 054-019 and CM Dra. The other three systems were previously known only to be spectroscopic binaries. In addition, we found possible eclipses in J13348+201 (LP 379-062), previously thought to be a single star. In at least one case, J07418+050 (G 050-001), the EB is the subject of a forthcoming publication (Morales et al. in prep.).

In some multiple systems, the *TESS* light curve shows that there are more than one period present, which could be hinting that the observed star belongs to a multiple system. These cases are listed in Table 4 alongside with stars that show eclipses in their light curves. The third column of Table 4 shows

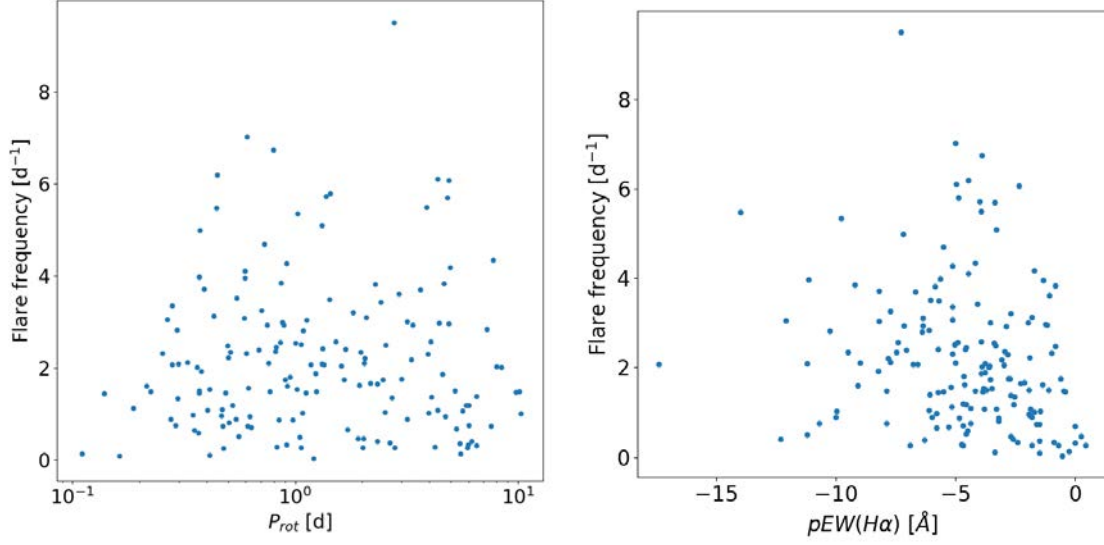


Figure 18: **Left:** flare frequency plotted as against the rotational period. The relation is not clear because stars with $P_{\text{rot}} > 10$ d are not represented. **Right:** flare frequency distribution as a function of $pEW(H\alpha)$.

Table 4: Systems for which we found hints of multiplicity in their TESS light curves. The third column indicates the previously known multiplicity of the system and is left blank if the star is a known single system.

Karman	Name	Multiplicity	Remarks
J01221+221	G 034-023	Resolved physical	Double period
J01437-060	BPS CS 22962-00111	SB2	Eclipse
J03372+691	LP 054-019AB	EB + SB2	Eclipses
J03147+114	RX J0314.7+1127	...	Double period
J04056+057	[R78b] 256 AB	Resolved physical	Double period
J04393+335	RX J04393.4+3332B	Wide + Resolved physical	Double period
J05019+099	LP 476-207 AB	Resolved physical + SB	Double period
J07295+359	1RXS J 072931.4+355607	Wide + Resolved physical	Double period
J07418+050	G 050-001	SB2	Eclipses
J09193+620	LP 091-014 AB	SB2	Eclipses
J11421+267	Ross 905	...	Eclipses
J13260+275	GUVVJ132602.6+273502.3	...	Eclipses
J13348+201	LP 379-062	...	Eclipses
J15009+454	BD+45 2247	Resolved physical	Double period
J15126+457	G 179-020	Resolved physical	Double period
J15474+451	LP 177-102 AB	SB2	Eclipses
J15499+796	LP 022-420	...	Double period
J15597+440	RX J1559.7+4403	Wide	Double period
J16343+571	CM Dra Aab	Wide + EB	Eclipses

the known multiplicity of the system as compiled in Carmencita. The labels “Resolved physical” and “Wide” mean that the system is physically bound and that their components are less than 5 arcsec or more than 5 arcsec apart. The study of multiplicities for stars with double periods and eclipses is left for future work.

From the eclipsing binaries that we found, five had a rotation period very close to the orbiting period, meaning that they were coupled. This is the case of, for example, J09193+620 (see Appendix B). This phenomenon is not uncommon for closely orbiting stars and usually even synchronizes both rotational periods with the orbiting period.

5. Conclusions and future work

Using 2-minute cadence data from *TESS* sectors from 1 to 33, we measured 244 rotational periods of the CARMENES Input Catalog stars, 110 of which are reported here for the first time. All the measured periods fall between 0.1 and 10 d, as longer periods are difficult to recover using *TESS* data. A careful analysis was carried out to determine that the periodic signals had their origin on the correct star using the TPFs. Of the 134 remeasured periods, 16 are not compatible with previous measurements and their aliases (Table 3).

The relations of the computed periods with $v \sin i$ and activity indicators follow the expected trend in the range of measured periods. In order to expand these relations, an analysis of longer periods needs to be carried out either with *TESS* multi-sector data or using other photometric surveys such as SuperWASP (Shan et al. in prep.).

We also found 2567 flare events in 179 rotating stars. The flare frequency distribution follows a power law for energies greater than 10^{33} erg with an exponent $\alpha = 2.095^{+0.043}_{-0.059}$ for all stars. Separating the flare events in groups depending on spectral types, we find that later types show steeper distributions, with α growing with spectral type. The flare frequency of rotating stars seems to grow at shorter periods, peaking at ~ 0.5 d.

We left for future analysis the search of periodic signals using the FFI data from *TESS*, as well as the search for periods longer than 13 d. The analysis of flaring activity can also be improved in future work in some ways. A completeness function that depends on the energy could be defined by injecting artificial flares of varying energies in some light curves and running the detection algorithm. The ratio of flares injected to flares recovered at different energies could give an idea of the probability of detection as a function on energy. The flare frequency distribution shown in Fig. 15 could then be corrected using this completeness function, allowing us to use the discarded flares when fitting a power law.

This work was carried out in collaboration with the CARMENES team, in particular the photometry working package. The results shown here will be presented in *TESS* Science Conference II¹ in August 2021, apart from in several CARMENES internal meetings and videoconferences.

Acknowledgements

This work made use of multiple Python packages: `numpy`, `pandas`, `lightkurve`, `astropy`, `wotan` and `matplotlib` were the most used packages. In addition, several software pieces were used: GLS, `tpfplotter` and `exostriker`, written in Python. The links to these software can be found in footnotes in previous sections.

Lastly, the Virtual Observatory tools `Aladin`² and `TOPCAT`³ were very useful for visualizing (Fig. 3) and managing big catalogs.

This Master’s Thesis was possible thanks to the concession granted by IPARCOS (Instituto de Física de Partículas y del Cosmos).

¹<https://tsc.mit.edu/>

²<https://aladin.u-strasbg.fr/>

³<http://www.star.bris.ac.uk/~mbt/topcat/>

References

- Aller, A. et al. *Planetary nebulae seen with TESS: Discovery of new binary central star candidates from Cycle 1*. *A&A*, 635:A128, 2020.
- F.J. Alonso-Floriano, J.C. Morales, J.A. Caballero, et al. *CARMENES input catalogue of M dwarfs-I. Low-resolution spectroscopy with CAFOS*. *A&A*, 577:A128, 2015.
- M.L. Baart. *The Use of Auto-correlation for Pseudo-rank Determination in Noisy III-conditioned Linear Least-squares Problems*. *IMAJNA*, 2(2):241–247, 04 1982.
- D. Charbonneau et al. *Detection of Planetary Transits Across a Sun-like Star*. *ApJ*, 529(1):L45–L48, jan 2000.
- C. Cifuentes et al. *CARMENES input catalogue of M dwarfs - V. Luminosities, colours, and spectral energy distributions*. *A&A*, 642:A115, 2020.
- S. Deb and H.P. Singh. *Light curve analysis of variable stars using Fourier decomposition and principal component analysis*. *A&A*, 507(3):1729–1737, 2009.
- E. Díez Alonso et al. *CARMENES input catalogue of M dwarfs: IV. New rotation periods from photometric time series*. *A&A*, 621:1–17, 2019.
- G. Einaudi and M. Velli. *The distribution of flares, statistics of magnetohydrodynamic turbulence and coronal heating*. *Phys. Plasmas*, 6(11):4146–4153, 1999.
- C. Fabricius, X. Luri, F. Arenou, et al. *Gaia Early Data Release 3-Catalogue validation*. *A&A*, 649:A5, 2021.
- Georgoulis and Vlahos. *Coronal Heating by Nanoflares and the Variability of the Occurrence Frequency in Solar Flares*. *ApJ*, 469(2):L135–L138, oct 1996.
- S.H. Gilhool, C.H. Blake, R.C. Terrien, et al. *The Rotation of M Dwarfs Observed by the Apache Point Galactic Evolution Experiment*. *AJ*, 155(1):38, 2017.
- J.E. Gizis et al. *K2 Ultracool Dwarfs Survey. II. The White Light Flare Rate of Young Brown Dwarfs*. *ApJ*, 845(1):33, aug 2017.
- M.N. Günther et al. *Stellar Flares from the First TESS Data Release: Exploring a New Sample of M Dwarfs*. *AJ*, 159(2):60, 2020.
- J.D. Hartman, G.Á. Bakos, and R.W. others Noyes. *A photometric variability survey of field K and M dwarf stars with HATNet*. *AJ*, 141(5):166, 2011.
- C. Hedges et al. *Systematics-insensitive Periodogram for Finding Periods in TESS Observations of Long-period Rotators*. *Research Notes of the AAS*, 4(12):220, dec 2020.
- M. Hippke et al. *Wotan: Comprehensive Time-series Detrending in Python*. , 158(4):143, Oct 2019.
- P.J. Huber. *Robust Statistics*. Wiley Series in Probability and Statistics. Wiley, 1981. ISBN 9780471418054.
- H.S. Hudson. *Solar flares, microflares, nanoflares, and coronal heating*. *Sol. Phys.*, 133(2):357–369, 1991.
- Ilin, E., Schmidt, S.J., Davenport, J.R.A., and Strassmeier, K.G. *Flares in open clusters with K2 - I. M 45 (Pleiades), M 44 (Praesepe), and M 67*. *A&A*, 622:A133, 2019.
- J. Irwin, Z.K. Berta, and C.J. others Burke. *On the angular momentum evolution of fully convective stars: rotation periods for field M-dwarfs from the MEarth transit survey*. *ApJ*, 727(1):56, 2011.

- S.V. Jeffers, P. Schöfer, A. Lamert, et al. *CARMENES input catalogue of M dwarfs-III. Rotation and activity from high-resolution spectroscopic observations*. *A&A*, 614:A76, 2018.
- M. Kiraga. *ASAS photometry of ROSAT sources I. Periodic variable stars coincident with bright sources from ROSAT all sky survey*. *Acta Astron. Sin.*, 2012.
- C.H. Lacy et al. *UV Ceti stars-Statistical analysis of observational data*. *ApJSS*, 30:85–96, 1976.
- A.S. Mascareño, R. Rebolo, and J.I.G. Hernández. *Magnetic cycles and rotation periods of late-type stars from photometric time series*. *A&A*, 595:A12, 2016.
- M. Mayor and D. Queloz. *A Jupiter-mass companion to a solar-type star*. *Nature*, 378(6555):355–359, November 1995.
- E.R. Newton, J. Irwin, D. Charbonneau, Z.K. Berta-Thompson, J.A. Dittmann, and A.A. West. *The rotation and galactic kinematics of mid M dwarfs in the solar neighborhood*. *ApJ*, 821(2):93, 2016.
- A. Quirrenbach et al. *CARMENES: high-resolution spectra and precise radial velocities in the red and infrared*. (July 2018):32, 2018.
- D. Revilla. *Estudio de las curvas de luz de TESS de estrellas M de la muestra de CARMENES*. Master thesis, Universidad Complutense de Madrid, 2020.
- G.R. Ricker et al. *Transiting Exoplanet Survey Satellite*. *JATIS*, 1(1):014003, 2014.
- D.F. Ryan et al. *Effects of flare definitions on the statistics of derived flare distributions*. *A&A*, 592:A133, 2016.
- T. Shibayama et al. *Superflares on solar-type stars observed with Kepler. I. Statistical properties of superflares*. *ApJSS*, 209, 11 2013.
- E.L. Shkolnik, L. Hebb, M.C. Liu, I.N. Reid, and A.C. Cameron. *Thirty New Low-Mass Spectroscopic Binaries*. *ApJ*, 716(2):1522, 2010.
- K.G. Stassun et al. *The Revised TESS Input Catalog and Candidate Target List*. *AJ*, 158(4):138, 2019.
- O. Struve. *Proposal for a project of high-precision stellar radial velocity work*. *Observatory*, 72:199–200, October 1952.
- T. Trifonov. *The Exo-Striker: Transit and radial velocity interactive fitting tool for orbital analysis and N-body simulations*, June 2019.
- T. Trifonov et al. *A nearby transiting rocky exoplanet that is suitable for atmospheric investigation*. *Science*, 371(6533):1038–1041, 2021.
- C. Verbeeck et al. *Solar Flare Distributions: Lognormal Instead of Power Law?* *ApJ*, 884(1):50, oct 2019.
- A. A West, K.L. Weisenburger, J. Irwin, et al. *An Activity–Rotation Relationship and Kinematic Analysis of Nearby Mid-to-Late-Type M Dwarfs*. *ApJ*, 812(1):3, 2015.
- H. Yang et al. *The Flaring Activity of M Dwarfs in the Kepler Field*. *ApJ*, 849(1):36, 2017.
- M. Zechmeister and M. Kürster. *The generalised Lomb-Scargle periodogram a new formalism for the floating-mean and Keplerian periodograms*. *A&A*, 496(2):577–584, 2009.
- M. Zechmeister et al. *The CARMENES search for exoplanets around M dwarfs. Two temperate Earth-mass planet candidates around Teegarden’s Star*. *A&A*, 627:A49, July 2019.

Appendices

A. Periods

We show all the stars of the CARMENES sample for which we found a reliable rotation period. We also list the number of flares detected in stars with no bright companions.

Table A.1: Stars for which reliable rotational periods could be obtained with *TESS* SAP and PDCSAP photometry.

Karmn	Name	N_{sectors}	P_{rot}	eP_{rot}	N_{flares}
J00188+278	LP 292-066	1	5.9728	0.0134	1
J00245+300	G 130-068	1	1.0783	0.0002	3
J00324+672N	V547 Cas Aab	4	1.9032	0.0037	7
J00328-045	GR* 50 AB	2	0.4722	0.0002	5
J00341+253	V493 And	1	3.1208	0.0009	0
J00374+515	G 172-014	1	5.2946	0.0173	2
J00428+355	FF And	1	2.1669	0.0007	5
J00459+337	G 132-025 AB	1	0.6681	0.0003	0
J00548+275	G 069-032	1	1.7117	0.0024	2
J00580+393	1RXS J005802.4+391912	1	0.9134	0.0001	1
J01019+541	G 218-020	2	0.13894	$2 \cdot 10^{-5}$	9
J01033+623	V388 Cas	2	1.0238	0.0028	39
J01036+408	G 132-050	1	0.25393	$2 \cdot 10^{-5}$	7
J01114+154	LP 467-016 AB	1	0.4571	0.0001	0
J01125-169	YZ Cet	1	1.9366	0.0057	6
J01134-229	GJ 1033	2	0.4848	0.0002	10
J01221+221	G 034-023	1	0.5005	0.0001	0
J01339-176	LP 768-113	2	7.5526	0.0481	5
J01352-072	Barta 161 12	2	0.7037	0.0001	22
J01369-067	LP 648-020	2	1.061	0.0001	17
J01390-179	BL Cet + UV Cet	1	0.226959	$4 \cdot 10^{-6}$	0
J01437-060	BPS CS 22962-0011	2	0.8624	0.0001	0
J01510-061	NLTT 6192	1	0.4683	0.0001	4
J01531-210	BD-21 332 AB	2	2.8543	0.0005	0
J02019+735	LP 030-055	3	1.0524	0.0595	0
J02071+642	G 244-049	3	1.1766	0.001	24
J02088+494	G 173-039	1	0.748	0.0002	10
J02129+000	G 159-046	2	4.7141	0.1187	7
J02142-039	LP 649-072	2	2.3345	0.0053	3
J02155+339	G 074-011	1	6.0302	0.0053	4
J02171+354	LP 245-010	1	0.27582	$2 \cdot 10^{-5}$	3
J02190+238	LTT 10787	1	0.9708	0.0001	3
J02207+029	LTT 17354	2	0.5025	0.0001	6
J02274+031	2M J02272756+0310548	2	1.2467	0.0003	11
J02336+249	GJ 102	1	3.0005	0.0054	6
J02353+235	2E 591	1	0.5463	$2 \cdot 10^{-5}$	12
J02367+226	G 036-026	1	0.37	0.0001	5
J02392+074	G 076-019	2	6.1743	0.0066	3
J02412-045	G 075-035	2	0.402	0.0001	8
J02518+294	LP 298-042	1	0.8947	0.0002	0
J02560-006	LP 591-156	2	1.0628	0.0002	2

Table A.1: Stars for which reliable rotational periods could be obtained with *TESS* SAP and PDCSAP photometry.

Karmn	Name	N_{sectors}	P_{rot}	eP_{rot}	N_{flares}
J02562+239	LSPM J0256+2359	1	0.5739	0.0001	0
J03018-165S	LP 771-096	2	1.3957	0.0021	0
J03033-080	StM 20	2	0.6263	0.0001	7
J03077+249	LP 355-027	1	4.2279	0.0036	1
J03112+011	1RXS J031114.2+010655	2	0.110585	$3 \cdot 10^{-6}$	1
J03147+114	RX J0314.7+1127	2	4.3532	0.0442	8
J03172+453	G 078-028 AB	1	3.3613	0.0063	0
J03217-066	G 77-046	2	5.5281	0.0144	1
J03236+056	1RXS J032338.7+054117	2	0.7695	0.0002	11
J03272+273	CK Ari	1	9.7813	0.0049	5
J03288+264	LP 356-106	1	3.1723	0.007	3
J03325+287	RX J0332.6+2843	1	0.41406	$4 \cdot 10^{-5}$	0
J03361+313	[GBM90] Per 49	1	0.8563	0.0001	8
J03366+034	[R78b] 233	1	0.3277	$3 \cdot 10^{-5}$	8
J03416+552	TYC 3720-426-1	1	4.6414	0.0013	15
J03473-019	G 080-021	2	3.8793	0.0019	43
J03565+319	HAT 214-02089	1	5.8362	0.0066	4
J04056+057	[R78b] 256 AB	2	1.4603	0.0004	0
J04059+712E	LP 031-301	3	7.4084	0.1115	0
J04112+495	Ross 27	1	0.9387	0.0017	0
J04122+647	G 247-015	1	1.603	0.0009	8
J04173+088	LTT 11392	2	0.36972	$1 \cdot 10^{-5}$	32
J04177+410	LSPM J0417+4103	1	1.085	0.0006	11
J04198+425	LSR J0419+4233	1	0.9868	0.0005	0
J04234+809	1RXS J042323.2+805511	3	0.39	0.0002	44
J04238+092	LP 535-073	1	5.1994	0.0053	6
J04238+149	IN Tau	2	0.9184	0.0002	13
J04247-067	2M J04244260-0647313	2	5.4149	0.0068	0
J04276+595	G 175-032	1	7.1611	0.0176	0
J04308-088	Koenigstuhl 2A	2	5.494	0.0584	3
J04312+422	2M J04311499+4217111	1	3.9784	0.0037	4
J04350+086	StKM 1-495	1	1.1156	0.0009	6
J04369-162	2MASS J04365738-1613065	2	0.60974	$4 \cdot 10^{-5}$	0
J04393+335	RX J0439.4+3332B	1	0.8951	0.0002	0
J04403-055	LP 655-048	2	0.4999	0.0002	18
J04414+132	TYC 694-1183-1	2	4.9041	0.0159	0
J04488+100	1RXS J044847.6+100302	2	4.256	0.0913	0
J04494+484	G 081-034	1	1.6599	0.0003	0
J04499+711	NLTT 13933	3	0.1738	$3 \cdot 10^{-5}$	0
J04524-168	NLTT 14116	2	1.3687	0.0003	47
J04595+017	V1005 Ori	2	4.4054	0.0025	24
J05019+011	1RXS J050156.7+010845	2	2.0794	0.0003	25
J05019+099	LP 476-207 AB	2	6.3395	0.0031	0
J05042+110	G 097-015	2	0.8412	0.0001	7
J05062+046	RX J0506.2+0439	1	0.8871	0.0001	12
J05084-210	2M J05082729-2101444	2	0.28046	$1 \cdot 10^{-5}$	17
J05091+154	Ross 388	1	2.541	0.0016	10
J05187+464	2M J05184455+4629597	1	0.29333	$3 \cdot 10^{-5}$	11

Table A.1: Stars for which reliable rotational periods could be obtained with *TESS* SAP and PDCSAP photometry.

Karmn	Name	N_{sectors}	P_{rot}	eP_{rot}	N_{flares}
J05243-160	1RXS J052419.1-160117	1	0.39636	$2 \cdot 10^{-5}$	0
J05322+098	V998 Ori	2	7.5075	0.0067	0
J05333+448	GJ 1081	1	0.5228	0.0001	0
J05337+019	V371 Ori	2	0.6048	0.0001	52
J05339-023	RX J0534.0-0221	2	7.2573	0.0045	21
J05402+126	V1402 Ori AB	1	1.5777	0.0002	0
J05425+154	1RXS J054232.1+152459	1	0.3678	0.0002	2
J05547+109	RX J0554.7+1055	2	0.56551	$3 \cdot 10^{-5}$	0
J05566-103	1RXS J055641.0-101837	2	1.6494	0.0004	13
J05599+585	G 192-012	1	0.948	0.0002	7
J06000+027	G 099-049	2	1.8143	0.0017	24
J06054+608	LP 086-173	2	0.31	0.0001	0
J06075+472	LSPM J0607+4712	1	0.8618	0.0001	15
J06171+751	TYC 4525-194-1	3	0.5383	0.0001	0
J06212+442	G 101-035	1	5.8483	0.0024	0
J06238+456	LP 160-022	1	2.5305	0.0018	4
J06293-028	V577 Mon AB	1	1.5852	0.0004	0
J06310+500	StKM 1-598	1	4.9656	0.0041	16
J06318+414	LP 205-044	1	0.2994	$1 \cdot 10^{-5}$	8
J06354-040	2M J06352986-0403185	1	0.7138	0.0001	0
J06467+159	TYC 1330-879-1	1	2.4741	0.0013	6
J06474+054	G 108-027	1	0.732	0.0015	0
J06509-091	LP 661-002	2	0.11515	$4 \cdot 10^{-5}$	0
J07051-101	2MASS J07051194-1007528	2	0.5408	0.0003	7
J07172-050	2M J07171706-0501031	2	0.4124	0.0001	12
J07212+005	TYC 178-2187-1	1	9.057	0.014	0
J07295+359	1RXS J072931.4+355607	1	1.9788	0.0003	0
J07310+460	1RXS J073101.9+460030	1	1.964	0.0009	9
J07446+035	YZ CMi	1	2.7789	0.0004	36
J07467+574	G 193-065	1	0.8199	0.0001	10
J07472+503	2M J07471385+5020386	1	1.3159	0.0003	8
J08317+057	2M J08314794+0545186	1	0.595	$4 \cdot 10^{-5}$	15
J08536-034	LP 666-009	1	0.4641	0.0002	3
J08589+084	NLTT 20670	1	0.8	0.0001	0
J08595+537	G 194-047	1	0.13618	$1 \cdot 10^{-5}$	0
J09096+067	2E 2104	1	4.0396	0.0018	8
J09161+018	RX J0916.1+0153	1	1.4326	0.0002	18
J09168+248	2M J09165078+2448559	1	0.2245	$1 \cdot 10^{-5}$	6
J09177+462	RX J0917.7+4612	1	1.0161	0.0001	0
J09193+620	LP 091-014 AB	2	2.9433	0.0139	0
J09248+306	LSPM J0924+3041	1	0.37305	$1 \cdot 10^{-5}$	20
J09256+634	G 235-025	2	1.6151	0.0009	0
J09275+506	G 195-027	1	10.5175	0.0357	0
J09302+265	RX J0930.2+2630 1	1	10.1276	0.0222	6
J09430+237	LP 370-035	1	10.1277	0.1041	0
J09449-123	G 161-071	1	0.44161	$2 \cdot 10^{-5}$	17
J09539+209	NLTT 22870	1	0.6131	0.0002	3
J10043+503	G 196-003A	1	1.3147	0.0001	22

Table A.1: Stars for which reliable rotational periods could be obtained with *TESS* SAP and PDCSAP photometry.

Karmn	Name	N_{sectors}	P_{rot}	eP_{rot}	N_{flares}
J10122-037	AN Sex	1	6.4848	0.0088	1
J10133+467	LP 167-017	1	2.0256	0.0091	2
J10367+153	RX J1036.7+1521	1	1.7924	0.0006	0
J10368+509	LP 127-502	1	2.532	0.0018	0
J10384+485	LP 167-071	1	3.1798	0.0009	13
J10506+517	LP 128-032	1	6.511	0.0041	6
J10520+005	G 045-011 ABC	1	1.3027	0.0004	0
J11031+366	LP 263-064	1	2.0516	0.0004	8
J11118+335	CW UMa	1	7.7413	0.0035	16
J11159+553	StKM 1-932	1	1.0017	0.0001	11
J11201-104	LP 733-099	1	5.6434	0.0054	4
J11240+381	1RXS J112405.0+380809	1	0.47467	$3 \cdot 10^{-5}$	1
J11433+253	LTT 13220	1	1.3267	0.0003	9
J11519+075	RX J1151.9+0731	1	2.2781	0.0005	0
J12121+488	G 122-074	1	1.5964	0.0015	0
J12156+526	StKM 2-809	1	0.7255	0.0001	17
J12169+311	Sand 39	1	2.1333	0.0005	0
J12269+270	CX Com	1	2.7221	0.002	5
J12294+229	LP 377-100	1	5.9065	0.0043	1
J12332+090	FL Vir AB	1	0.20724	$1 \cdot 10^{-5}$	0
J12417+567	RX J1241.7+5645	2	2.0391	0.0008	15
J12470+466	Ross 991	2	0.29763	$4 \cdot 10^{-5}$	0
J12485+495	RX J1248.5+4933	2	0.5885	0.0001	21
J13005+056	FN Vir	1	0.6008	0.0001	7
J13007+123	DT Vir AB	1	2.905	0.0004	11
J13095+289	GJ 1167A	1	0.215232	$4 \cdot 10^{-6}$	5
J13317+292	DG CVn AB	1	0.26829	$2 \cdot 10^{-5}$	0
J13326+309	LP 323-169	1	0.30831	$2 \cdot 10^{-5}$	0
J13376+481	BD+48 2138C	3	0.5576	0.0003	5
J13417+582	StM 187	2	1.7008	0.0018	0
J13488+041	Wolf 1494	1	0.353	$2 \cdot 10^{-5}$	2
J13518+127	RX J1351.8+1247	1	4.889	0.0051	9
J13536+776	RX J1353.6+7737	5	1.2312	0.0012	39
J13591-198	LP 799-007	1	3.3248	0.0029	7
J14023+136	MCC 150	1	8.9489	0.0139	0
J14173+454	RX J1417.3+4525	2	0.3612	0.0045	14
J14200+390	IZ Boo	2	0.3691	0.0001	26
J14306+597	LP 098-079	3	0.4128	0.0004	1
J14312+754	2M J14311348+7526423	5	0.6317	0.0003	14
J14511+311	LP 326-038	2	2.3414	0.0026	12
J14549+411	LP 222-015	3	6.0141	0.0256	8
J14578+566	GJ 1187	4	0.8281	0.001	4
J15079+762	HD 135363 B	6	0.7571	0.0017	51
J15126+457	G 179-020	3	1.6835	0.0033	25
J15166+391	LP 222-065	2	0.2907	0.0001	5
J15218+209	OT Ser	1	3.3525	0.001	11
J15238+561	StKM 1-1240	4	0.8771	0.1774	45
J15238+584	G 224-065	5	1.1199	0.0013	54

Table A.1: Stars for which reliable rotational periods could be obtained with *TESS* SAP and PDCSAP photometry.

Karmn	Name	N_{sectors}	P_{rot}	eP_{rot}	N_{flares}
J15290+467	RX J1529.0+4646 AB	3	0.6704	0.0265	0
J15319+288	G 167-047	1	3.1159	0.0022	0
J15368+375	BK CrB	1	4.4889	0.0027	0
J15474+451	LP 177-102 AB	2	3.5214	0.0059	0
J15476+226	LSPM J1547+2241	1	2.7879	0.0012	1
J15496+348	LP 274-008	1	1.4963	0.001	0
J15499+796	LP 022-420	7	0.18779	$3 \cdot 10^{-5}$	32
J15555+352	G 180-011 AB	1	3.6281	0.0065	13
J15557+686	RX J1555.7+6840	12	3.9403	0.0141	101
J15569+376	RX J1556.9+3738	1	0.6145	0.0001	5
J15581+494	V1022 Her	2	0.8153	0.0004	18
J15597+440	RX J1559.7+4403	1	0.37044	$2 \cdot 10^{-5}$	6
J16139+337	sig CrB Cab	2	0.3922	0.0002	0
J16313+408	G 180-060	2	0.5118	0.0004	19
J16343+571	CM Dra Aab	7	1.268	0.0048	0
J16354+350	LP 275-068	2	0.9167	0.0002	0
J16403+676	LP 069-457	12	0.3783	0.0004	85
J16509+224	G 169-029	1	0.8976	0.0001	7
J16591+209	RX J1659.1+2058	1	4.0748	0.0024	0
J17038+321	LP 331-057	1	2.0531	0.0015	0
J17338+169	1RXS J173353.5+165515	1	0.265951	$5 \cdot 10^{-6}$	12
J17572+707	LP 044-162	12	0.1623	0.0001	4
J18022+642	LP 071-082	11	0.2803	0.0001	140
J18131+260	LP 390-016	1	2.2814	0.0004	15
J18189+661	LP 071-165	10	0.5225	0.0003	45
J18358+800	LP 025-002	9	4.0793	0.0164	48
J18394+690	RX J1839.4+6903	12	10.2912	0.3265	45
J18416+397	G 205-035	2	0.2959	0.0002	11
J18427+139	V816 Her	1	8.0216	0.0143	8
J18453+188	G 184-024	1	1.015	0.0002	6
J19044+590	LSPM J1907+5905	12	2.01	0.0133	12
J19146+193N	Ross 733	1	0.9132	0.0002	14
J19260+244	G 185-023	1	2.6521	0.0017	1
J19312+361	G 125-015	1	1.6273	0.0005	0
J19354+377	RX J1935.4+3746	1	8.3906	0.0103	5
J19511+464	G 208-042	2	0.593	0.0003	32
J19512+622	G 260-035	9	1.2112	0.0064	1
J20050+544	V1513 Cyg	2	0.4967	0.0003	17
J20198+229	LP 395-008	1	1.1282	0.0001	0
J20301+798	GSC 04593-01344	7	2.4264	0.005	91
J20435+240	Wolf 1360	2	0.799	0.0001	41
J20451-313	AU Mic	2	4.8888	0.0034	49
J21380+277	BD+27 4120 AabC	1	0.6495	0.0005	0
J22012+283	V374 Peg	1	0.44597	$1 \cdot 10^{-5}$	19
J22117-207	WT 2221 A	2	1.5228	0.0003	19
J22231-176	LP 820-012	1	4.5745	0.0084	6
J22387-206S	FK Aqr	1	4.03	0.0101	0
J22468+443	EV Lac	1	4.3491	0.0043	20

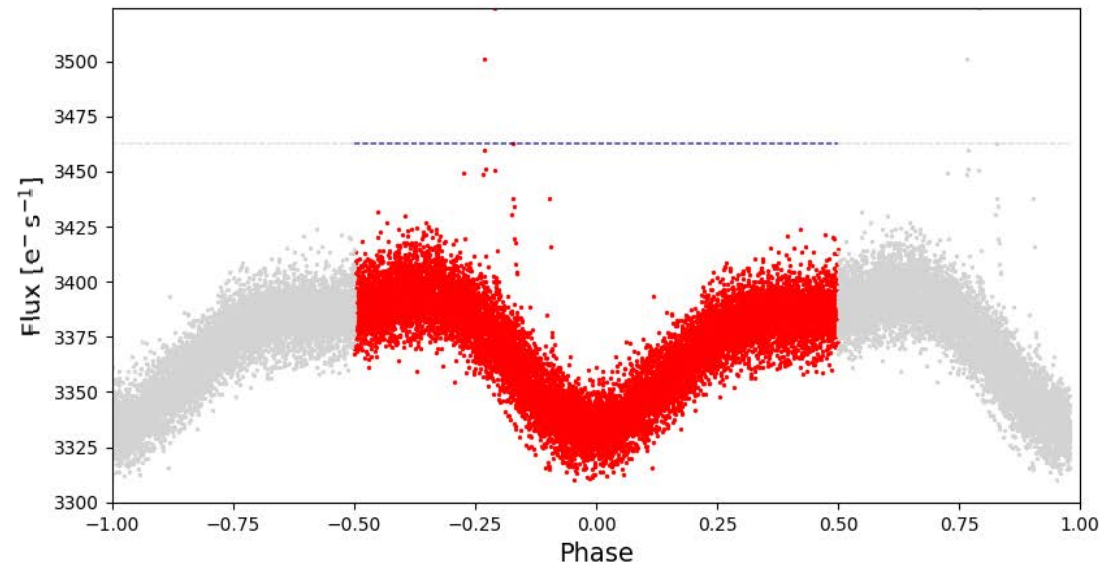
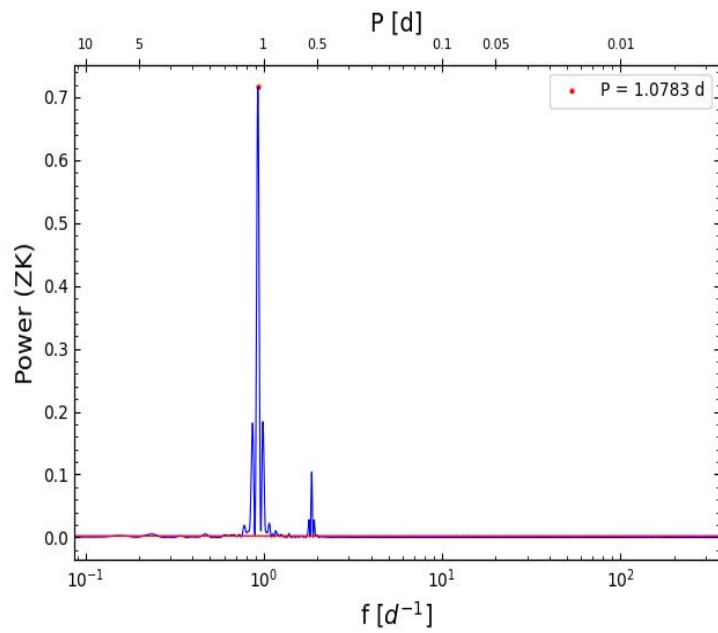
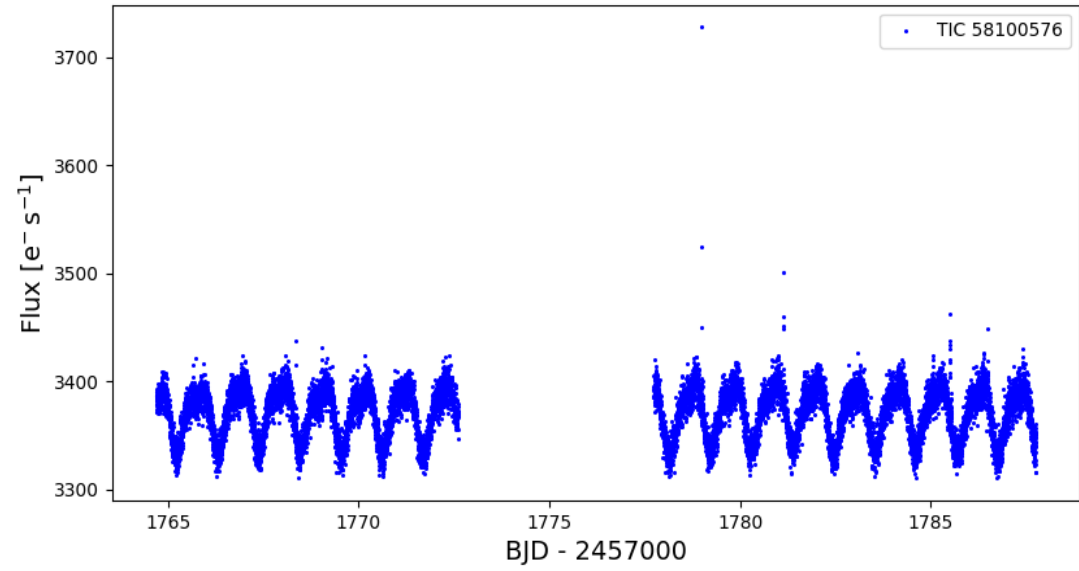
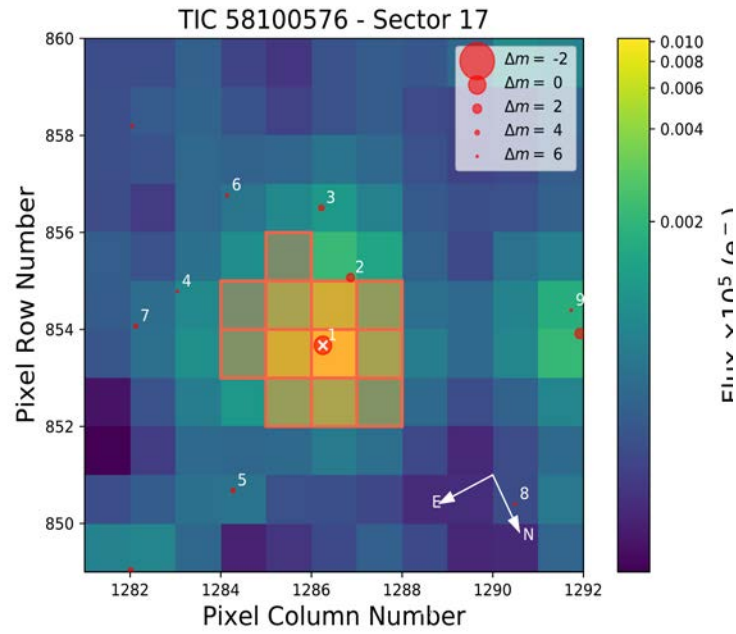
Table A.1: Stars for which reliable rotational periods could be obtained with *TESS* SAP and PDCSAP photometry.

Karmn	Name	N_{sectors}	P_{rot}	eP_{rot}	N_{flares}
J22509+499	2M J22505505+4959132	2	0.6847	0.0001	14
J23028+436	LSPM J2302+4338	1	0.34755	$2 \cdot 10^{-5}$	3
J23051+452	LSPM J2305+4517	2	1.3418	0.0578	12
J23083-154	HK Aqr	2	0.43088	$1 \cdot 10^{-5}$	24
J23228+787	NLTT 56725	4	1.0444	0.0015	8
J23293+414N	G 190-028	2	1.4208	0.0029	22
J23302-203	GJ 1284	2	7.3929	0.0206	0
J23439+647	Ross 676 AB	3	1.7291	0.0075	0
J23455-161	LP 823-004 AB	2	0.3996	0.0002	0
J23548+385	RX J2354.8+3831	1	4.798	0.0015	17
J23578+386	LP 291-034	1	2.2572	0.0007	0

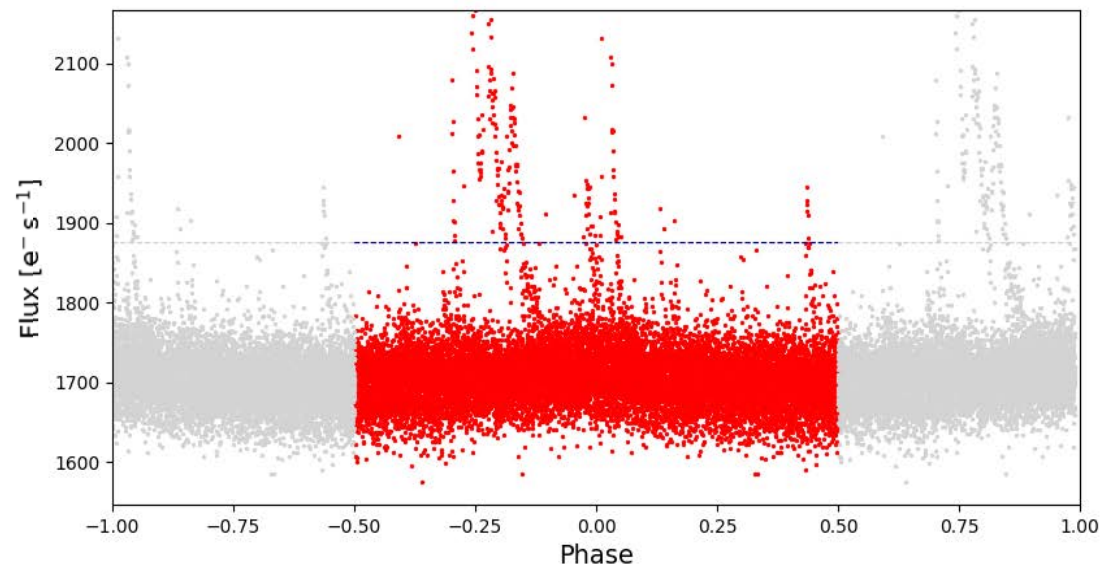
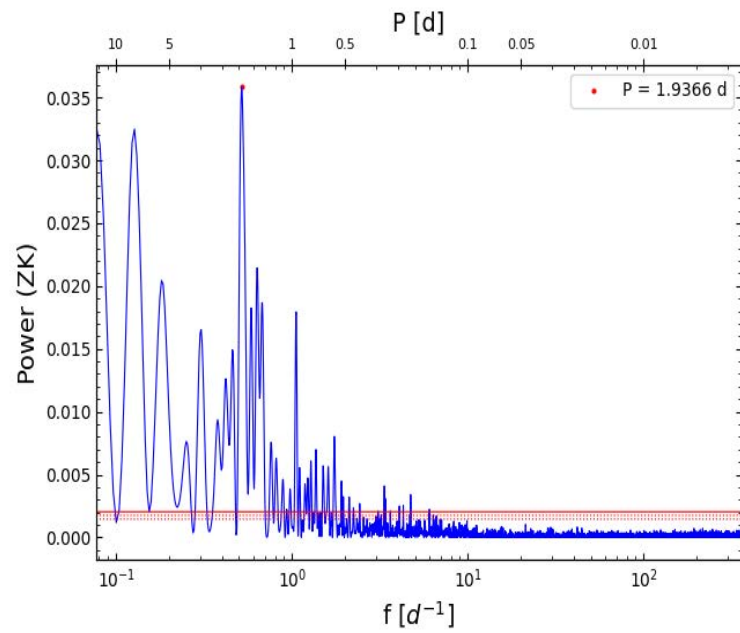
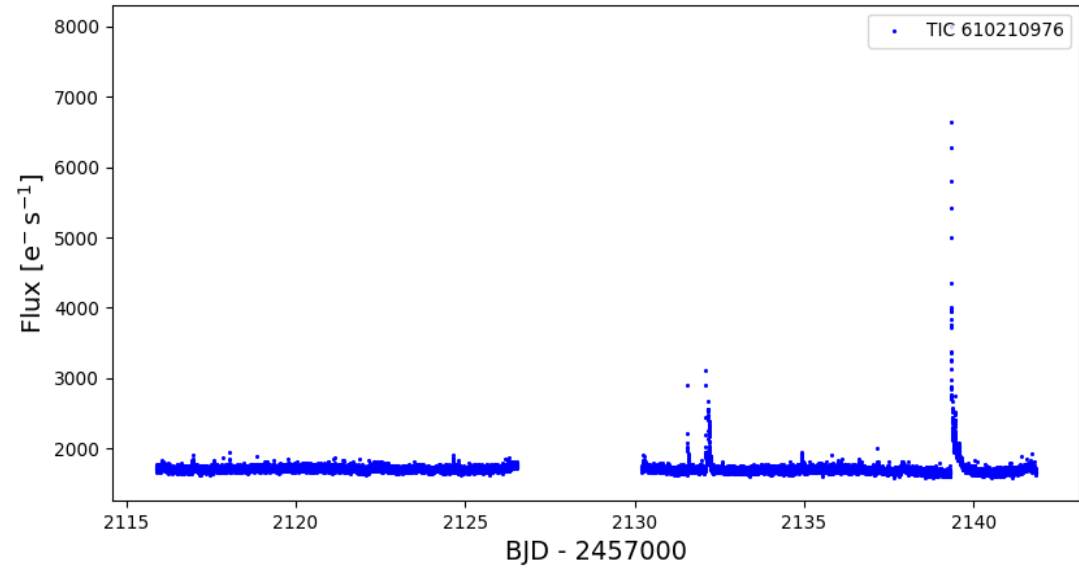
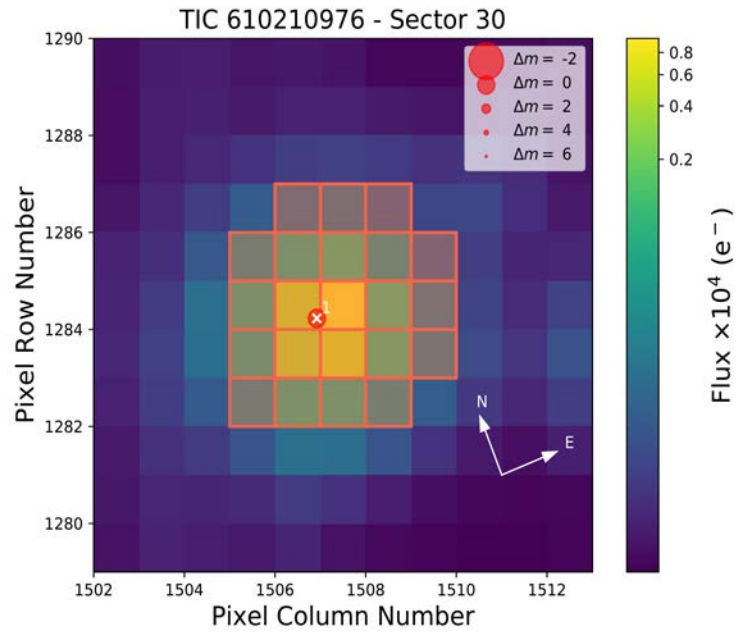
B. Summary sheets

In the following pages we show some of the summary sheets that we created for quick checking rotation periods obtained.

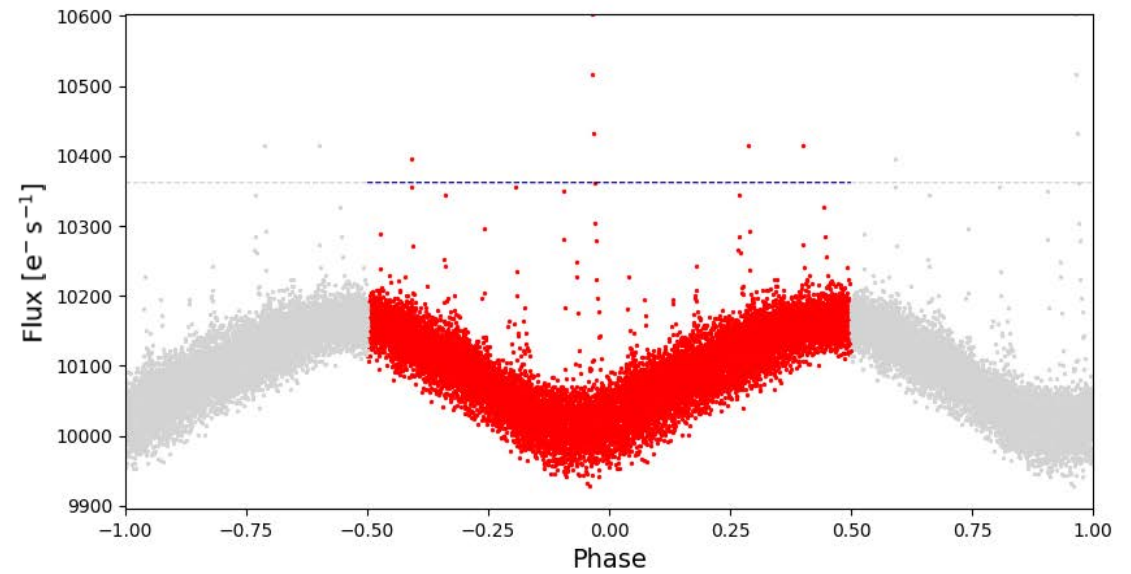
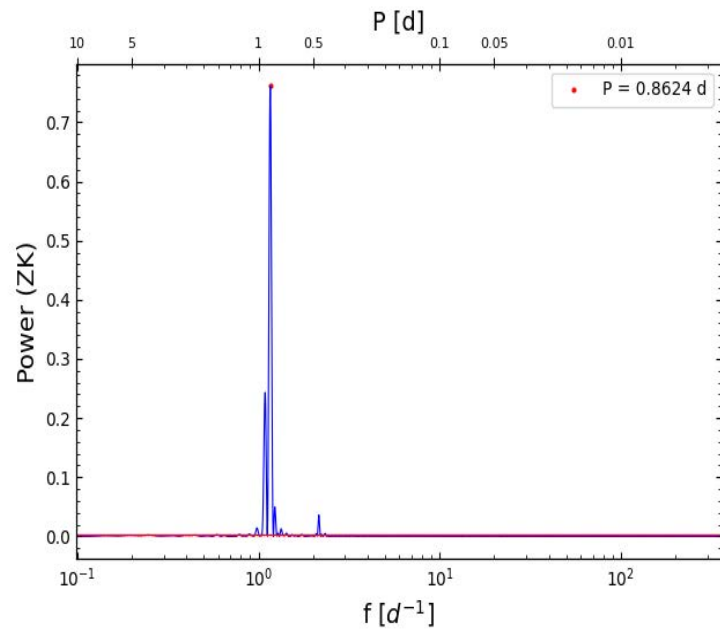
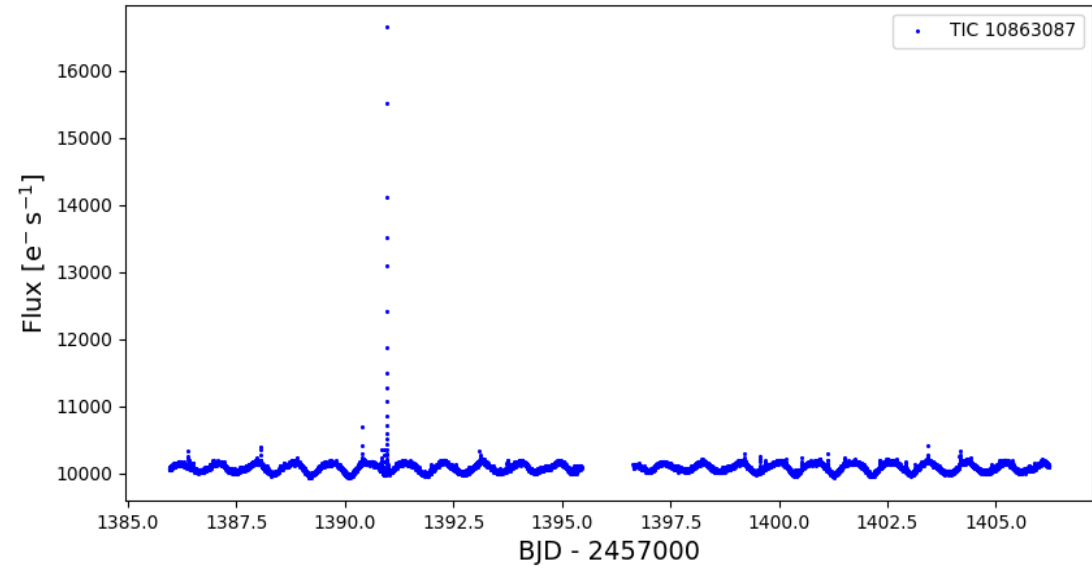
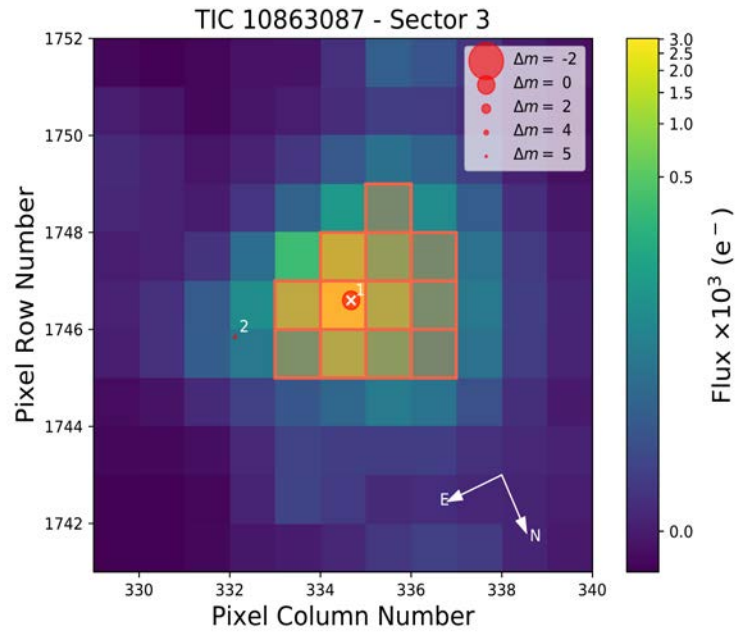
Karmn J00245+300 = G 130-068



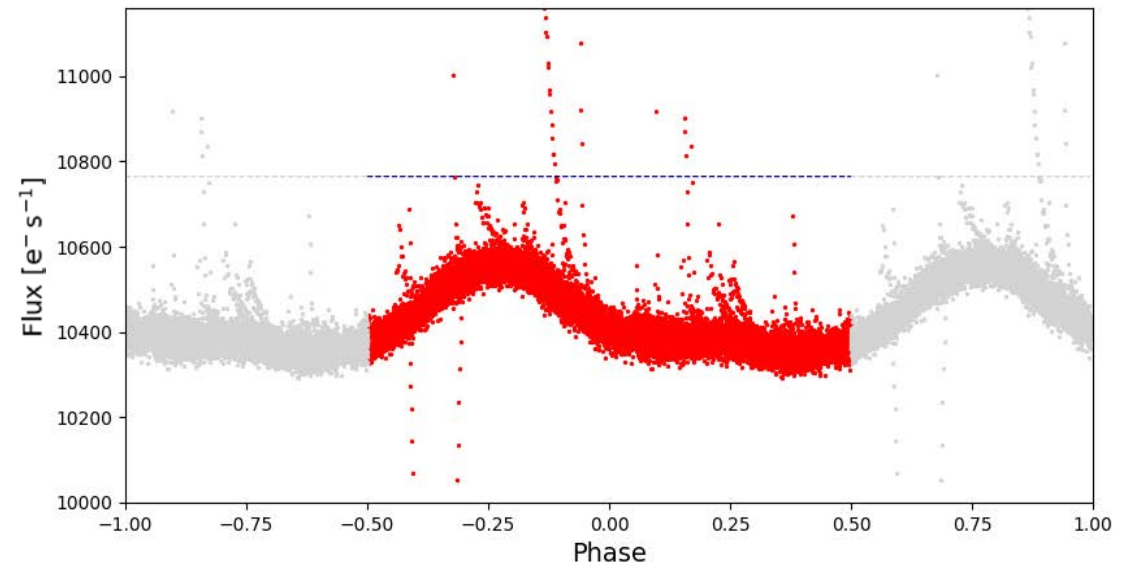
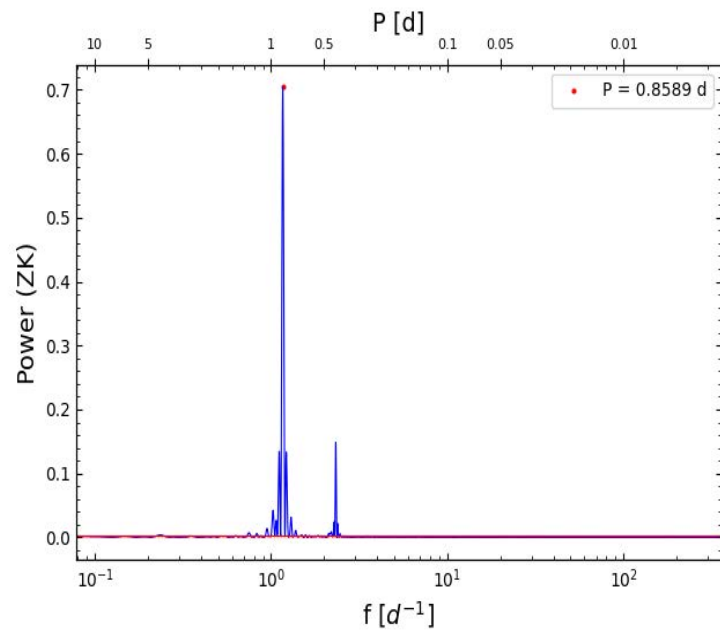
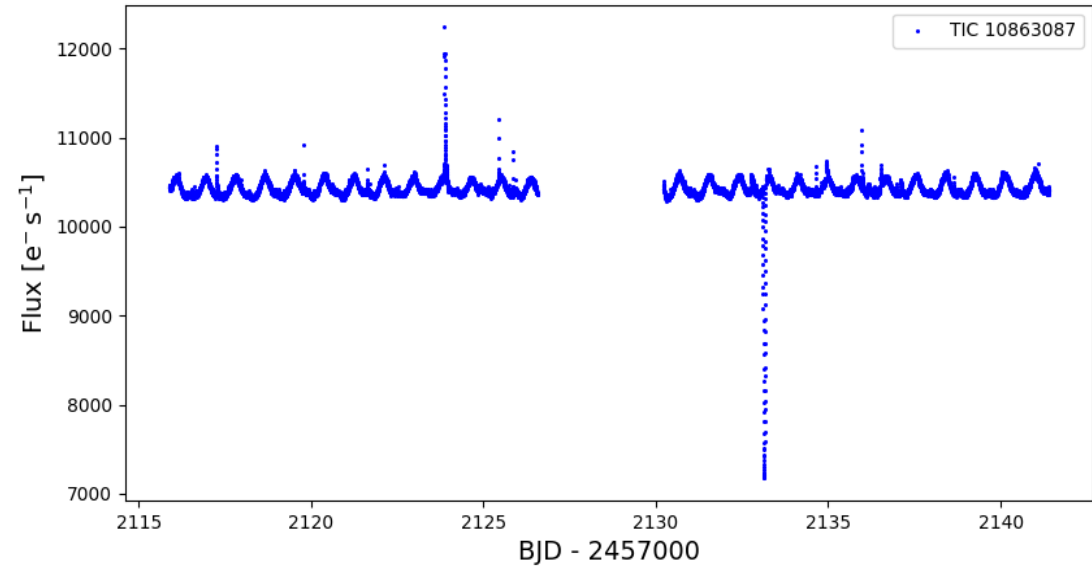
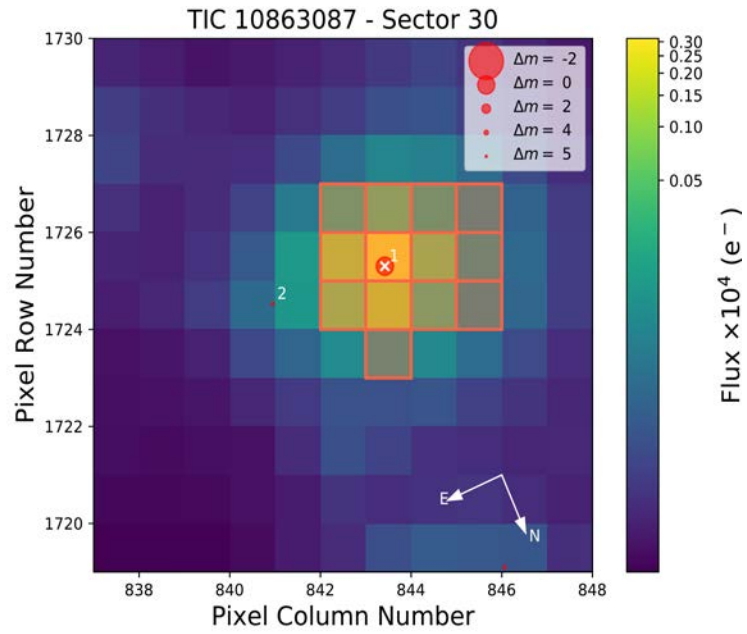
Karmn J01125-169 = YZ Cet



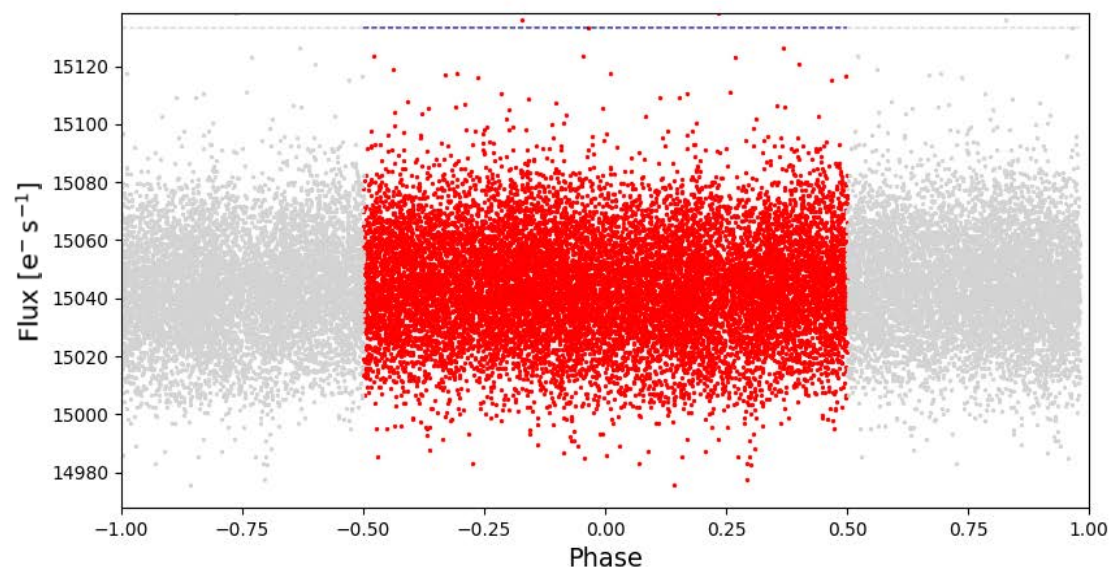
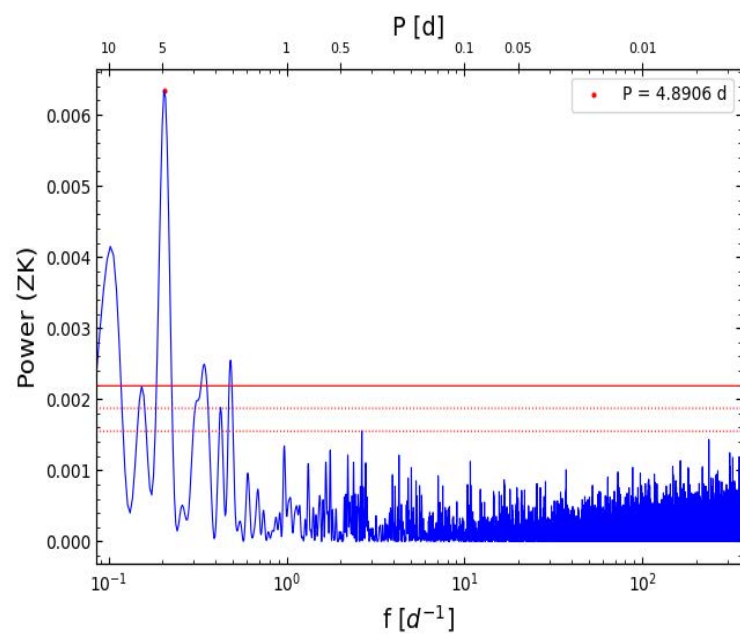
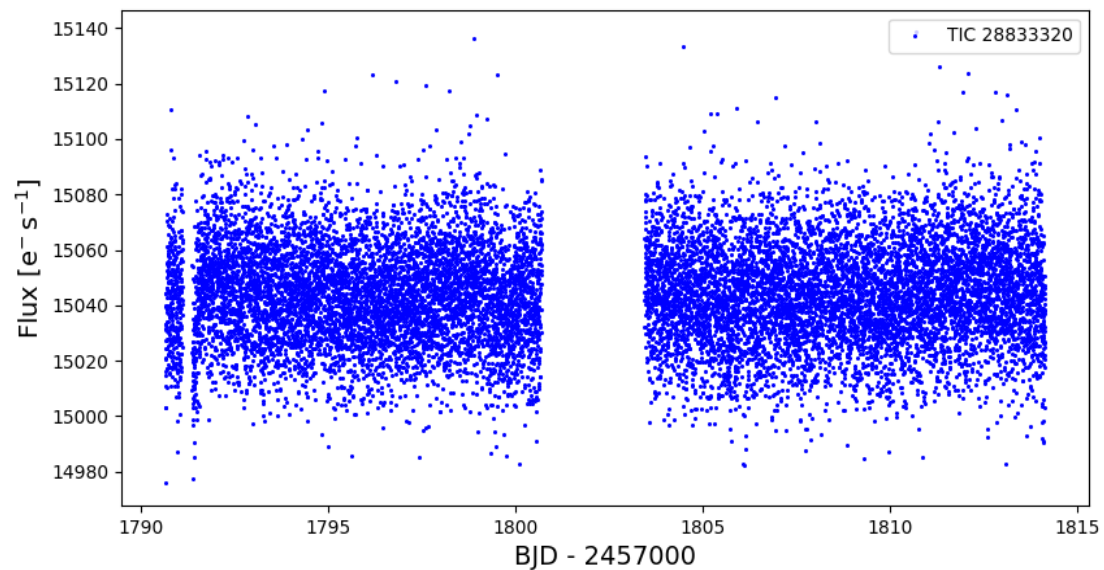
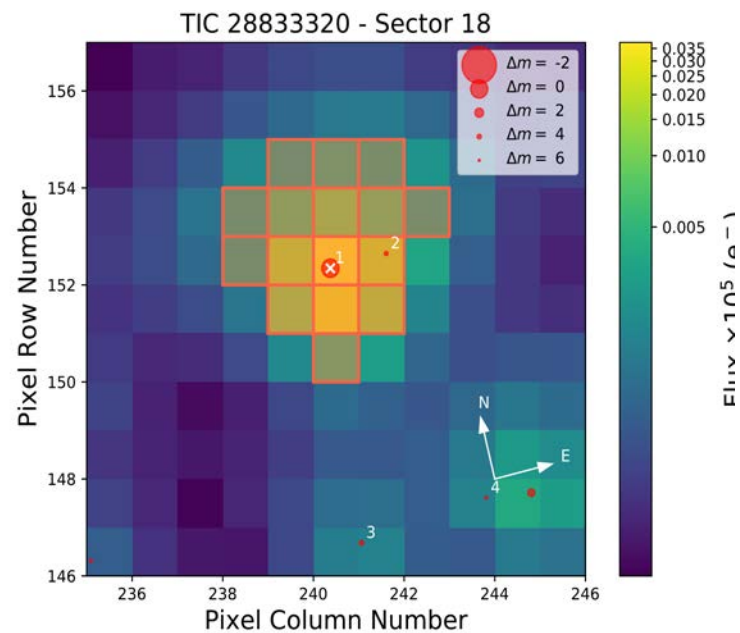
Karmn J01437-060 = BPS CS 22962-0011



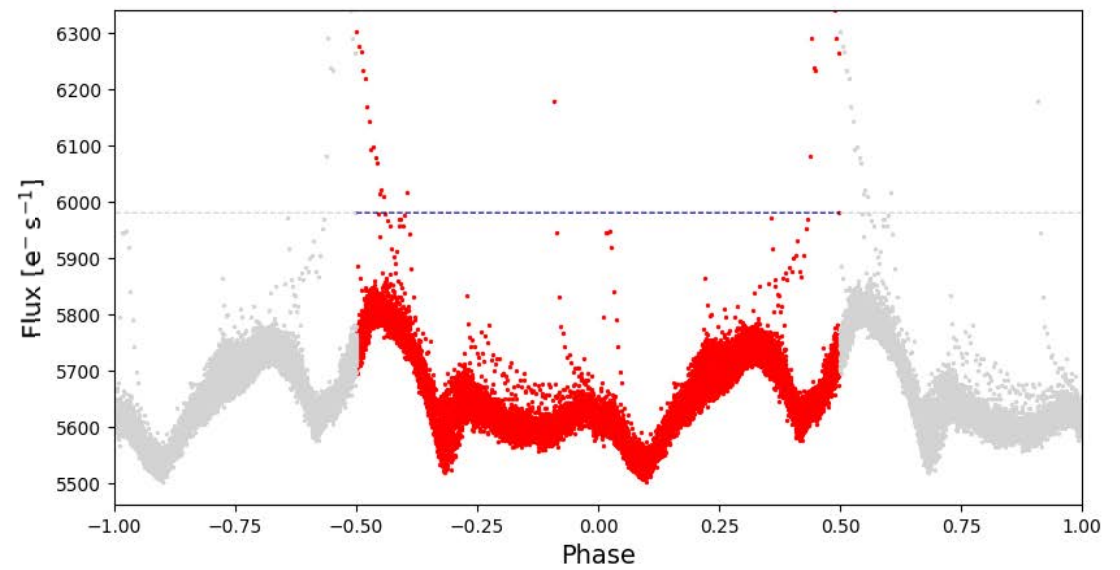
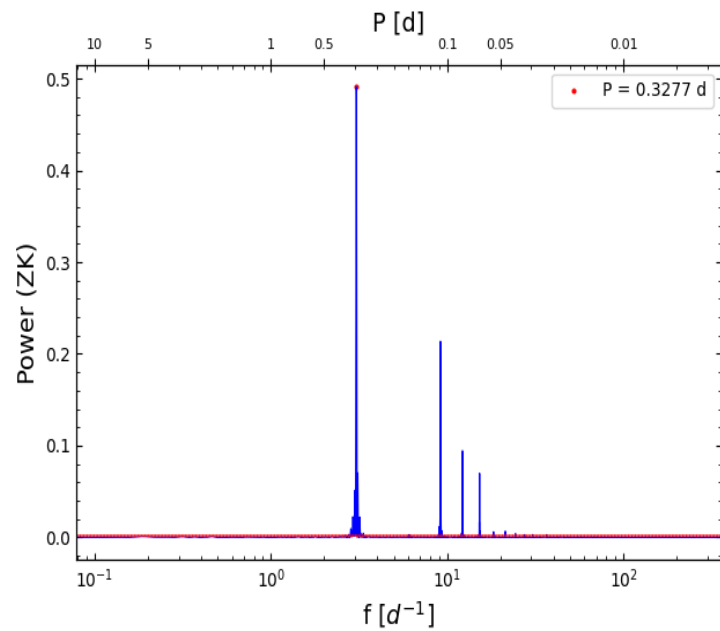
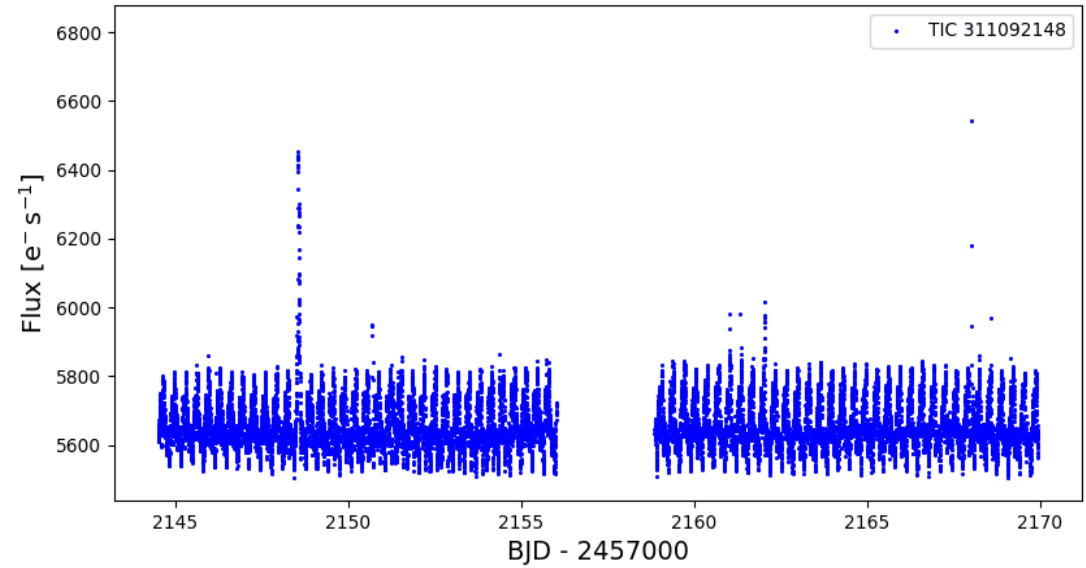
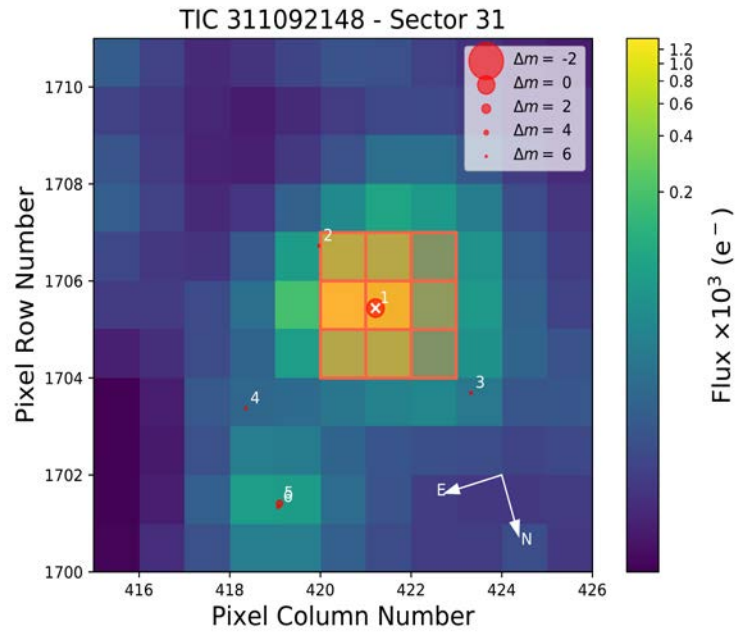
Karmn J01437-060 = BPS CS 22962-0011



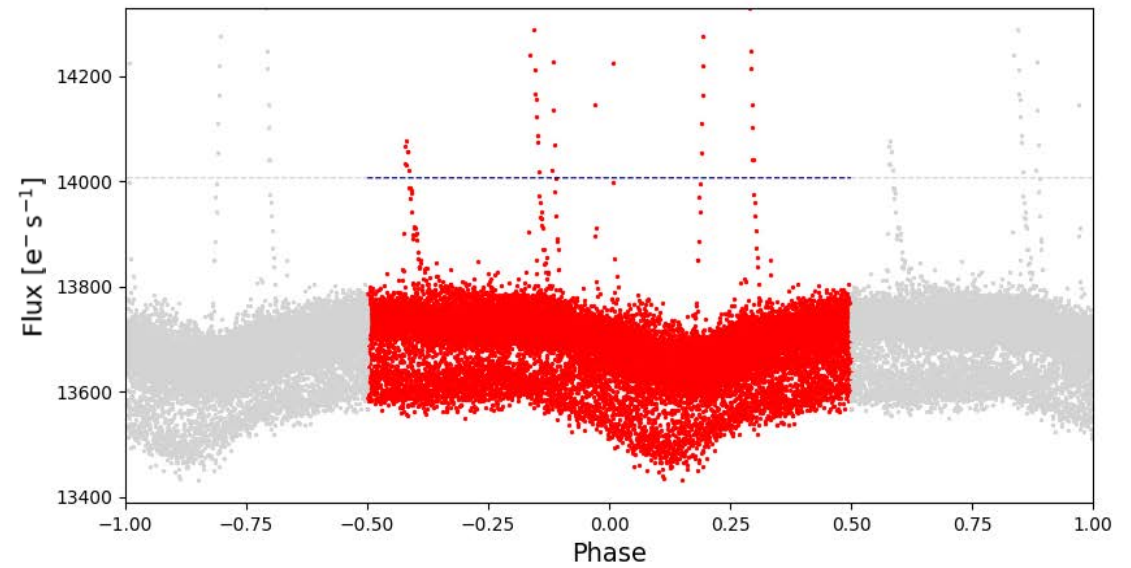
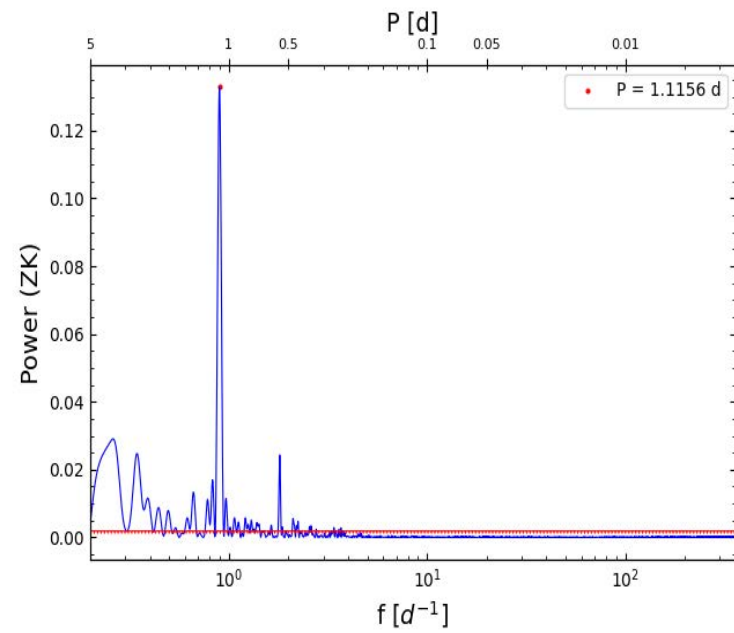
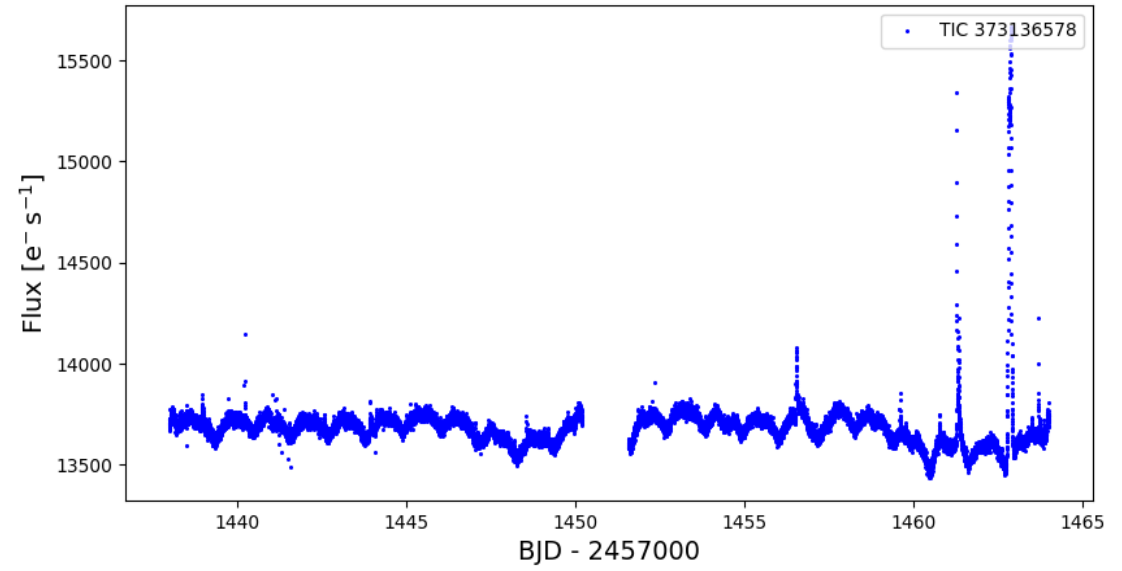
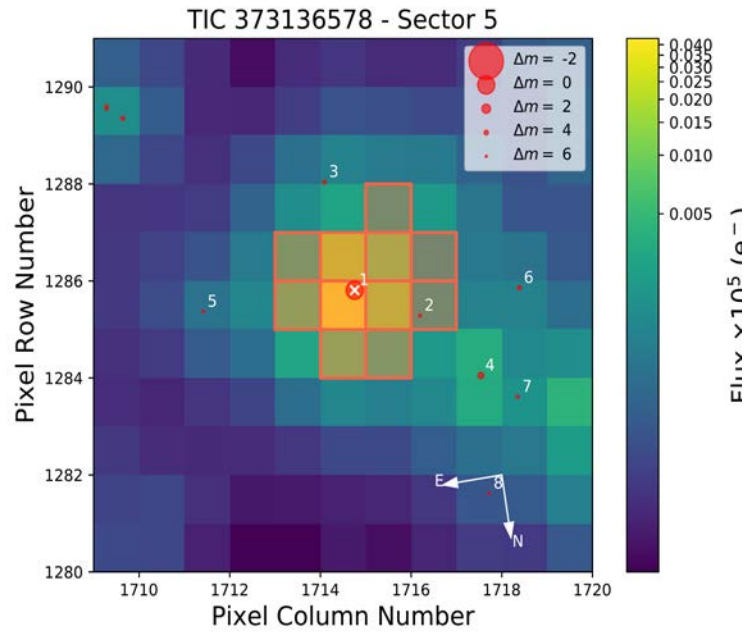
Karmn J03177+252 = LP 355-051



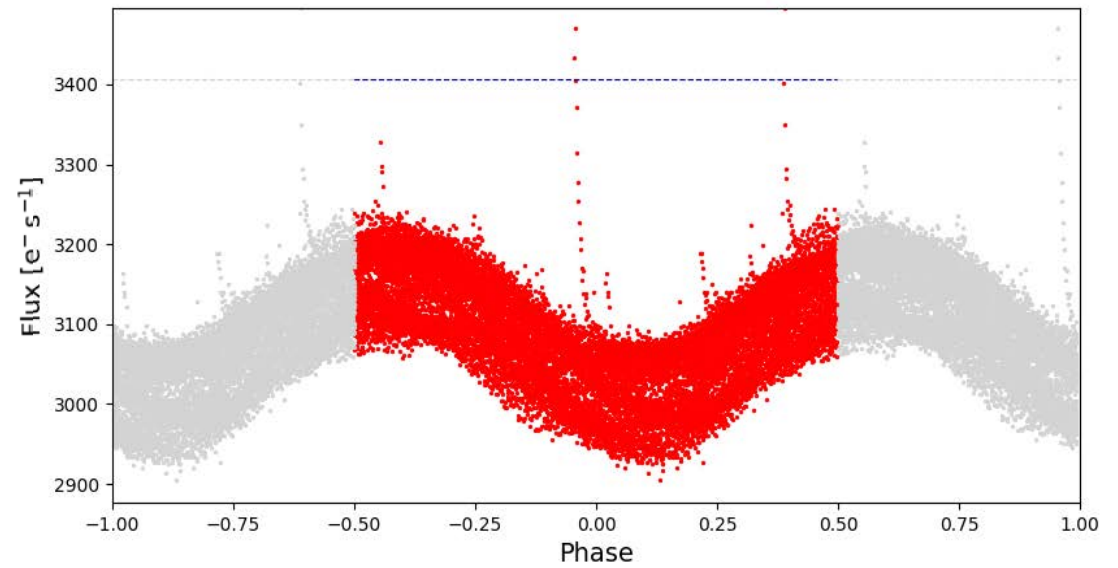
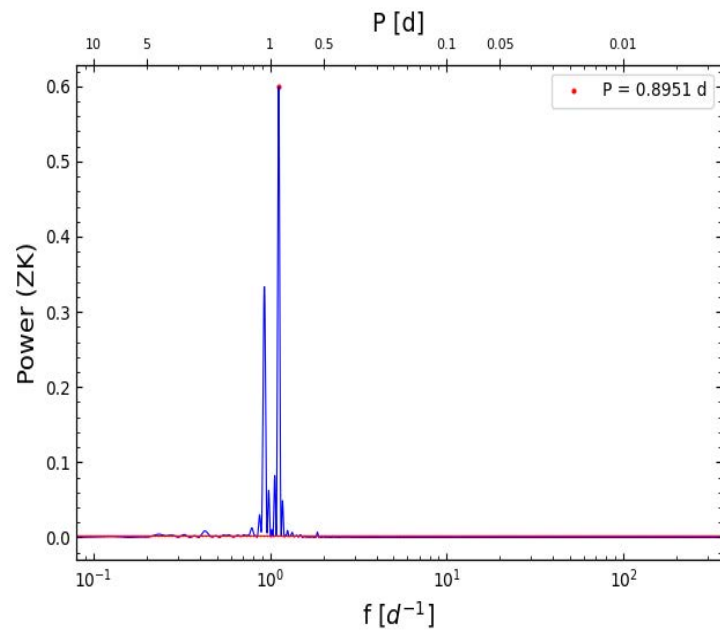
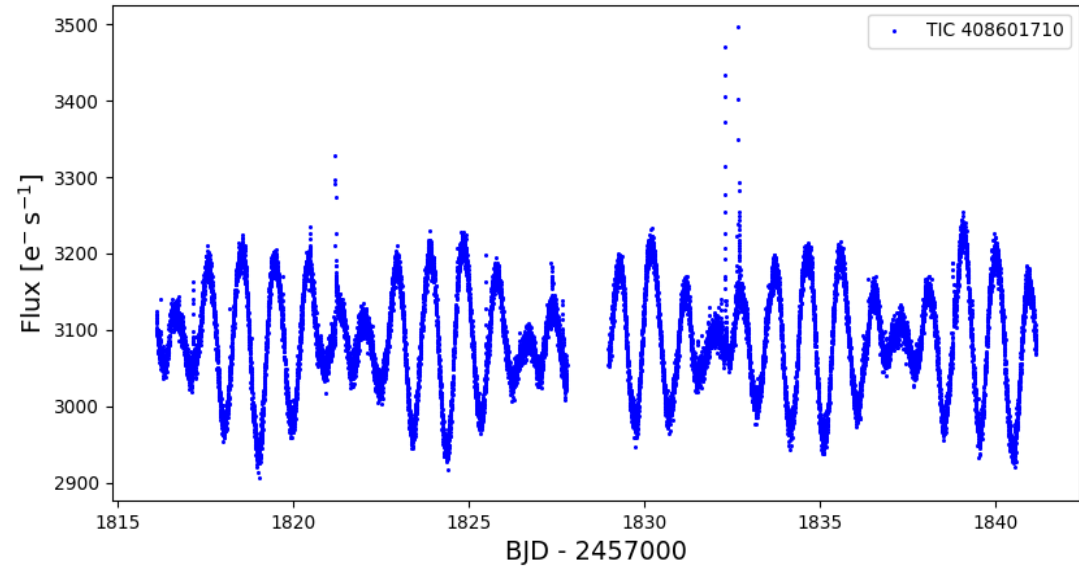
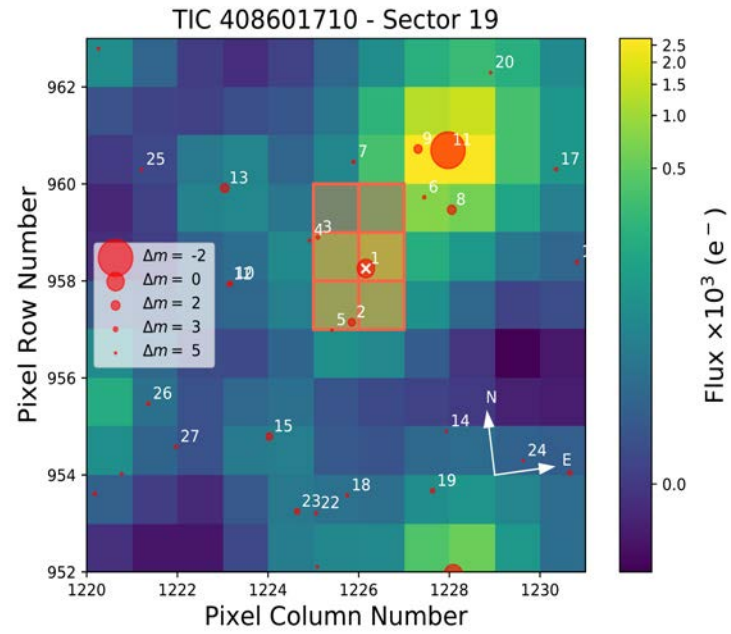
Karmn J03366+034 = [R78b] 233



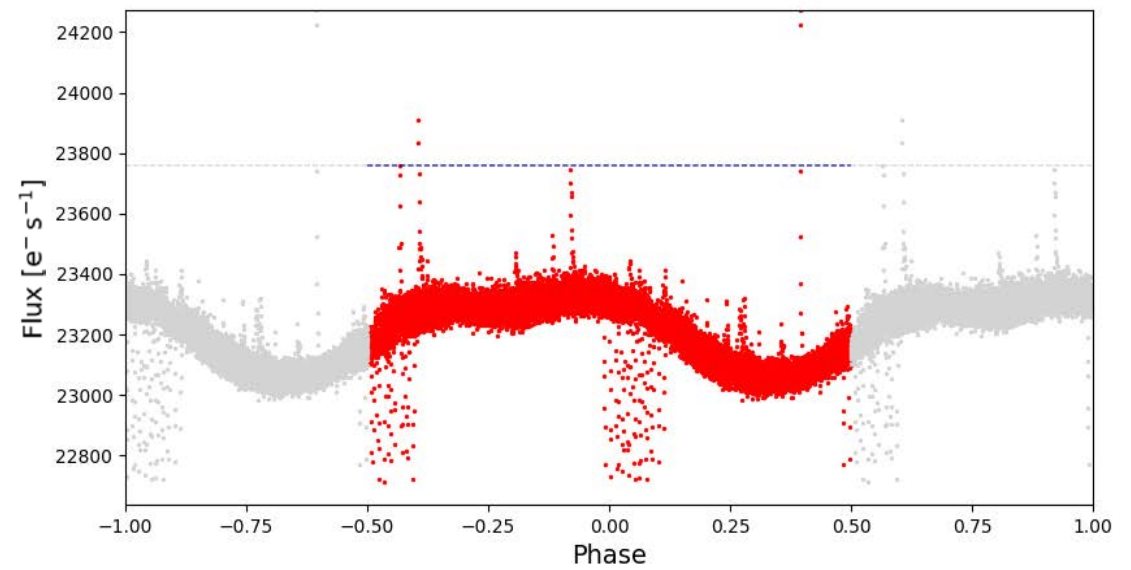
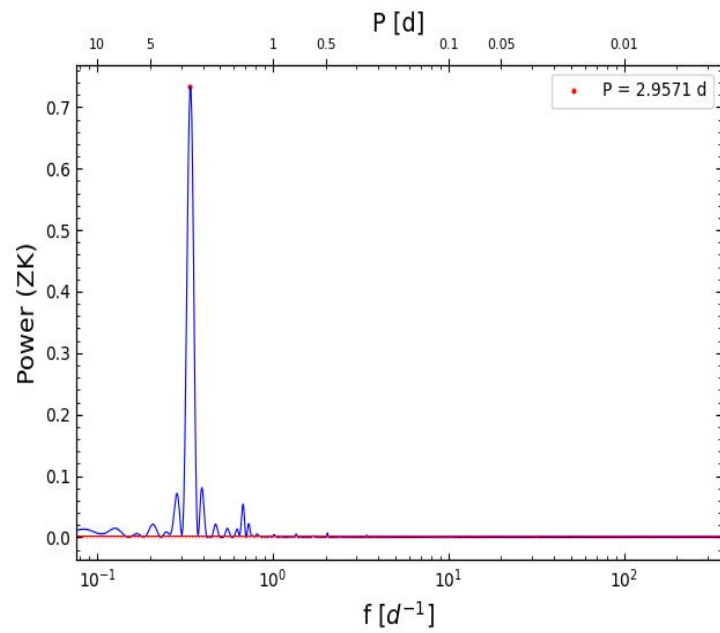
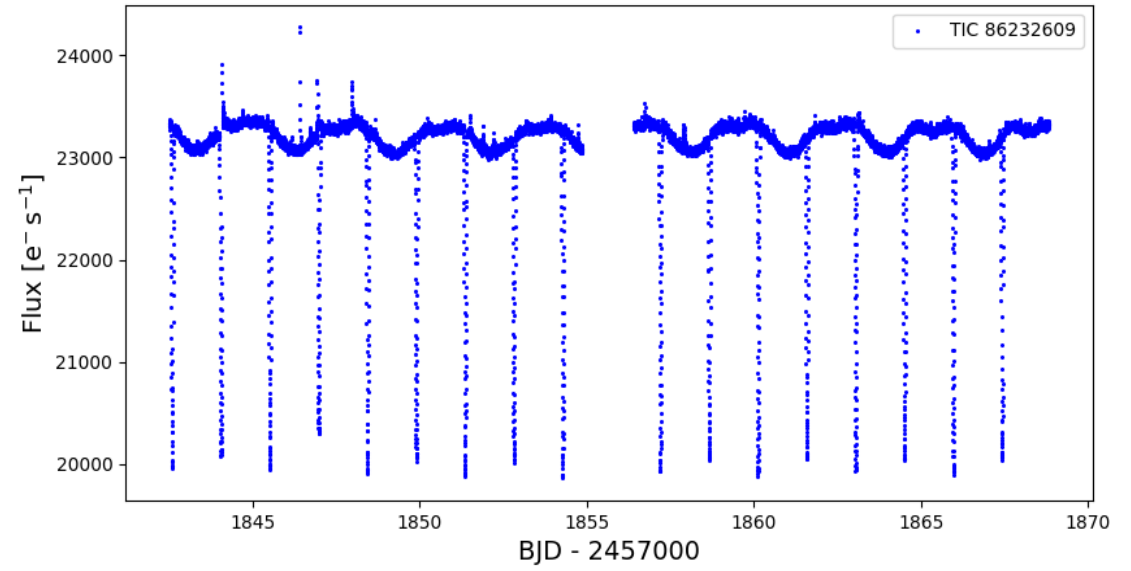
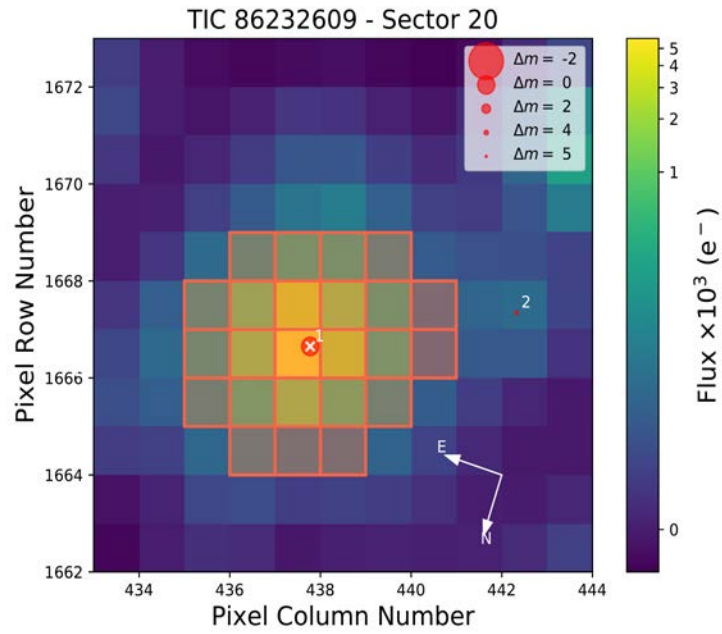
Karmn J04350+086 = StKM 1-495



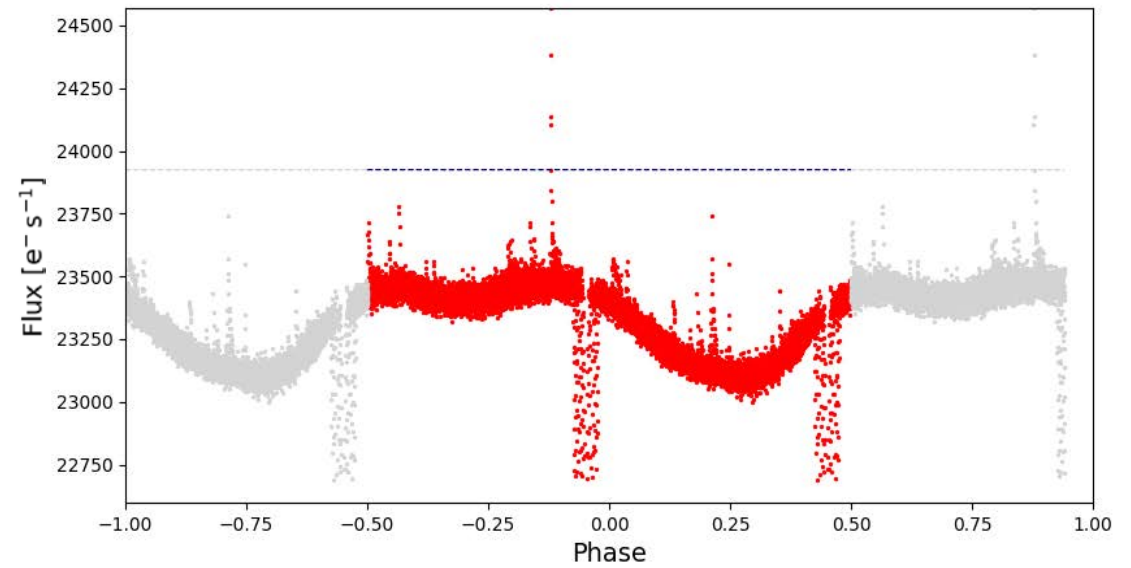
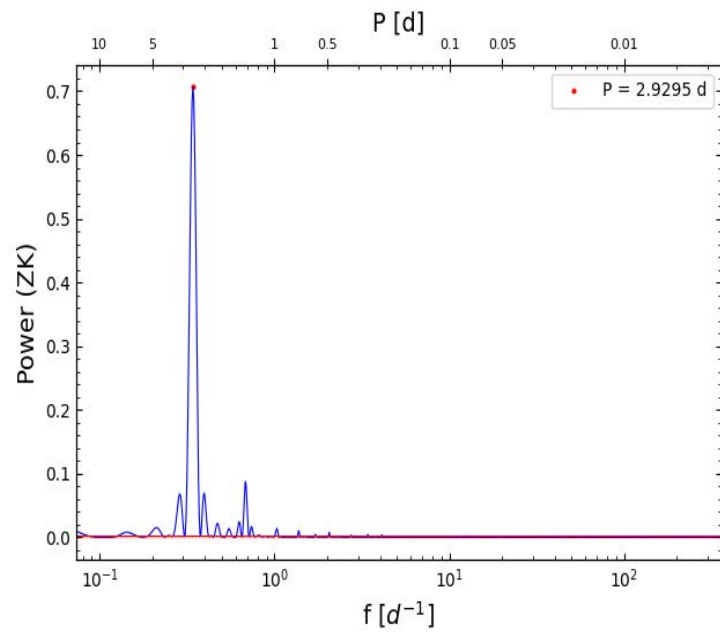
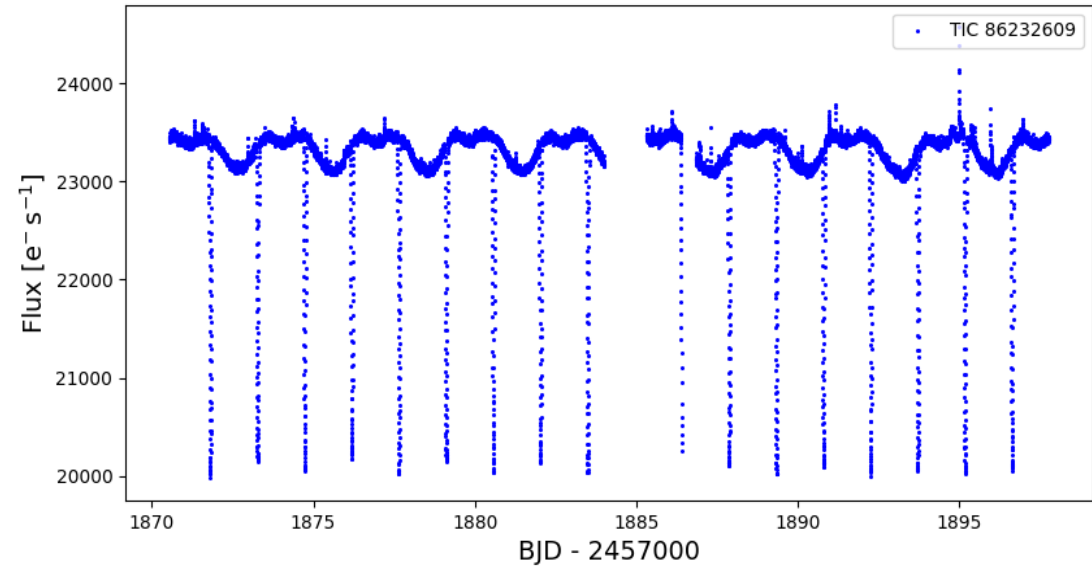
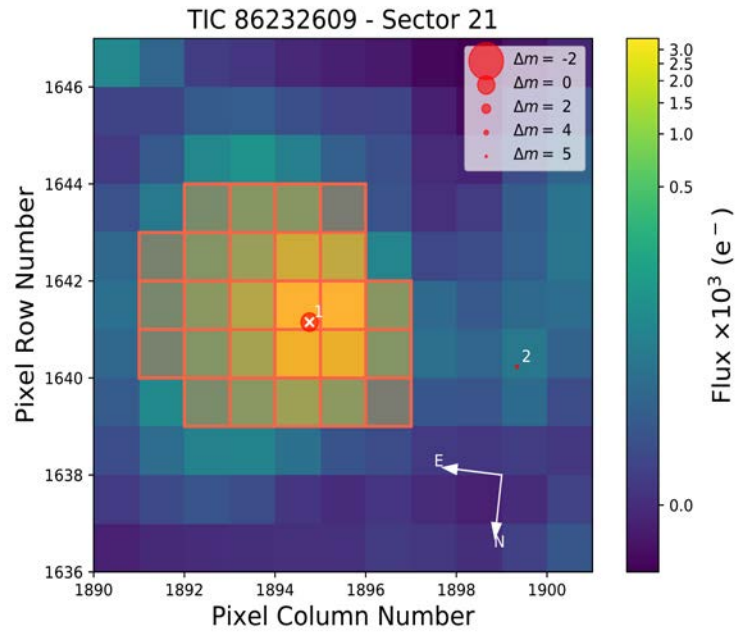
Karmn J04393+335 = RX J0439.4+3332B



Karmn J09193+620 = LP 091-014 AB

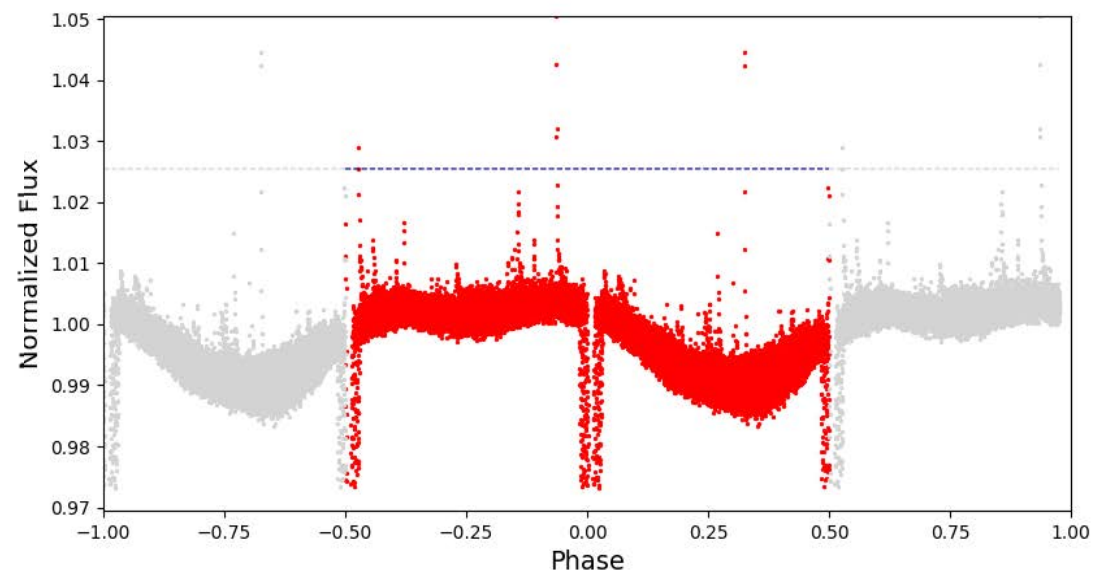
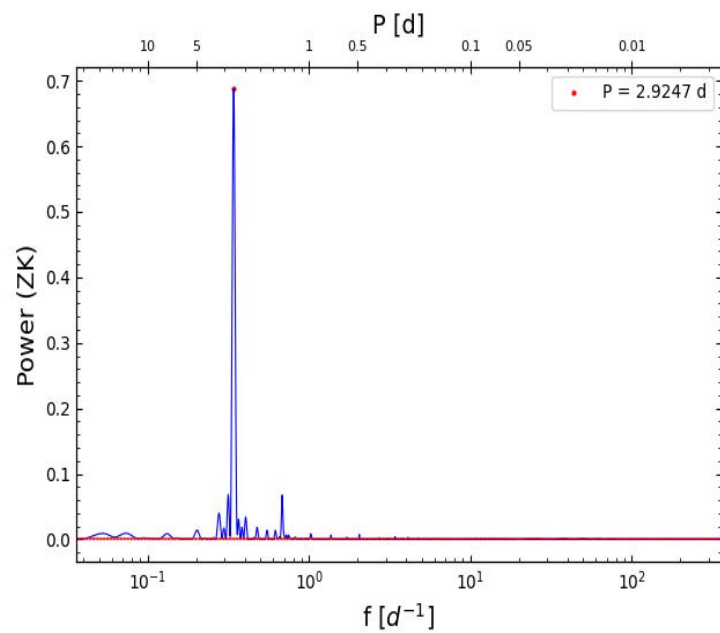
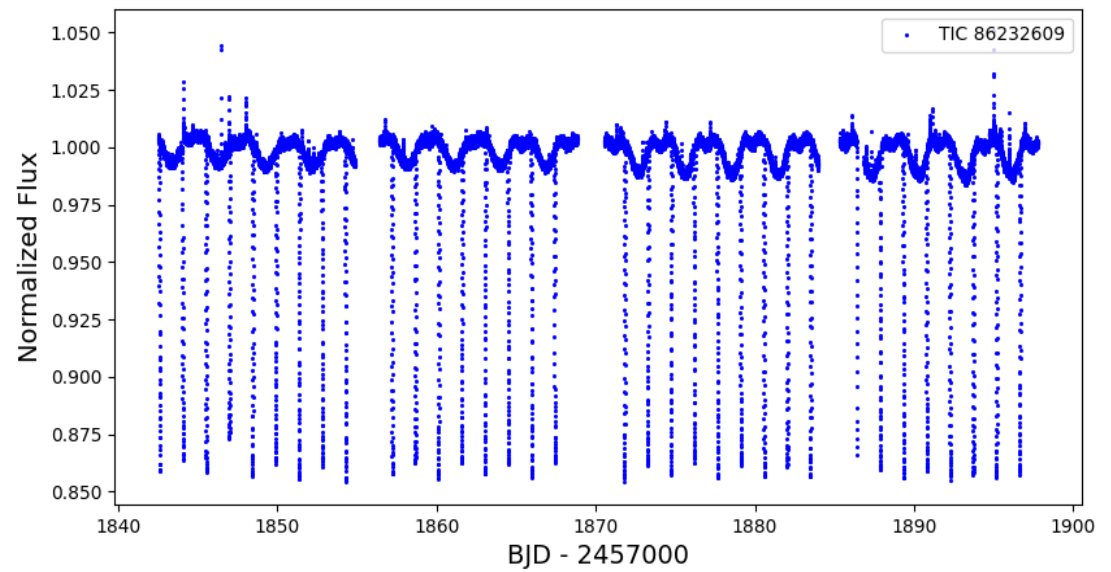


Karmn J09193+620 = LP 091-014 AB

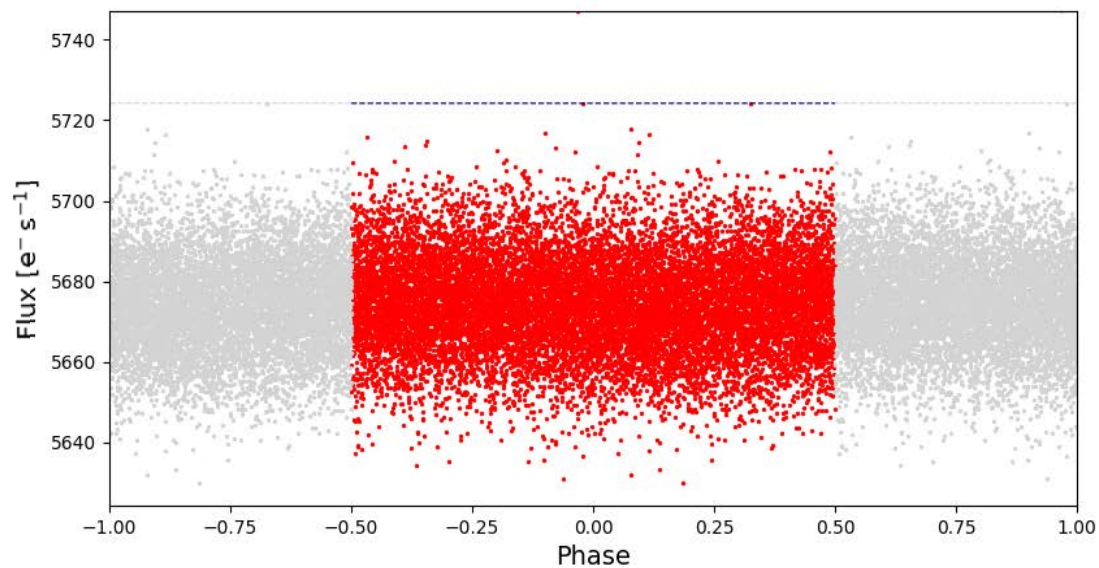
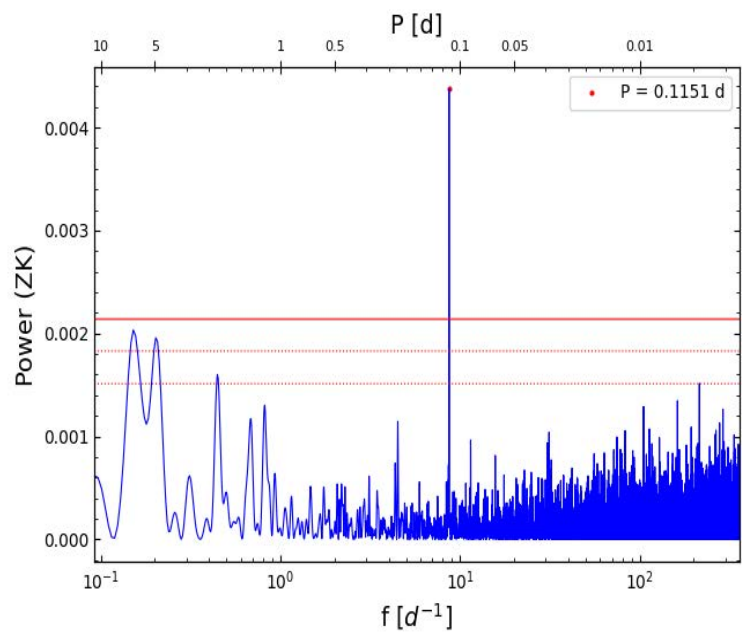
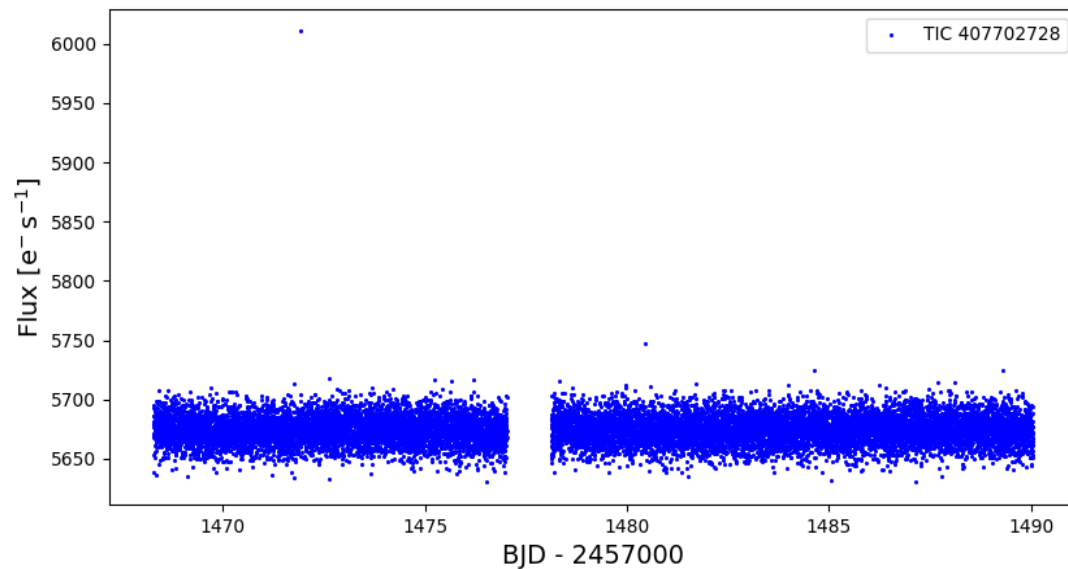
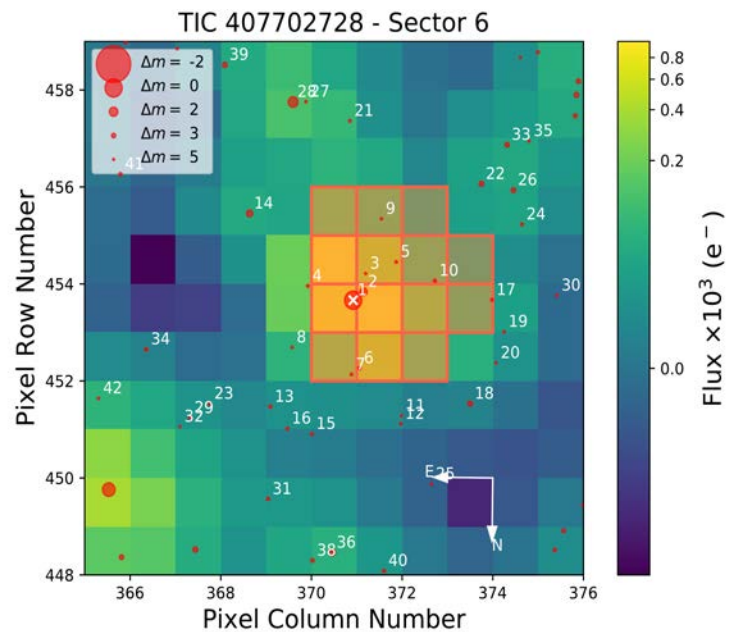


Karmn J09193+620 = LP 091-014 AB

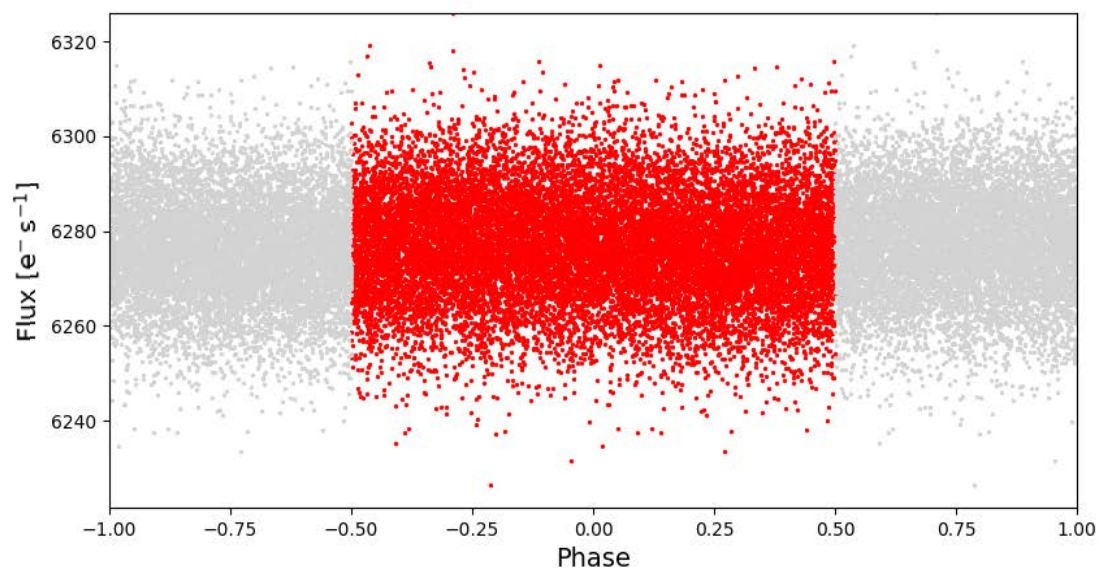
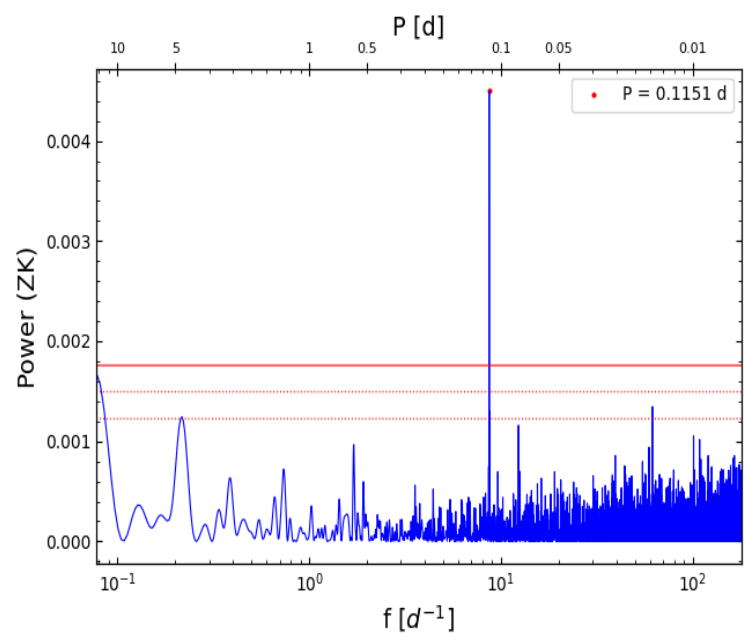
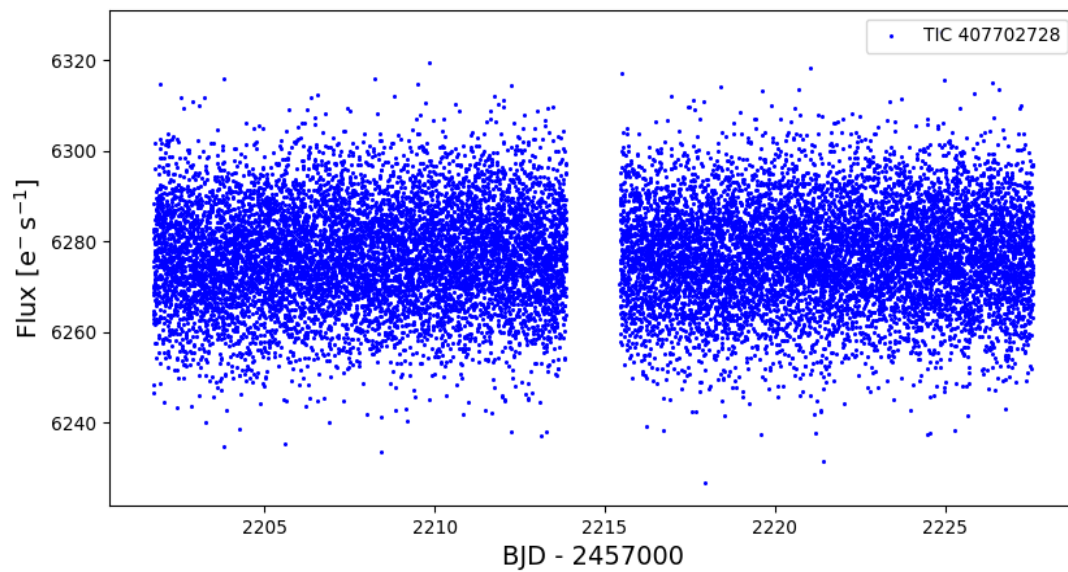
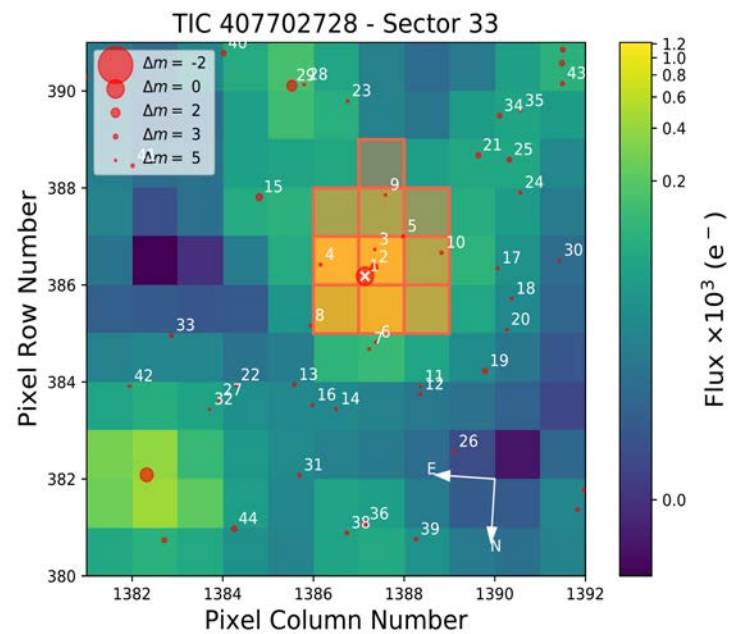
TIC: 86232609 Merged data



Karmn J06509-091 = LP 661-002

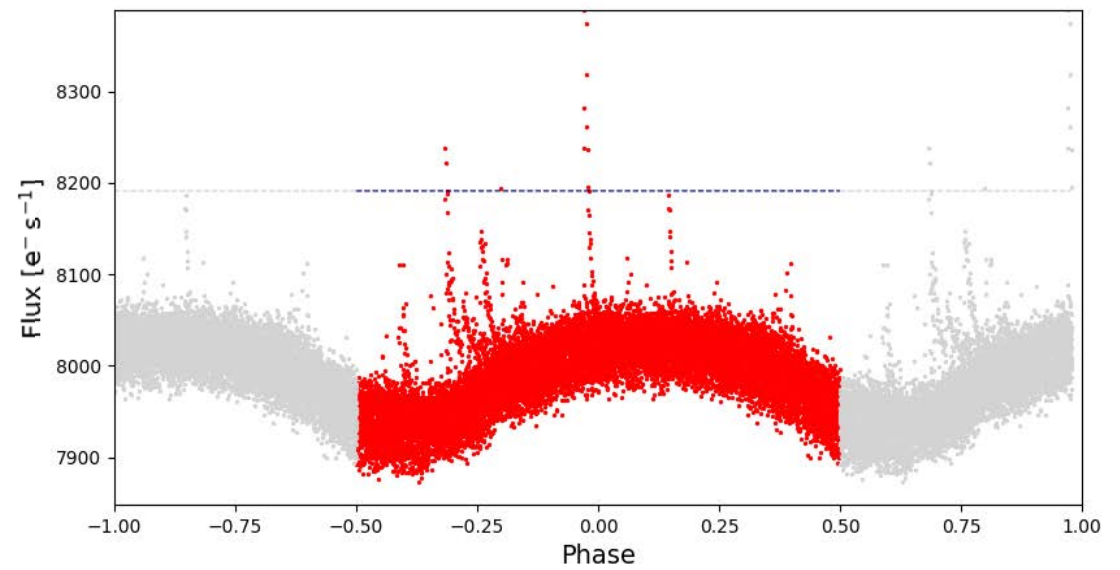
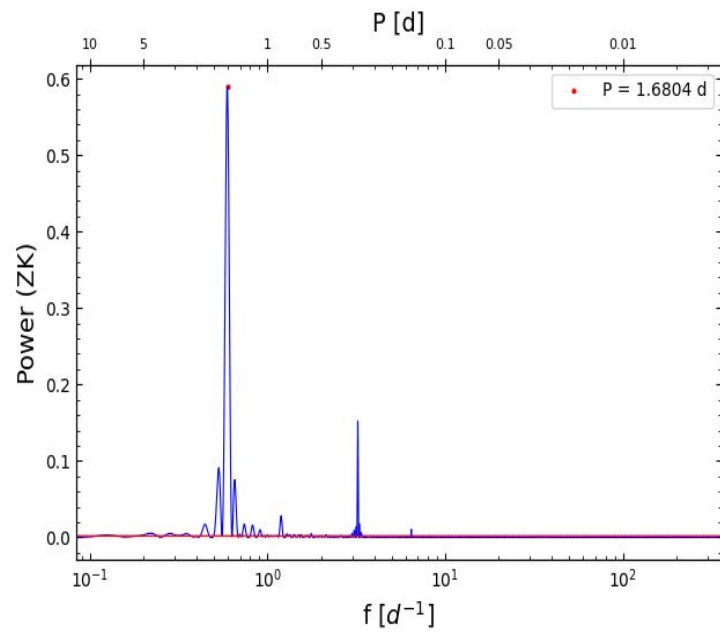
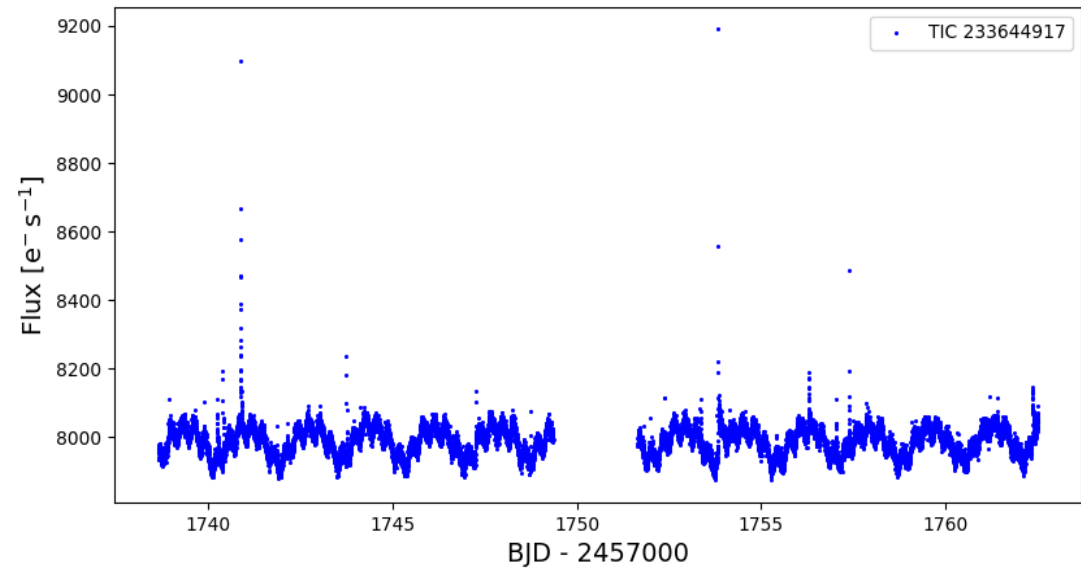


Karmn J06509-091 = LP 661-002



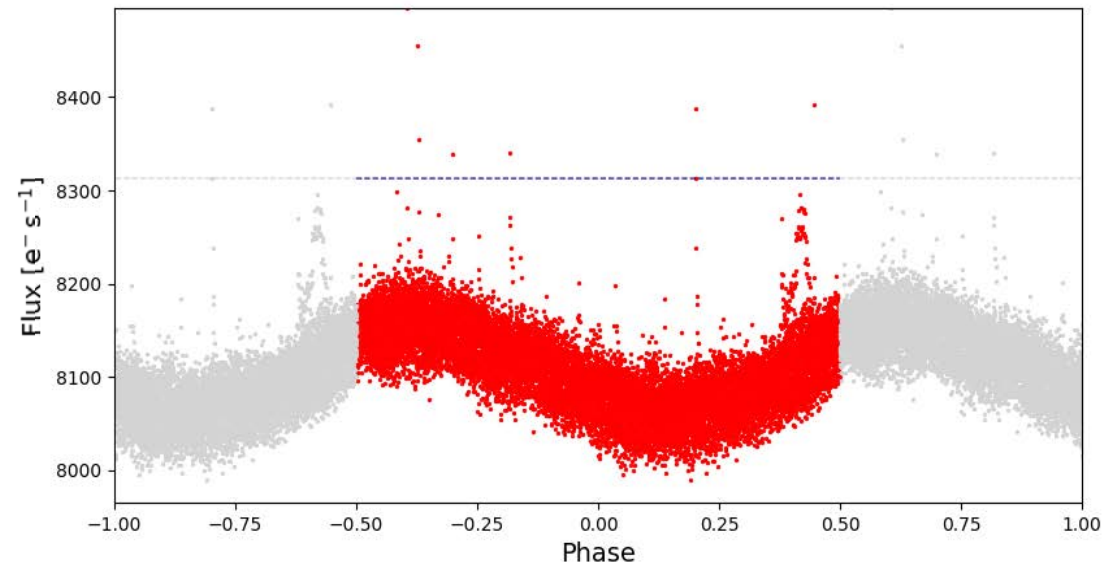
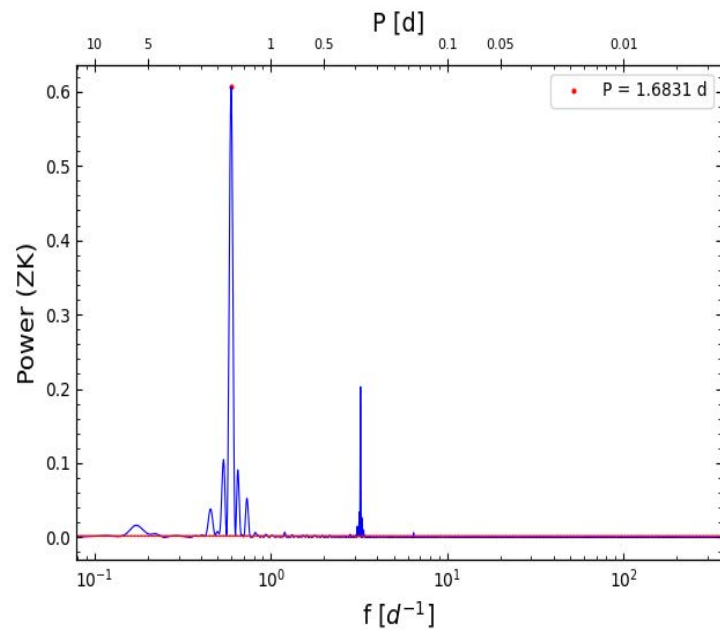
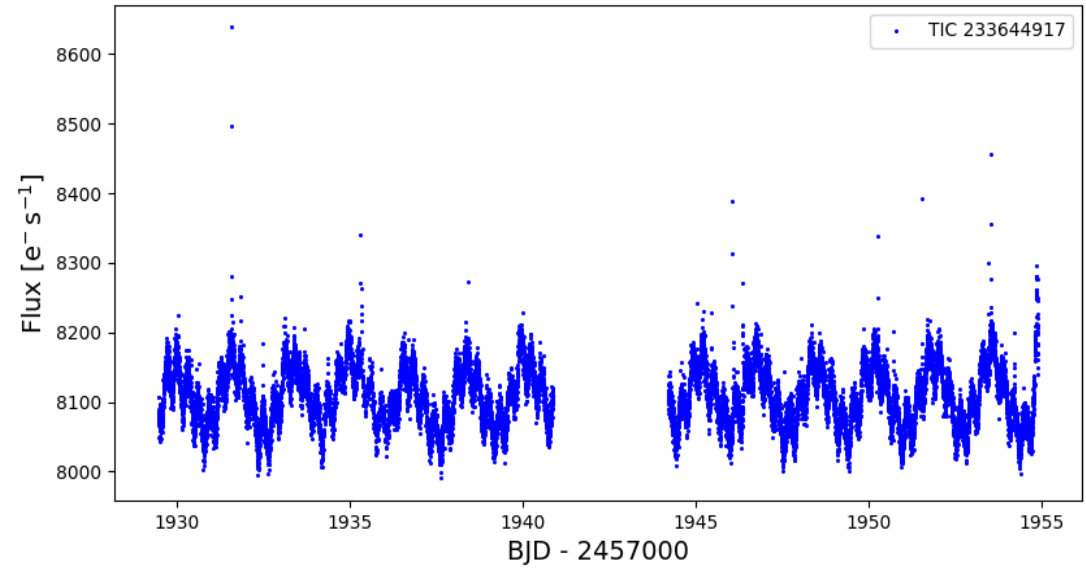
Karmn J15126+457 = G 179-020

TIC: 233644917 Sector 16



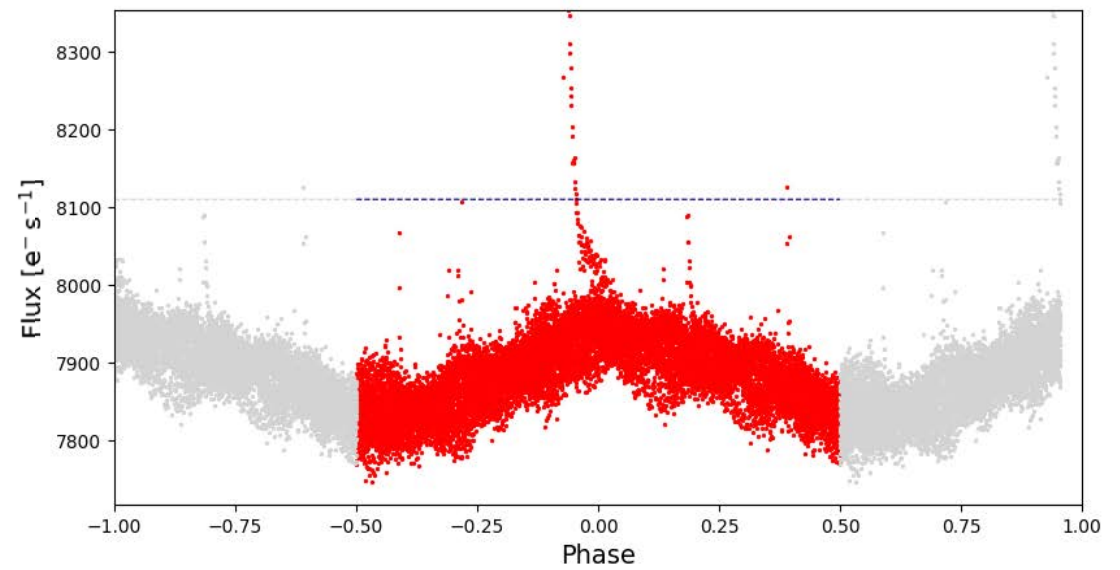
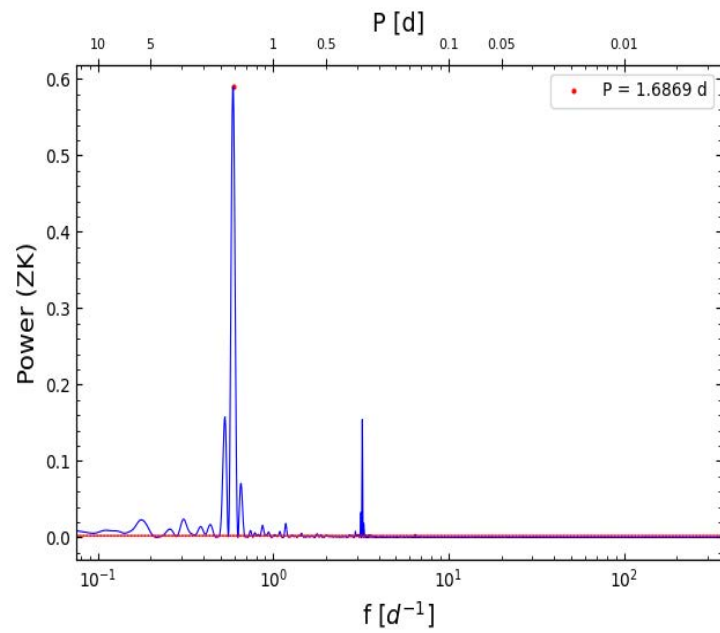
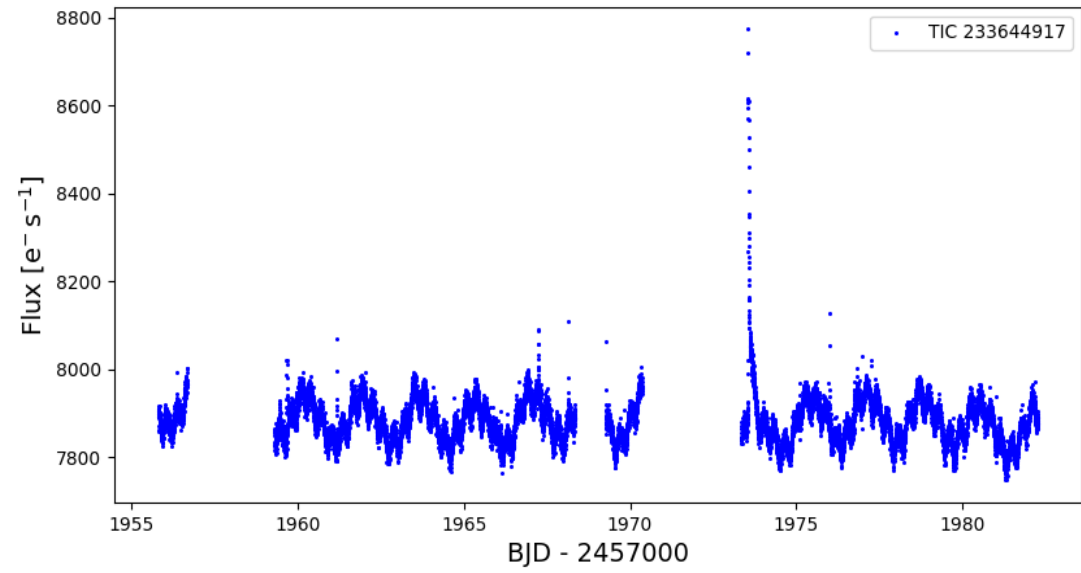
Karmn J15126+457 = G 179-020

TIC: 233644917 Sector 23



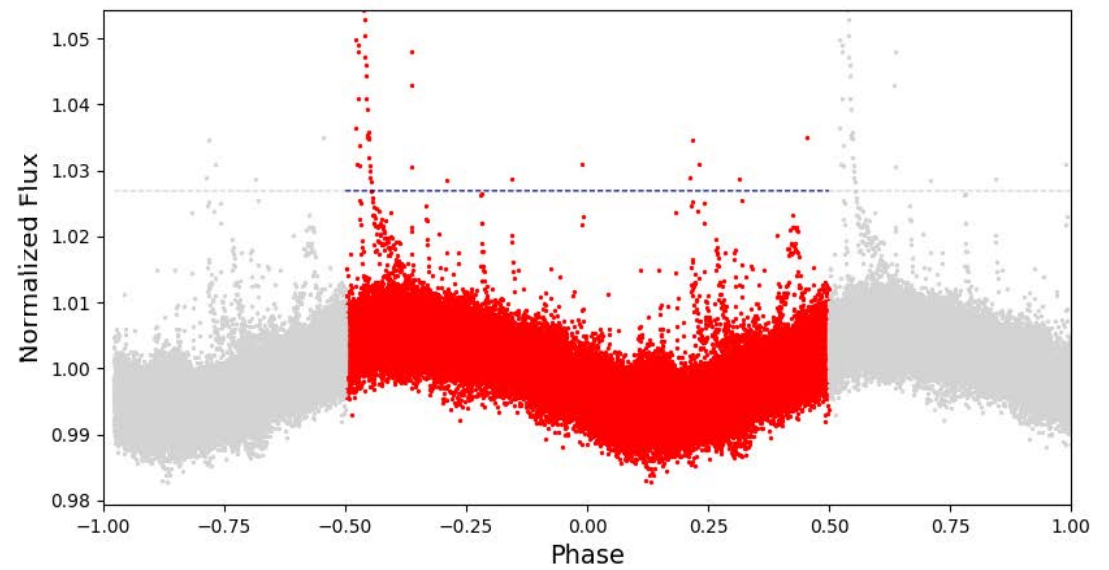
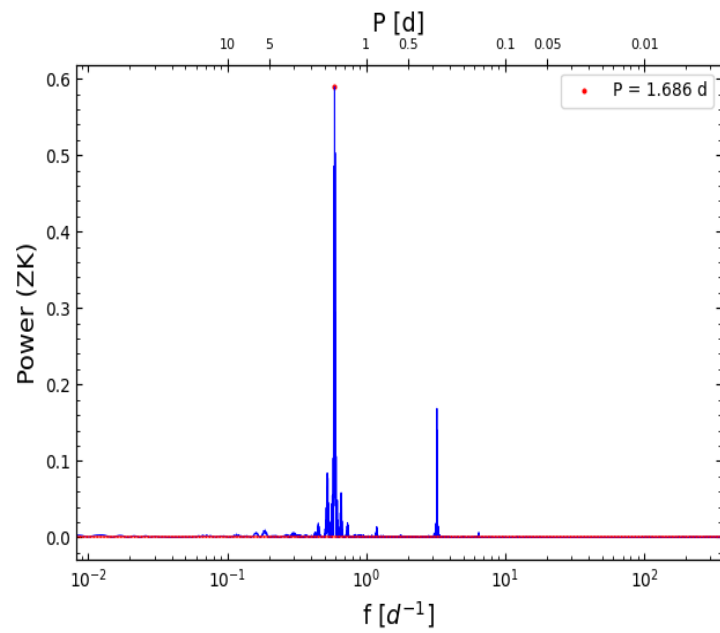
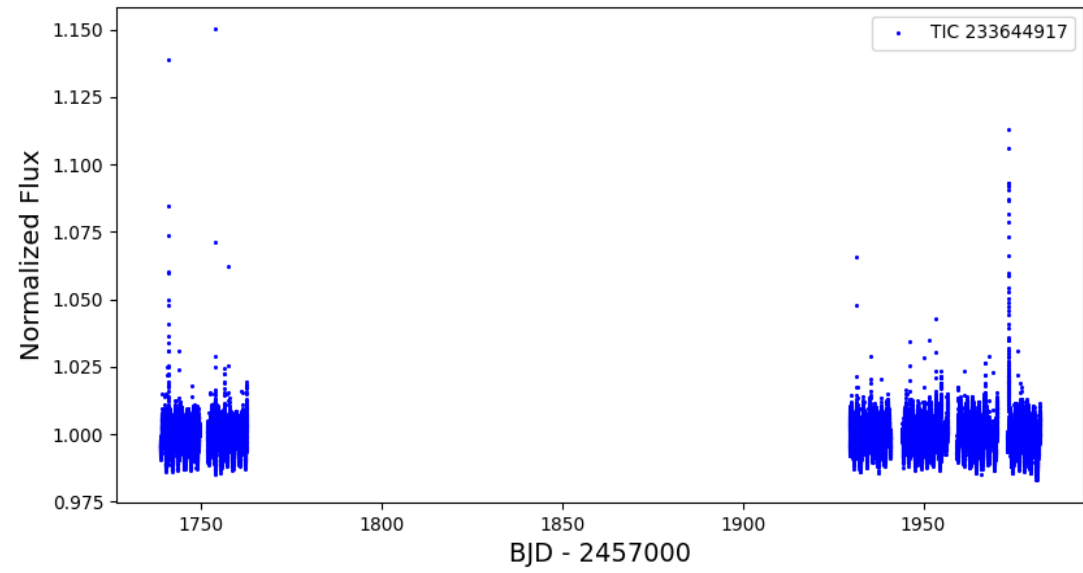
Karmn J15126+457 = G 179-020

TIC: 233644917 Sector 24

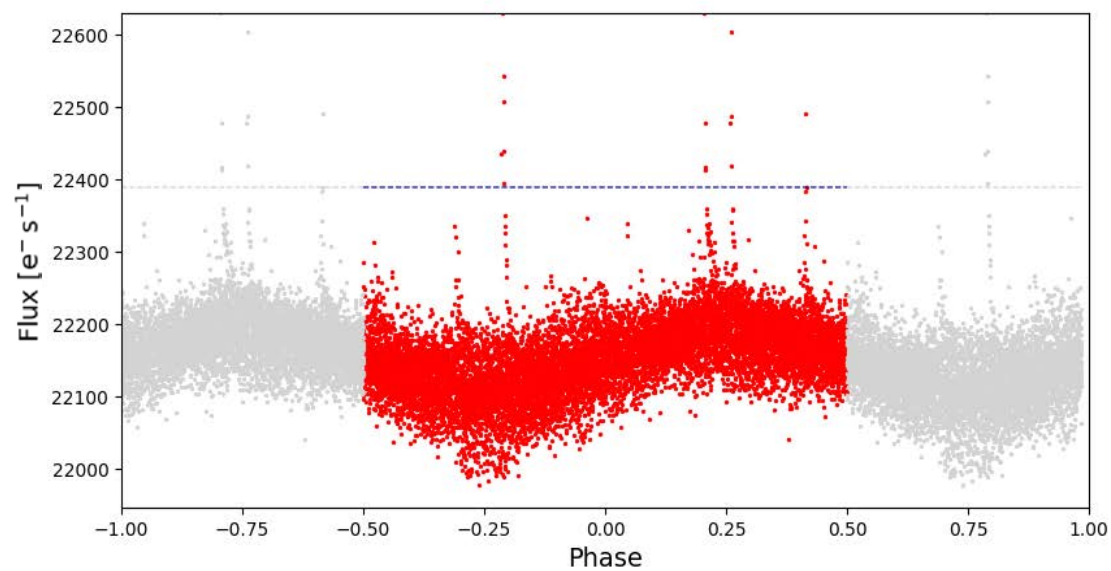
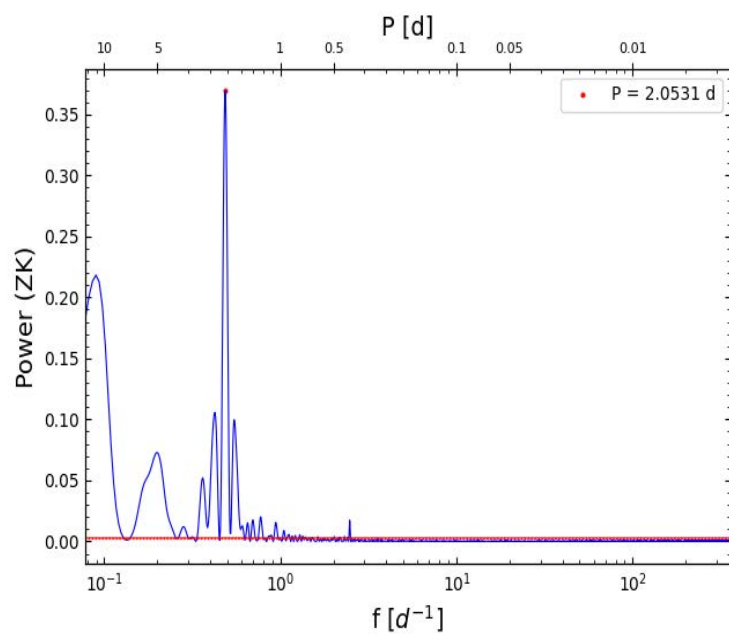
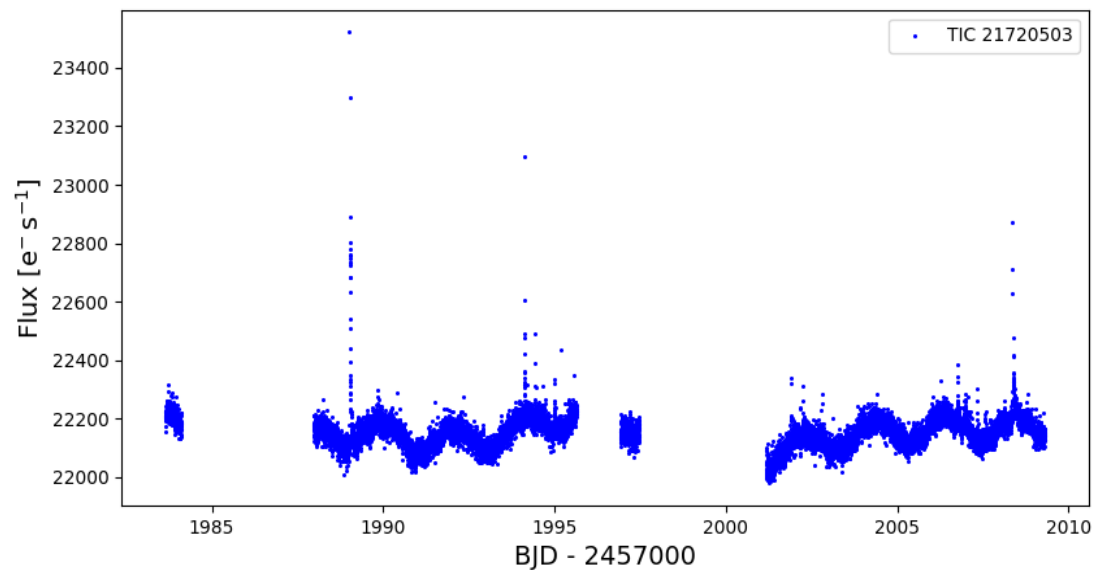
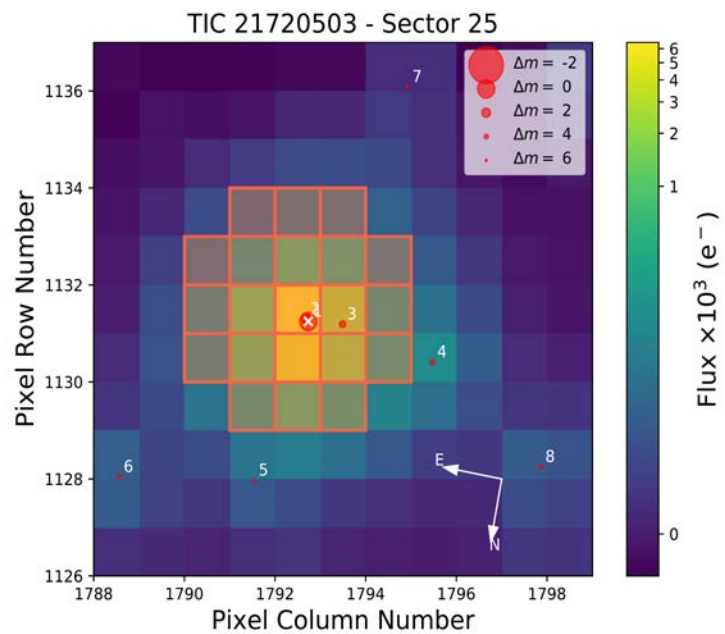


Karmn J15126+457 = G 179-020

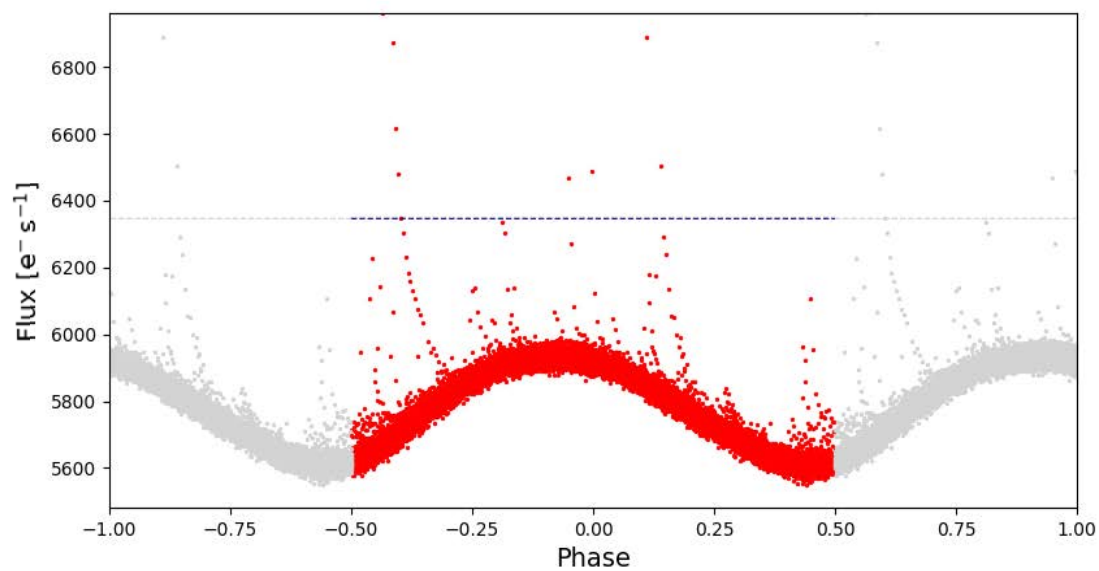
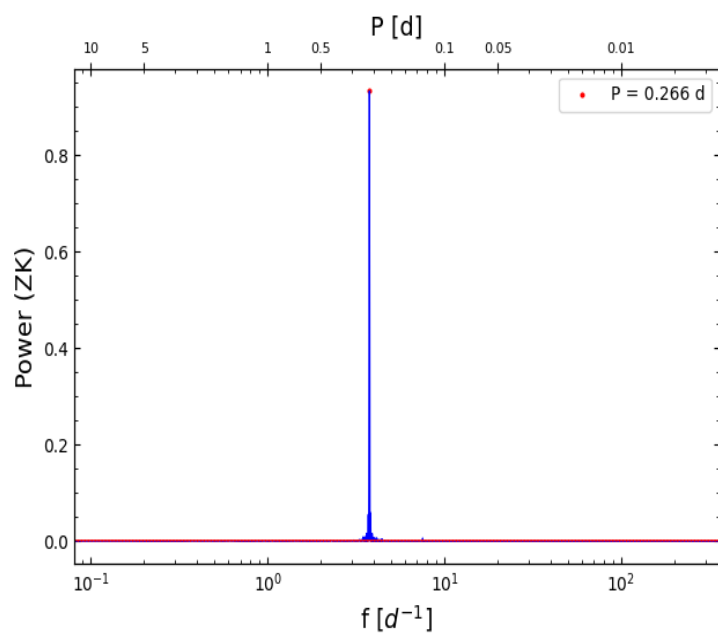
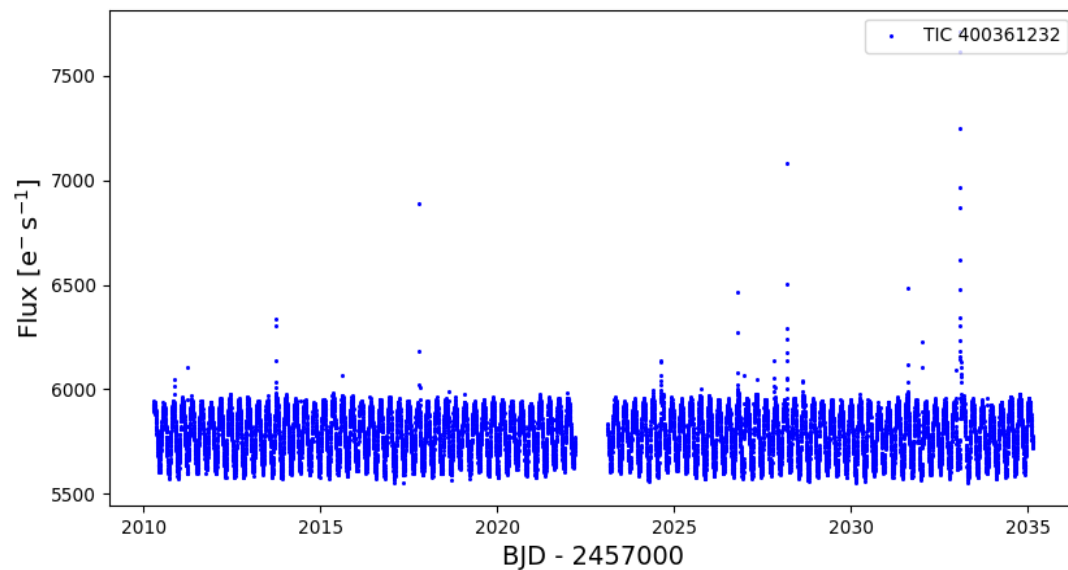
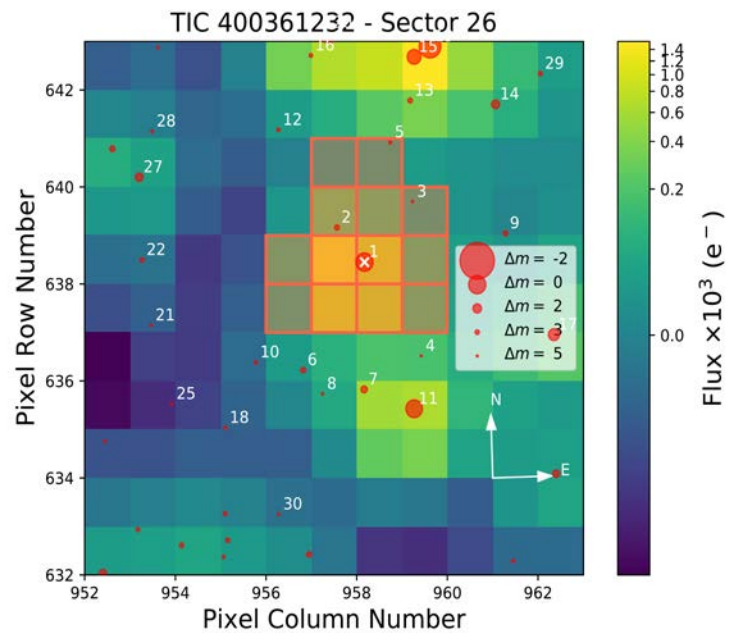
TIC: 233644917 Merged data



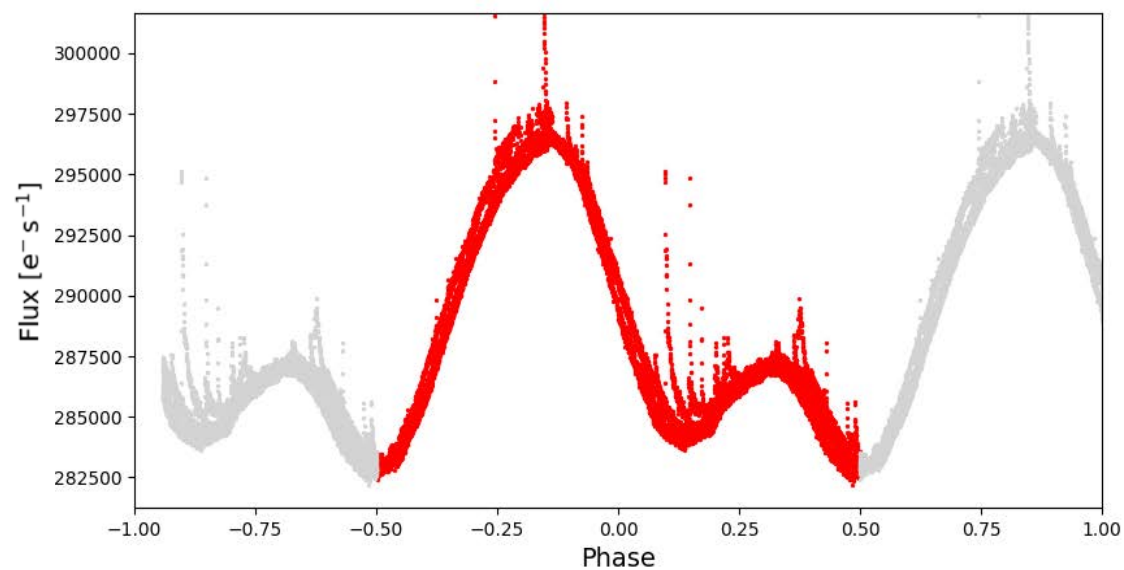
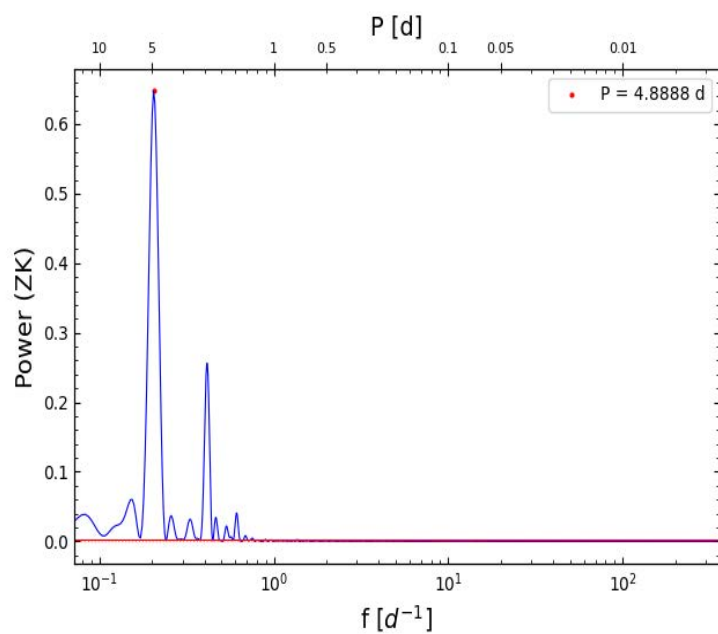
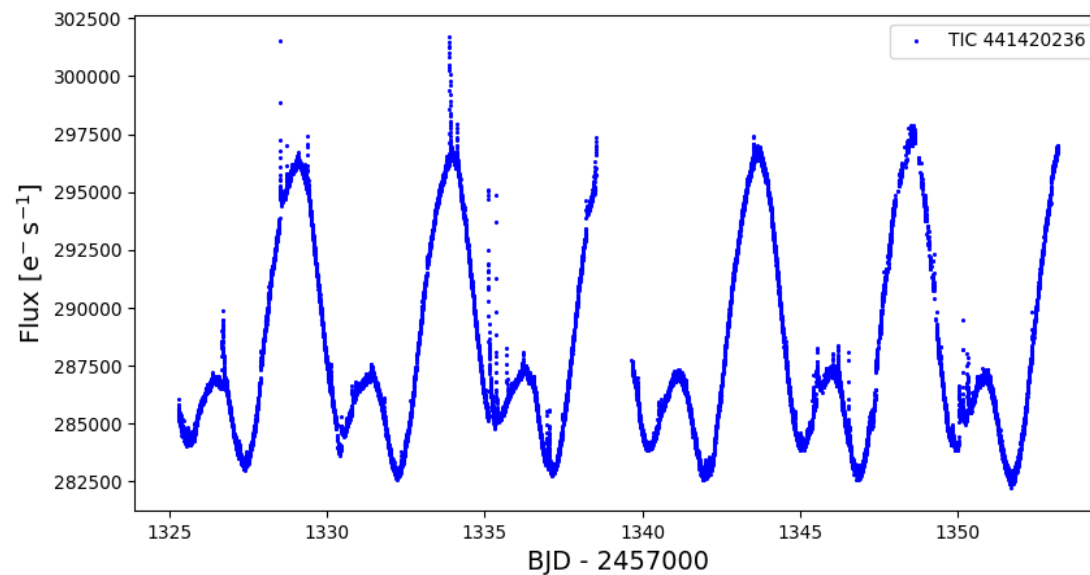
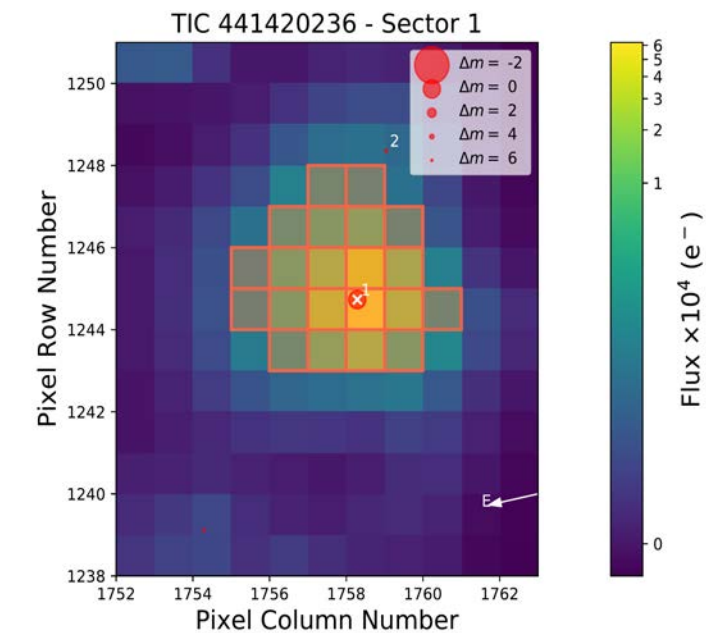
Karmn J17038+321 = LP 331-057



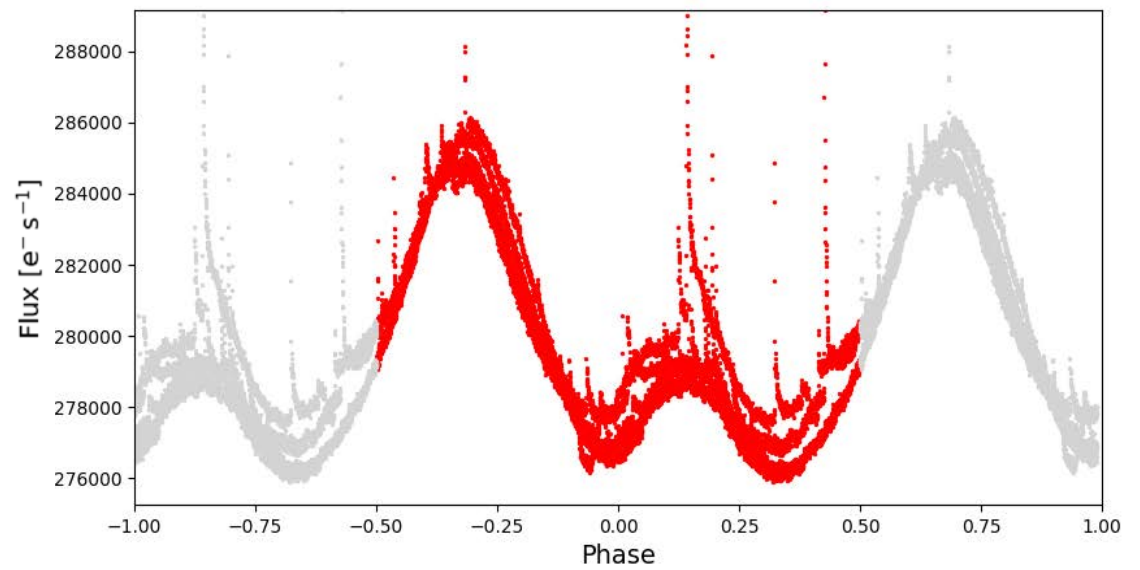
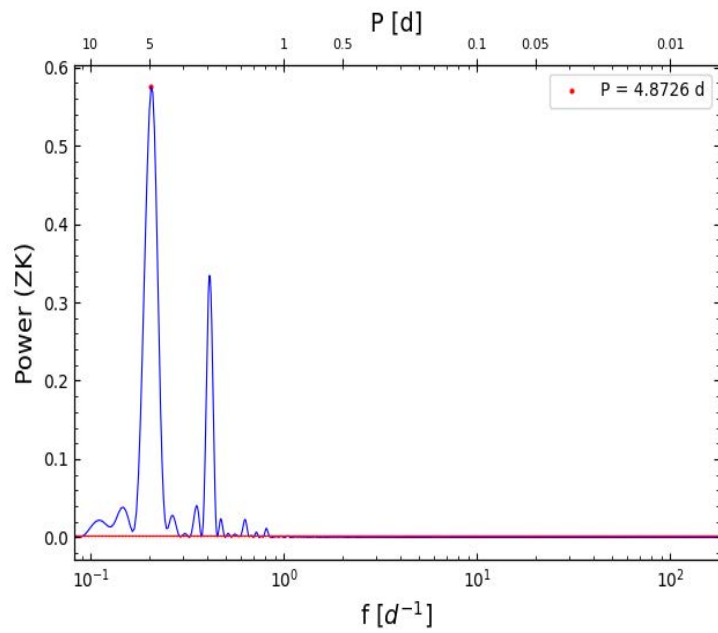
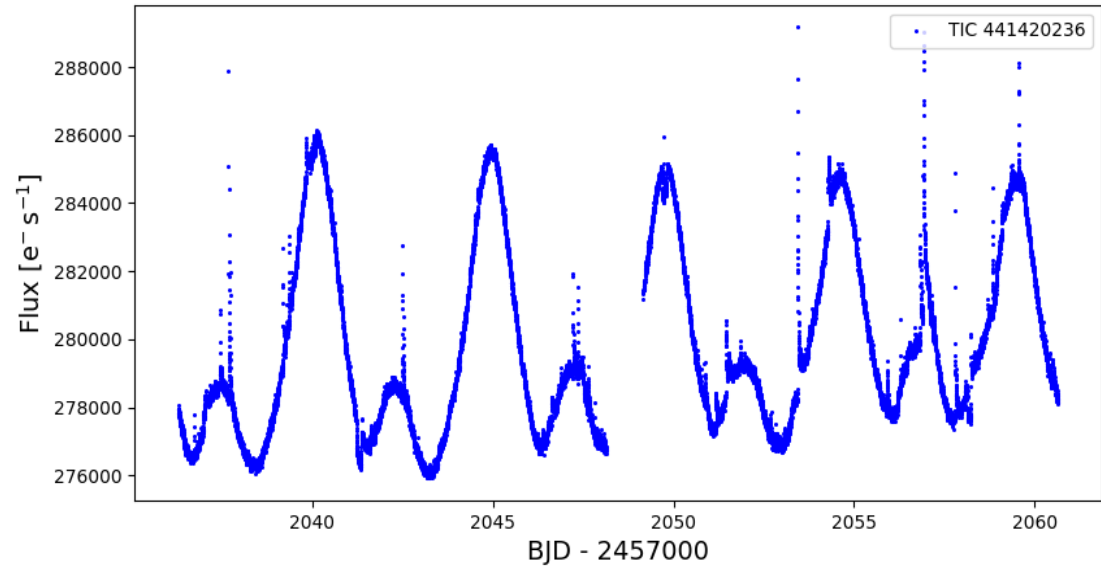
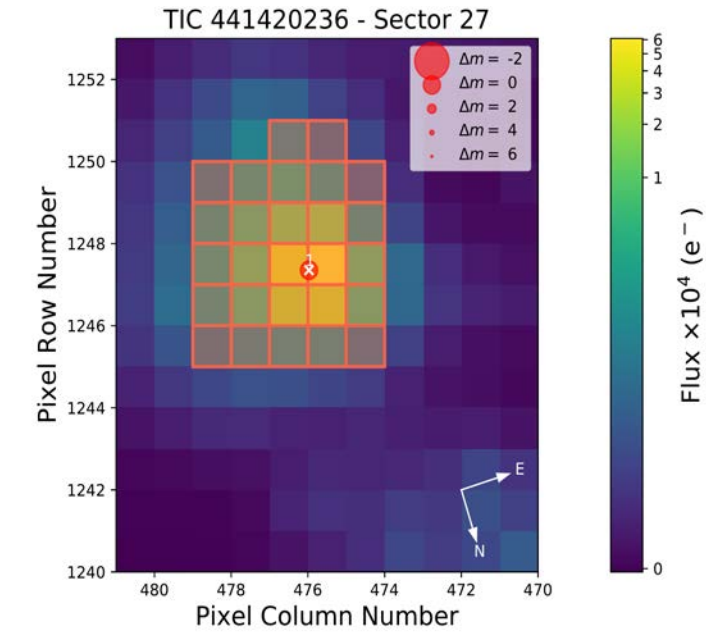
Karmn J17338+169 = 1RXS J173353.5+165515



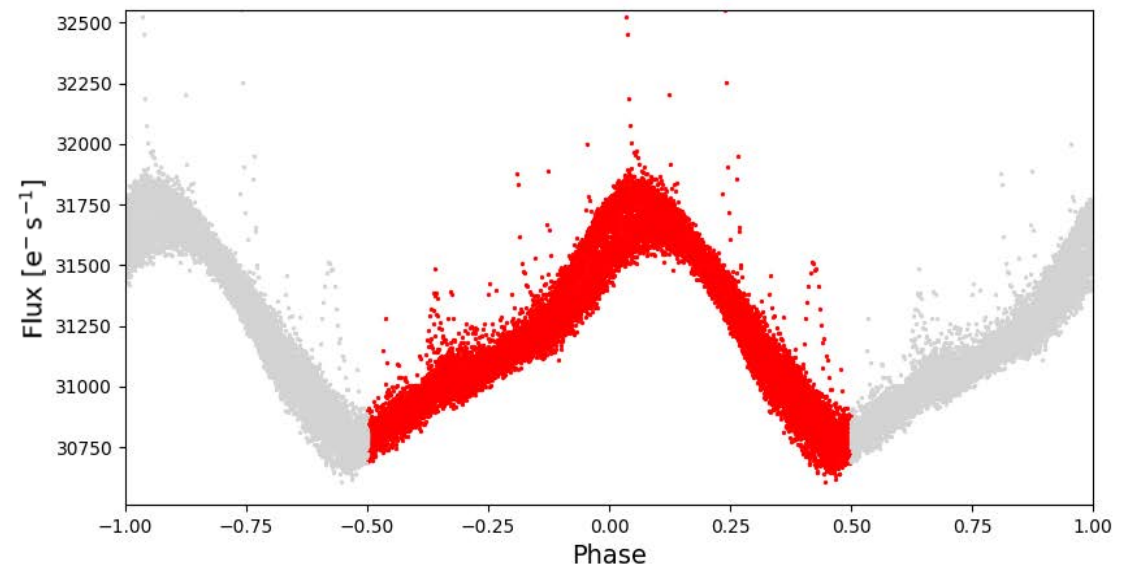
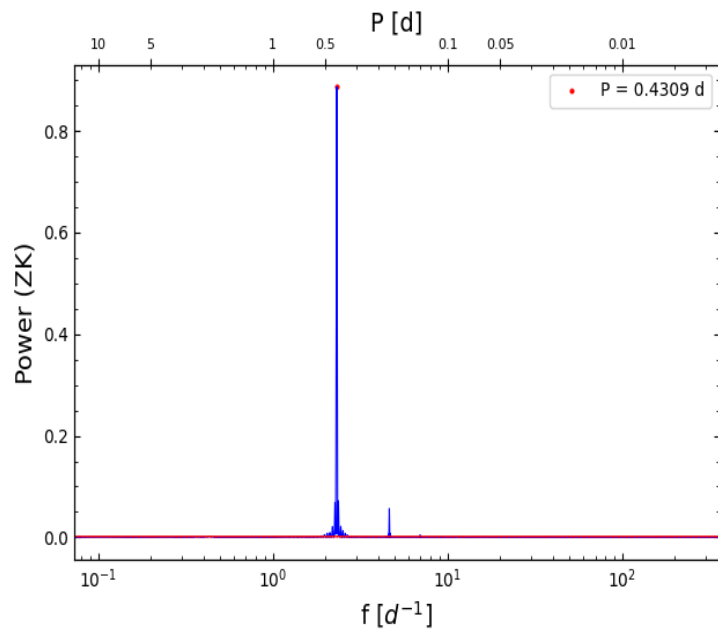
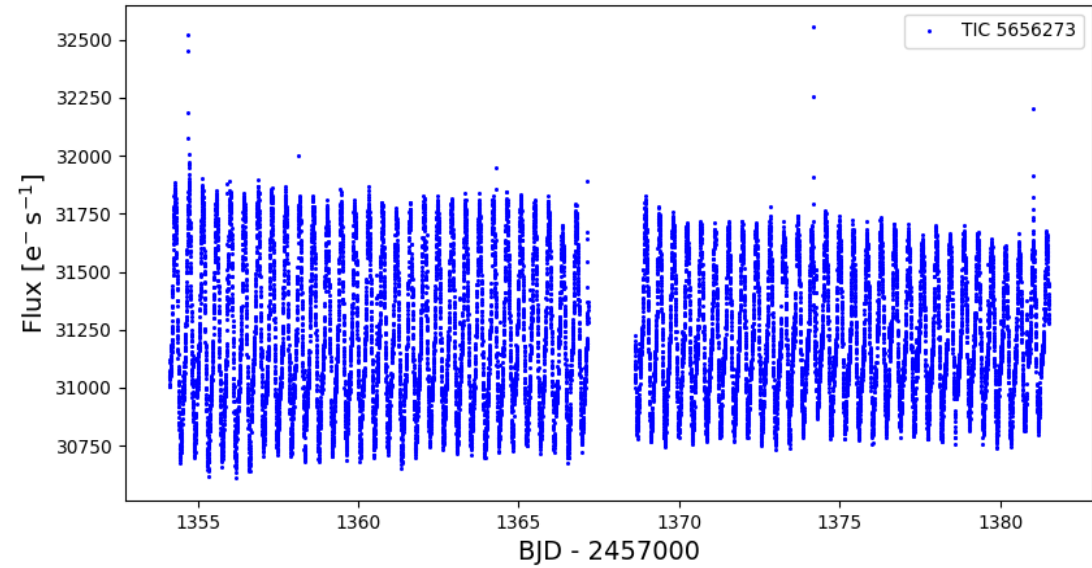
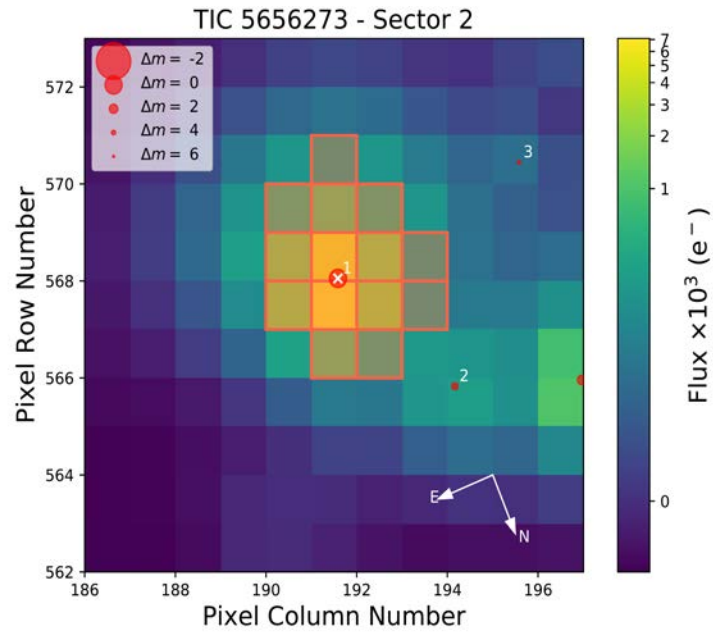
Karmn J20451-313 = AU Mic



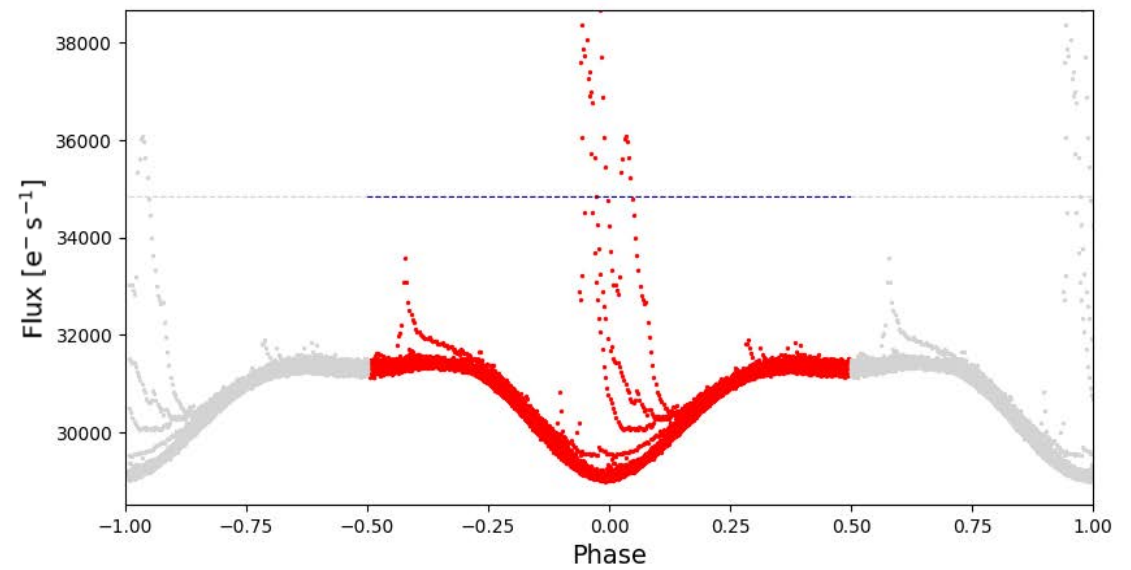
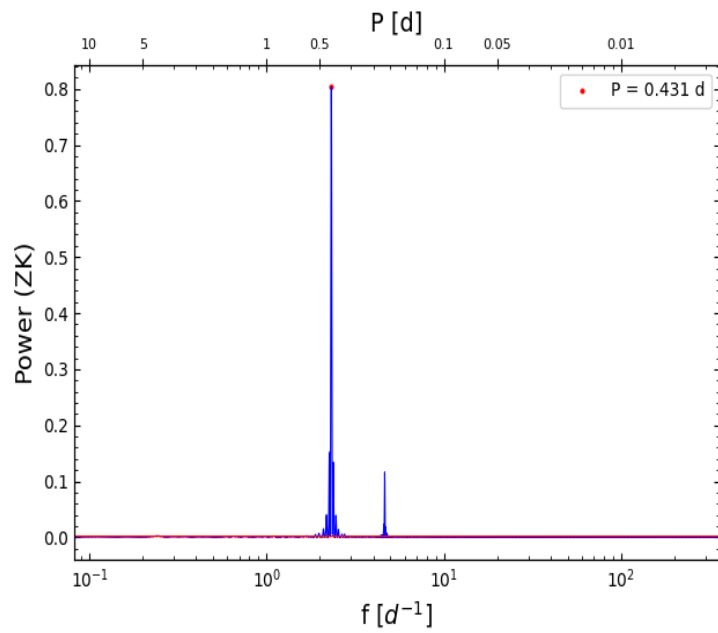
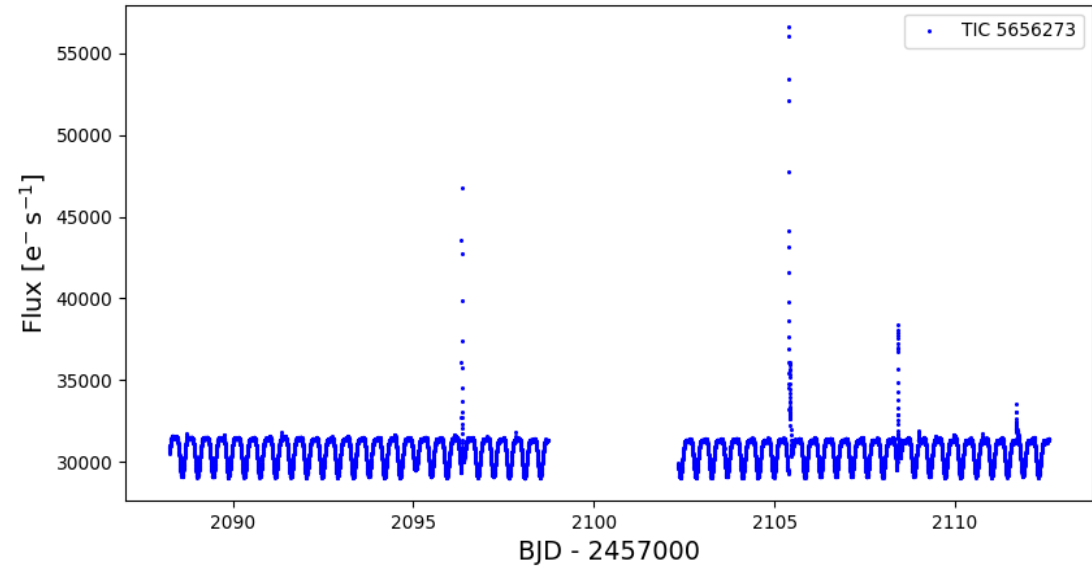
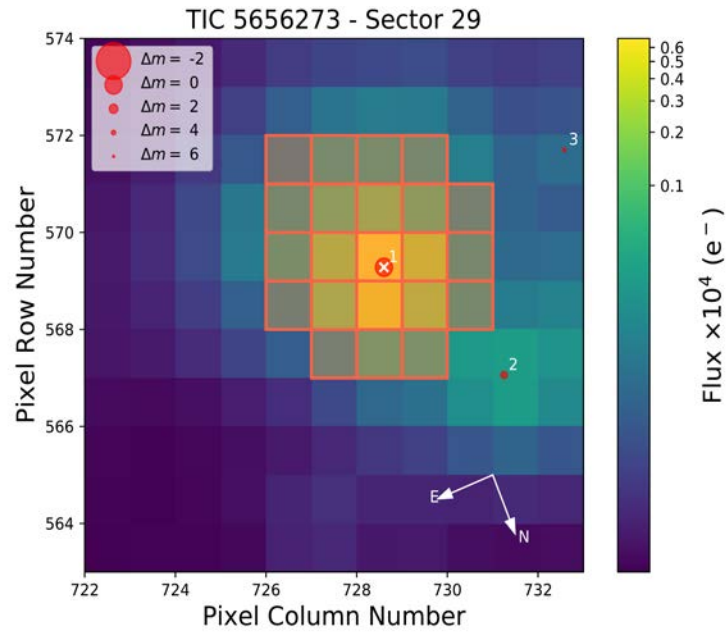
Karmn J20451-313 = AU Mic



Karmn J23083-154 = HK Aqr



Karmn J23083-154 = HK Aqr



C. Solar System objects

Here we show three light curves that show light of a Solar System object passing near or through the aperture mask. The shapes of the peaks are symmetrical enough to be ignored by the flare finding algorithm. However, this can be a potential issue, so every light curve for which we searched for flares was cautiously revised to avoid false positives.

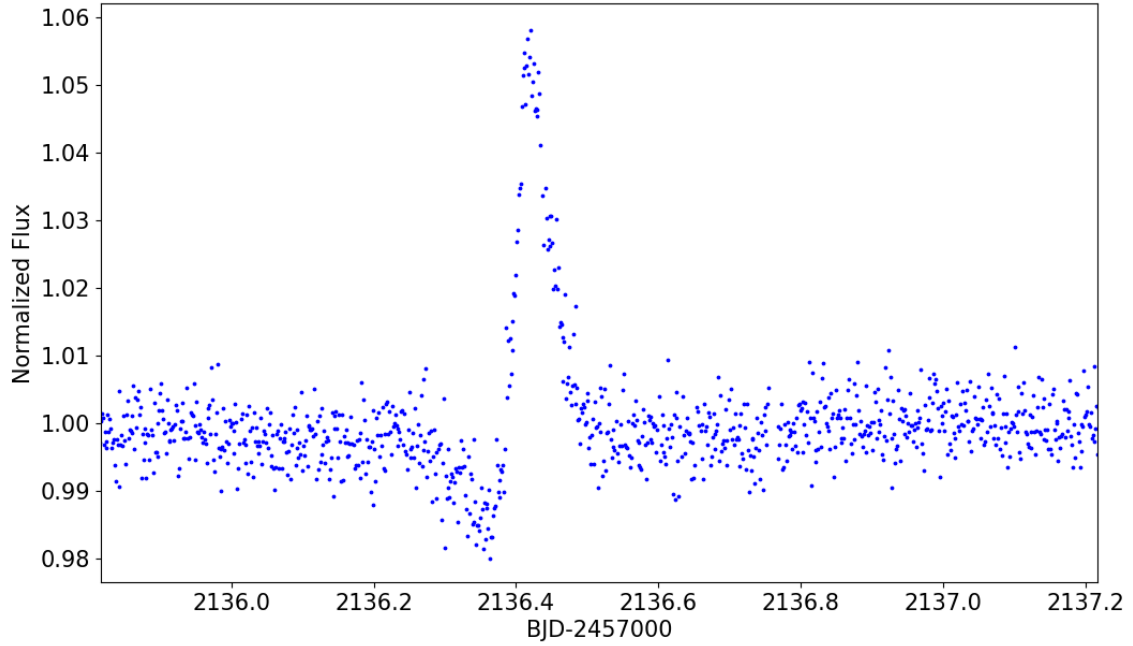


Figure C.1: Light curve of J01009-044 (GJ 1025) in sector 30. We zoom the region around the so the shape of the peak caused by a passing object is visible.

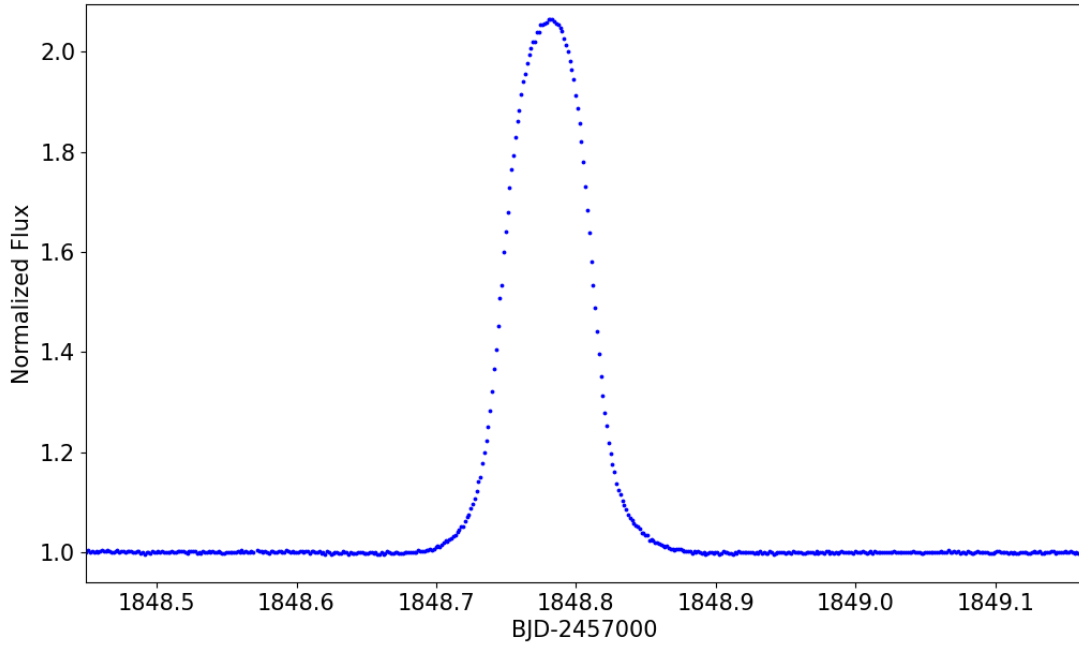


Figure C.2: Same as Fig. C.1 but for J07033+346 (LP 255-011) in sector 20.

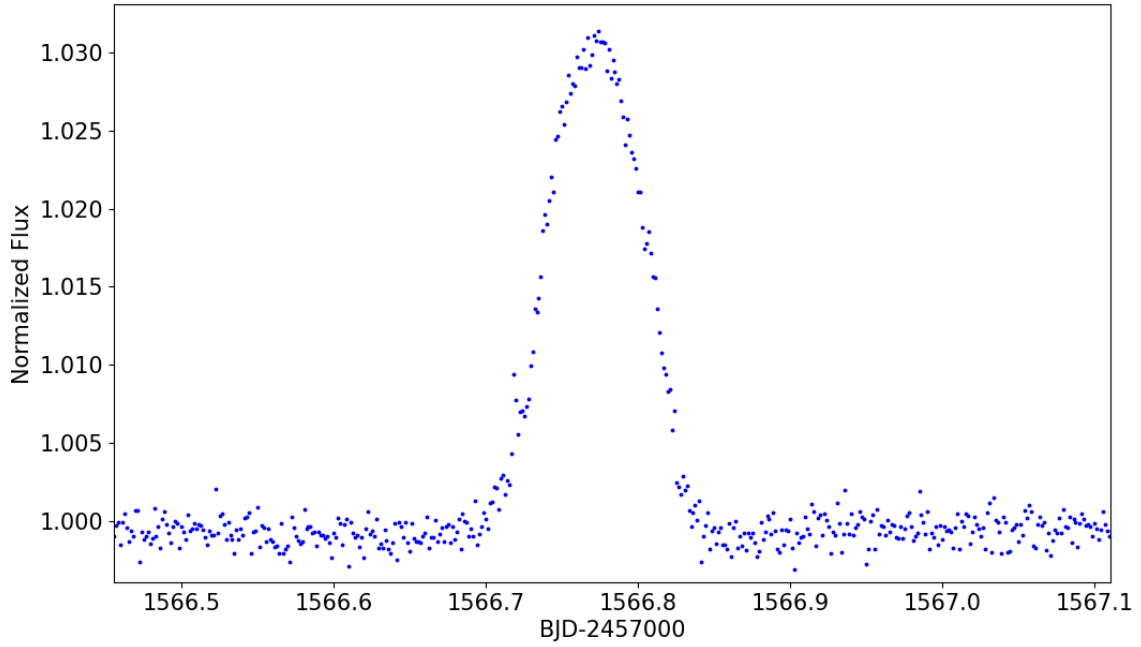


Figure C.3: Same as Fig. C.1 but for J11467-140 (GJ 443) in sector 9.